AN ABSTRACT OF THE THESIS OF

Samuel T. Brannon for the degree of Master of Science in Industrial Engineering presented on June 5, 2013
Title: Development of an Economical High Temperature Microchannel Recuperator for Solid Oxide Fuel Cells

Abstract Approved:

_____

Brian K. Paul

To improve the performance of solid oxide fuel cells, a secondary power cycle can be driven by the recuperation of exhaust gas heat. Microchannel recuperators are attractive for waste heat recuperation due to compact form factors which also minimize the mass of the expensive superalloys required. This paper introduces a new microchannel lamination architecture with the potential to further reduce the cost of high temperature microchannel recuperators. The design consists of a two fluid counterflow microchannel array containing alternating high and low pressure channels made from a high temperature nickel alloy. High pressure microchannels are hermetically sealed by laser welding. Low pressure microchannels contain microchannel flow inserts in the form of micro-scale pyramidal truss networks that prevent the channels from collapsing during operation. A clamshell housing is used to encapsulate the array and provide headering for the low pressure channels. To demonstrate the feasibility of the new microchannel lamination architecture, a sub-scale heat exchanger was designed and fabricated. Functional testing of the device shows a heat exchanger effectiveness of 52% with a pressure drop of 8.7 [kPa] through the low pressure side at a Reynolds number similar to that needed for the full-scale device. Based on our results, a full-scale design is proposed that uses 25% the raw material as the conventional design leading to an estimated cost reduction of over fourfold.

Keywords: Microchannel Recuperator, High Temperature, Nickel Superalloy, Microchannel Flow Insert, Economics

Development of an Economical High Temperature Microchannel Recuperator for Solid Oxide Fuel Cells

By
Samuel T. Brannon

A THESIS

Submitted to

Oregon State University

In partial fulfillment of
the requirements for the
degree of

Master of Science

Presented June 5, 2013
Commencement June 2014

Master of Science thesis of Samuel T. Brannon presented on June 5, 2013.

APPROVED:

Major Professor, representing Industrial Engineering

Head of the School of Mechanical, Industrial, and Manufacturing Engineering

Dean of the Graduate School

I understand that my thesis will become part of the permanent collection of Oregon State University libraries. My signature below authorizes release of my thesis to any reader upon request.

Samuel T. Brannon, Author

ACKNOWLEDGEMENTS

First and foremost I'd like to acknowledge my Advisor, Dr. Brian Paul, for the trust and support he gave me throughout this exhausting process, as well as his patience. Enabling me to learn far more than a manufacturing degree often calls for; he provided insight and access to resources to help me get through it all. More importantly, he provided an environment in which I felt free to explore any option available, and to break preconceived notions of what a microchannel device needs to look like. He allowed me to cater my education to be exactly what I wanted it to be; filled with learning of every kind. Secondly I bring up my family. They spent my entire life promoting my interests in science and engineering and never dissuaded me from achieving my goals. My siblings may have teased me growing up, but when I needed advice and support as to what I needed to do next in life, they reminded me of who I am and who I have the potential to be. My father always said there are only two guarantees in life; death and taxes. My mom always reminded me that everything else is up in the air and under one's own control. Their loose guidance in my youth allowed me to make my own path in life and for that I thank them from the bottom of my heart. I'd also like to acknowledge Ryan Dubina and Kadee Mardula, two people who since I've known them helped me kept my eye on the ball. The distracting adventures they undertake with me, the long climbing sessions they endure, and the hugs they provide keep me trucking on a daily basis. The love these two people give to those they care about is unquestioning and unparalleled in volume and I am blessed to be on the receiving end of it. I'd like to acknowledge Don Higgins and Jair Lizarazo-Adarme of PNNL who helped me with my TDV testing, and Hailei Wang who helped me learn the proper way to test and evaluate the performance of my device. My colleagues at the MBI provide an environment in which knowledge has no bounds and is free-flowing across disciplines. I could not ask for a better place to spend the next few years of my life.

TABLE OF CONTENTS

TABLE OF CONTENTS (Continued)

TABLE OF CONTENTS (Continued)

LIST OF FIGURES

LIST OF FIGURES (Continued)

LIST OF TABLES

Development of an Economical High Temperature Microchannel Recuperator for Solid Oxide Fuel Cells

1 Introduction

In response to the demand for higher efficiency power generation systems, advances in materials and material processing have enabled the use of solid ceramics as the electrodes and electrolyte within a hydrogen fuel cell. These solid oxide fuel cells (SOFCs) have increased efficiency, decreased carbon dioxide emissions, and an increased useful life over traditional designs containing metal electrodes and liquid electrolytes[1]. Although the use of ceramics improves the functionality of fuel cell systems, ion and electron transport is only enabled at increased temperatures, typically between 600 and 1000[°C]. As a result, metallic components can be required which have stringent requirements for creep life and corrosion rates. Typically these Ni and Fe-based superalloys are expensive which increases the cost of the SOFC system.

One method for further increasing system efficiency of SOFCs is to incorporate the SOFC into a combined cycle with an indirectly-fired gas turbine.[2] In this cycle, a waste heat recuperator replaces the combustor in a direct-fired gas turbine. The waste heat (900[°C]) from the SOFC exhaust pre-heats the incoming process air which is then run through a turbine before entering the fuel cell. Because the recuperator is typically made out of an expensive superalloy, opportunities exist to reduce the cost of the recuperator and the overall combined-cycle SOFC system through the miniaturization provided by microchannel process technology (MPT).

MPT has been shown to be a viable alternative for reducing the size of heat exchangers and conventional chemical processing technologies. MPT utilizes arrayed microchannels to process mass and energy in bulk.[3] As the critical dimension of fluid channels are reduced, device size decreases as a result of shorter diffusional lengths permitting accelerated heat and mass transfer per unit surface area and an increased surface area to volume ratio.[3] These benefits allow the footprint and volume of diffusion-limited processes to be dramatically reduced. MPT has been demonstrated for various applications such as heat exchangers[4], chemical reactors[5], fuel reformers[6], and cooling systems[7]. The size and weight reductions available through MPT can result in cost reductions for components[8] manufactured from high cost alloys such as the waste heat recuperator discussed above.

Although MPT has been shown to be beneficial, high costs have been a barrier to application. Typically, MPT devices are fabricated using microchannel lamination (microlamination[3]) architectures involving patterning and bonding steps. Recent studies have shown that the economics of microlamination can be greatly improved at higher manufacturing production volumes[8],[9]. However, traditional photochemical machining and diffusion brazing steps do not scale well to high production volumes. Photochemical machining has poor material utilization and high consumable costs (photoresist and etchant reclamation) even at high production volumes while diffusion brazing is susceptible to low yields on hermetic bonds. Scalable microlamination methods have been studied as process alternatives for low temperature devices[10],[11]. However, little work has been done to drive down the costs of high temperature MPT components.

In this paper, a new microlamination architecture based on metal stamping and laser welding is introduced for the economical manufacture of a high temperature microchannel recuperator (HTMR). The concept of a microchannel flow insert (MFI) is developed to address resolution issues in the stamping of metal microchannel laminae. The lamina design is further simplified to reduce the amount of laser welding necessary to produce the device. Only the high pressure path within the device is hermetically sealed by laser welding. The low pressure path is defined by the outside of the high pressure array and a clamshell housing. The housing can be permanently sealed using laser welding or, alternatively, sealed using a high temperature gasket permitting the low pressure flow path to be accessed after operation to address operational issues such as channel clogging. Below, a rationale is provided for the design of the HTMR developed in this paper.

1.1 Typical MPT Manufacturing Process Flow

There are four general steps in the microlamination of MPT components: lamina patterning, laminae bonding, device singulation and device interconnect.[8] The most common manufacturing process flow for a MPT device consists of patterning the laminae with photochemical machining

(PCM), bonding the laminae through diffusion bonding or diffusion brazing, singulating devices by way of wire EDM, and adding fluid interconnects by TIG welding or brazing. Of these four main process steps, cost model studies have shown the largest contributors to device cost are the patterning and bonding steps.[8],[9]

Using this manufacturing architecture, microchannel laminae are often designed with small, blind, stand-alone islands of material called bosses or ribs. These laminae features are typically produced using PCM and are utilized to perform any one of three basic design functions. First, in order to combat flow maldistribution, ribs and small islands are used to direct flow across the lamina. Second, islands and ribs are used to prevent creep and other structural defects caused by high temperatures and pressures during the diffusion brazing and diffusion bonding cycles. In this regard, the location of the features provide more uniform pressure distribution to faying surfaces to promote hermetic sealing during bonding. Third, these small, blind, stand-alone features are used to prevent flow maldistribution due to elastic fin deflection or creep during device operation. In this manner, these island features largely help maintain the fluid channel height, a critical dimension in MPT development, during fabrication and operation.

Diffusion bonding involves clamping together the surfaces to be joined and heating for a sufficient time to enable solid state diffusion of atoms across faying surfaces. There are six important parameters in diffusion bonding: bonding temperature, bonding pressure, bonding time, surface roughness, surface cleanliness, and bonding atmosphere. Lamina faying surfaces must have low surface roughness and good cleanliness for bonding to take place. Diffusion brazing requires the addition of a melting point depressant interlayer on the bond line which generally relaxes all bonding requirements. Both diffusion bonding and diffusion brazing of microchannel laminae involve stacking and properly registering all required laminae inside a fixture, placing the fixture in a vacuum chamber, pulling a vacuum, increasing the temperature of the stack to a point that facilitates rapid atomic diffusion, and applying compression to the stack to ensure good fit-up of faying surfaces. In diffusion brazing, the interlayer melts at the bonding temperature and rapidly diffuses into the parent material or otherwise

fills voids at the bondline. While diffusion brazing requires the addition of an electroplating step, diffusion brazing is typically a more robust process with higher yields.

Economic efficiencies exist by batch production of devices at both the PCM and diffusion bonding steps. Batch production typically is performed using 24 x 24 inch panels. Subpanel device sizes enable multiple devices to be processed at each step. However, at the end of bonding, the devices must be separated from the bonded monolith via singulation. Common methods listed in order of best to worse surface and edge quality include wire electro discharge machining (wire EDM), waterjet cutting, laser cutting, and sawing. The final step required to manufacture an MPT device is to add interconnects that allow the device to be connected to common tubing. Common ways to add interconnects is to TIG weld or braze tubes onto connection points or half cylinders over layer headers.

1.2 Drawbacks of Typical Process Flow

The main benefit to the use of PCM is the ability to produce small, blind, island features as described above. However, as a machining process, PCM has poor material utilization extending below 50% on some designs which is problematic for MPT applications which typically demand the use of non-corrosive, high cost materials. Specifically, material utilization was about 55% for etched laminae on a comparative HTMR design developed at the Microproducts Breakthrough Institute (MBI). Also, consumable costs are high in PCM owing to the need for photoresists and etchant reclaim.[8] In order to move away from PCM, it is necessary to eliminate the need for the small, blind island features.

The width of the microchannel, or microchannel span, plays an important role in the performance of a microchannel heat exchanger both during fabrication and operation. Microchannel span is determined by the distance between ribs or island features. Therefore, in order to eliminate island features, efforts are needed to maximize channel spans. Excessive channel spans can cause fin deflections both during bonding and operation. If the span is too large, thermal warpage[12],[13],[14] or creep can take place during diffusion bonding. During operation, elastic fin deflection can take place

caused by differential pressure across fins. In either case, channel deviations of 10% can cause significant flow maldistribution leading to hot spots and poor heat exchanger efficiency[3] .

As previously discussed, a significant drawback to solid-state diffusion bonding methods is process yield. Because the various laminae are bonded together simultaneously, it is difficult to detect, repair and eliminate internal device leaks. However, a more important drawback to the use of solid-state diffusion bonding is that it requires the use of small, blind, stand-alone features on MPT laminae. For example, diffusion bonding cycle times can be long with a typical microlamination cycle taking in excess of 24 hours. This cycle time is a result of high stresses that occur within the device due to thermal gradients present during both heating and cooling cycles[12],[13],[14]. Fast cooling rates result in thermal warpage of fins and other unsupported spans. Therefore, to eliminate the need for islands, slow cooling rates are required. Cooling rates as low as 0.1°C/minute are often required for large (24 inch scale) devices incorporating islands which, for the diffusion bonding of superalloys, can require several days simply to remove it from the furnace at 400°C. A byproduct of these long cycle times is a decrease in the production capacity of the capital equipment leading to increased capital costs (which can be quite high). This approach to eliminating islands is impractical.

Further, for the diffusion bonding of 500[μm] thick stainless steel laminae, Paul et al.[14] established a fin aspect ratio (fin thickness over channel span) limit of 6:1 within the channel header region of a two-fluid microchannel device. Beyond this limit, lack of bonding pressure above and below channel headers resulted in unbonded regions and internal leakage between fluid streams. Therefore, in order to increase spans and eliminate islands, a bonding process different than diffusion bonding or diffusion brazing is needed with lower bonding temperature and bonding pressure.

As discussed above, another reason for islands involves managing differential pressure across a fin during operation. Typically this is in the form of a high pressure channel that will elastically deflect a fin into a low pressure channel. However, chiefly important for high temperature applications, differential pressures can affect the creep behavior of the fin. One means to eliminate the need for

islands in these cases, could be simply by increasing the thickness of the fin. But this approach increases the size and weight of the device. Therefore, rather than to eliminate the islands, the islands can be replaced through the use of a microchannel flow insert (MFI) as described in more detail below.

1.2.1 Design Methodology

Efforts were made to develop a HTMR design based on metal stamping (embossing and punching) and keyhole laser welding. Criteria for the selection of these process steps included material utilization, the cost of consumables and yield relative to the standard microlamination process flow described above. Metal stamping is a high-volume patterning process capable of embossing ribs, fins, or islands into thin shimstock and punching out through-holes. Unlike PCM, consumable costs can be low by spreading the costs of punch and dies over large production volumes. Further, material utilization rates in stamping is high because, as a forming process, there is little material removed during the generation of laminae features. The majority of material loss in stamping is due to the blanking step in which a net-shape part is punched out of a coil of sheetstock. In stamping, the thickness of the starting shimstock must only be as thick as the desired fin width, providing raw material savings. Finally, stamping cycle times are much faster than PCM cycle times allowing for higher production capacities for equipment and tooling leading to lower labor and capital costs.

Stamping has not been used as a mainstream lamina patterning step for two reasons. First, embossing of ribs and islands on one side of the lamina causes an indent or valley on the opposite side. This can be a problem in circumstances requiring embossed islands or fins in the middle of the flow as it will cause the fin for the adjacent channel to have corresponding valleys that will change flow conditions and perhaps cause stagnation of flow. In addition, embossing features can nest requiring bosses from layer to layer to be offset to maintain contact between layers[10]. The second drawback to stamping is that the minimum island feature size is larger than that possible with PCM owing to the minimum bend radius allowed which is a function of the material thickness and material elasticity. This

reduces the density of island features allowed within a device, making stamping incompatible with the high bonding pressures associated with diffusion bonding and diffusion brazing.

Keyhole laser welding utilizes a focused laser beam to rapidly melt, coalesce and solidify two adjacent laminae yielding a lap weld. During weld formation, a “keyhole” exists within the center of the beam/material interaction caused by high power densities in the center of the beam which effectively vaporize the metal. The keyhole acts as a black body during laser welding, greatly increasing the absorption characteristics of the material. While temperatures within the keyhole are extreme, they last for only fractions of a second. Rapid solidification of the weldment leads to a minimal heat affected zone. For microchannel lamination, keyhole laser welding has many advantages over diffusion bonding or brazing. First, the cycle time of laser welding is potentially much lower leading to higher capacities for equipment and labor. Scan speeds of several hundred mm/sec are possible. To maximize capital equipment capacities, the length of laser weld paths must be minimized. Second, laser welding is performed one lamina at a time, providing an opportunity for in-process quality control to detect and repair failed welds. This can be an important consideration as the size of the device and number of laminae increases leading to larger and larger faying surface areas. The third, and most important benefit, is the localized high temperature and low bonding pressure required to bond the laminae. Prior work has shown that externally applied pressures on the order of tens of psi are all that are needed to ensure proper faying surface fit-up between microchannel laminae during keyhole laser welding and that pressures beyond this provide no improvement in weld quality.[15] This reduced pressure requirement eliminates the need for many of the structural islands and bosses formerly required in laminae designs. Because laser welding reduces the need for these structural features, metal stamping becomes more suitable for lamina patterning. The full manufacturing plan for the half-array HTMR can be found in appendix 7.1.

1.3 Half Array Lamina Design

The design of the HTMR involves two laminae containing welding bosses which, when interleaved with one another, produce a high-pressure half array (HPHA). The HPHA is then inserted within a housing having interconnects. The exterior of the HPHA and the interior of the housing form a low pressure half array (LPHA) into which microchannel flow inserts (MFI) are embedded in order to minimize channel deflection during HTMR operation. These two fluid arrays lead to the half array designation. Figure 1 shows laminae designs for a HTMR produced using conventional microlamination methods and a half-array HTMR produced using a new microlamination architecture. Because the microchannel flow insert (MFI) serves as the structural element within the LPHA, the number of required islands is reduced, simplifying the laminae designs and making the laminae more stampable. Both the HPHA and LPHA have channel sizes of 0.450[mm] in height.

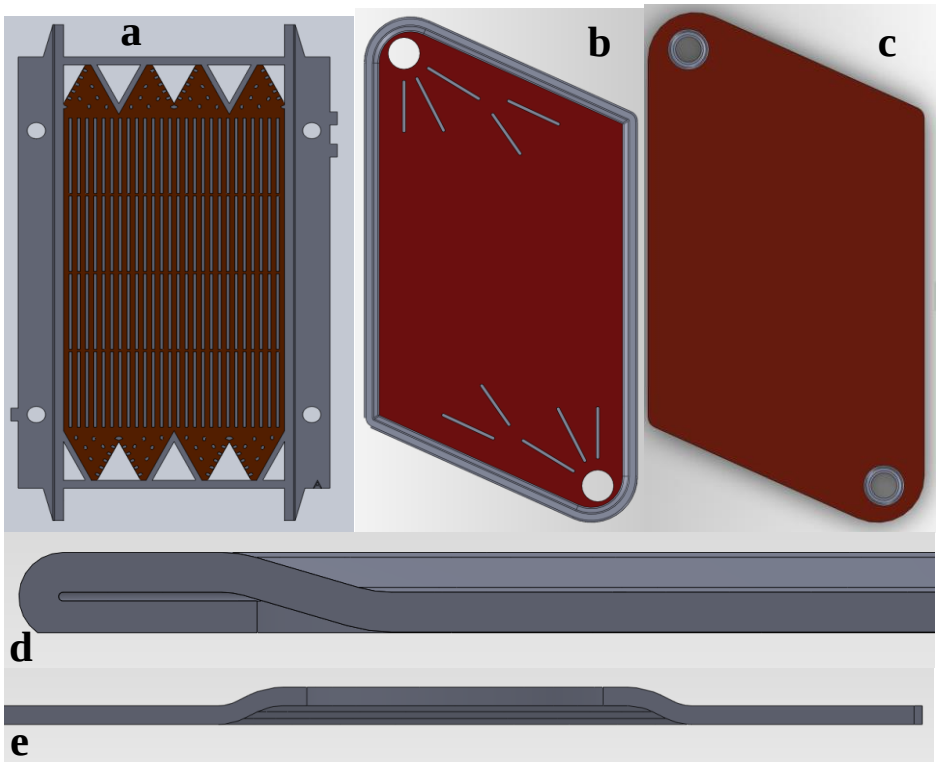

Figure 1: Lamina designs for the HTMR systems. Top views of (a) a representative lamina from the original HTMR design produced using PCM and laser welding; and (b) lamina A and (c) lamina B of the half-array HTMR design proposed in this paper. Also shown, (d) a cross section of the hemmed and embossed edge of lamina A which produces a fluid path and (e) a cross section of the header embossed into lamina B showing the raised feature and its corresponding valley.

Further, the periphery of the laminae is significantly changed as well. In order to block unwanted low pressure flow around the edges of the HPHA, hems were used on the edge of the foil to take up the unwanted space. This can be seen in Figure 1(d). Further, the faying surfaces required in keyhole laser welding are smaller when compared to diffusion bonding and diffusion brazing. Laser welding bosses on the exterior of the modified lamina A and around the header hole in lamina B define the welding path for hermetic sealing of the HPHA. Figure 2 shows the designed weld paths. As a result, the modified lamina designs only have one half the hermetic bonded area. The main reason for only bonding half of the array is to compensate for weld crown, shown in Figure 3, which is difficult to eliminate in keyhole laser welding. Weld crown prevents fit-up from one layer to the next. Consequently, every other layer must provide clearance for weld crown. In Figure 1(b) and (c), weld

crown clearance is provided by the embossed welding bosses or hems of adjacent layers. This architecture requires that no bonding surfaces (weld paths) directly overlap between layers. As mentioned, the overall reduction in island requirements improves the stampability of the laminae.

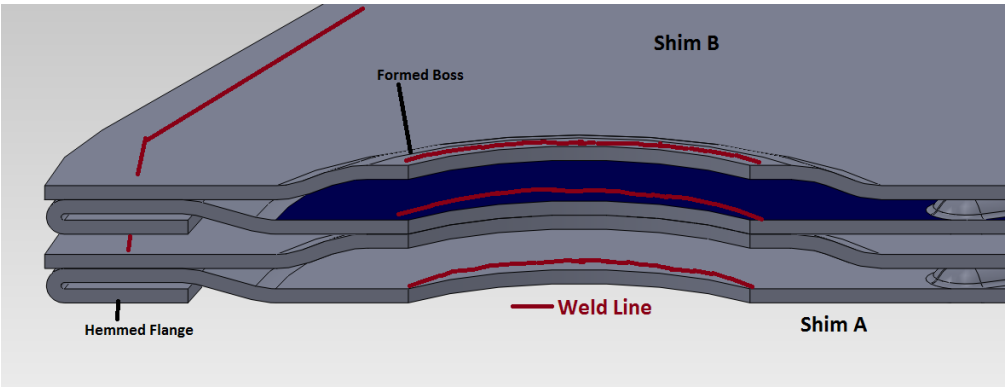

Figure 2: Weld design of the half-array design.

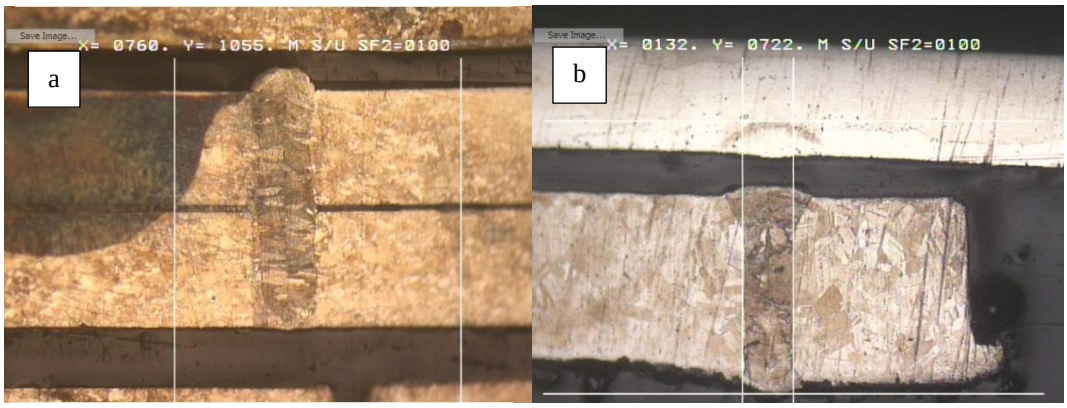

Figure 3: Example of weld defects that can prevent proper device function. (a) Weld crown that would prevent proper fit-up of the next layer given current MPT designs. (b) Failed weld due to a large gap. During welding, any initial gap between shims can be widened by the forces encountered during welding.

Finally, the exterior shapes of the laminae are also different. The shape of the modified laminae is to facilitate the formation of the LPHA by placing the HPHA within a housing (discussed below). In other words, the lower pressure channels are bounded by the exterior of the HPHA and the

interior of the housing. The tapered ends help to form headers at the end of the LPHA for distributing flow between and across low pressure channels (Figure 4).

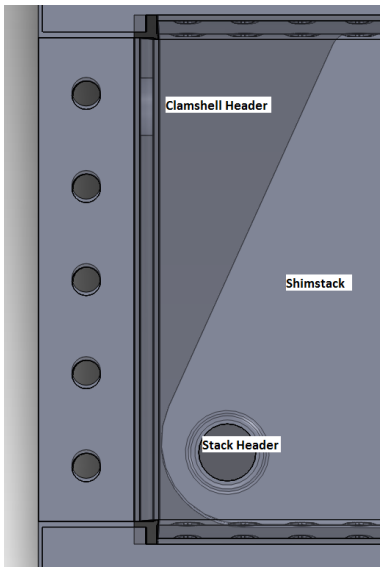

Figure 4: Visualization of the proposed LPHA header region produced by the tapered lamina ends.

1.3.1 Lamina Formability

Based on design requirements, 0.312[mm] thick Haynes 214 sheet stock was found to be suitable and readily available to form the two laminae designs. Two analyses were required to assess the manufacturability of the laminae; minimum bend radius and the expected drawing force.

1.3.1.1 Minimum Bend Radius

The minimum bend radius for a material is used to predict bending failure modes like cracking in the bend line. The minimum bend radius is found by Equation 1[16].

$$R_{min} = t\left(\frac{50}{r} - 1\right) \quad (1)$$

where R_{min} is the minimum bend radius[mm] t is the material thickness[mm], and r is the tensile percent reduction in area. For Haynes 214 r was found to be 53% from data provided by Haynes International, giving a negative value for R at all thicknesses. As a result, the minimum bend radius was not found to be a risk for cracking defects. This was important for the design of lamina A due to the hemmed edge requiring a near zero bend radius. To evaluate cracking in hemming, three samples of 0.312[mm] thick shimstock were hemmed and the external radial surface was analyzed under an optical microscope (Figure 5(a)). Striations capable of acting as crack initiation sites are shown even though no materials were found to fail. Since the role of the hem had no structural requirement, the hems were found to be suitable. The outside bend radius for bends in the MPTN (design described below) was also analyzed and did not show any striations. This can be seen in Figure 5(b). Figure 5(c) shows an MPTN with imperfectly formed peaks occurring mid strut.

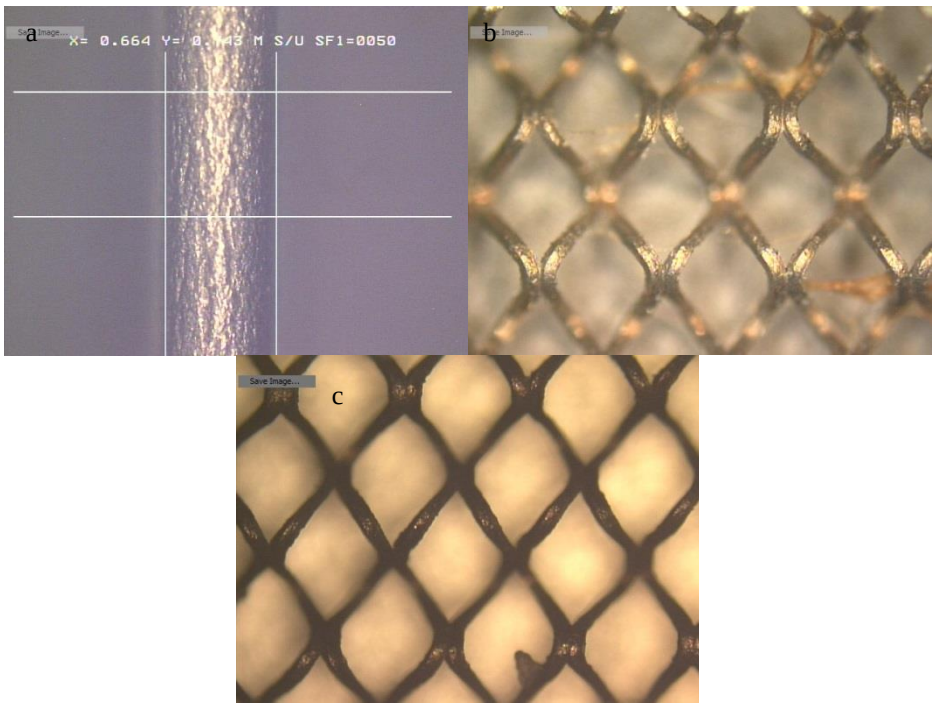

Figure 5: Micrographs showing (a) a hemmed edge of 0.312[mm] thick Haynes 214 sheetstock and (b) outside bends of the MPTN made from Dexmet expanded 0.076[mm] thick Haynes 214. (c) Poorly formed MPTN with bends occurring inconsistently with reference to the raw foil.

1.3.1.2 Drawing Force

The major drawback to the use of a high-temperature superalloy for the HTMR is that the high hot hardness and yield strength of these alloys promote rapid tool wear. To pattern both shim A and shim B of the HPHA an embossing step is required and can be modeled as a shallow deep drawing process. Drawing force is calculated in order to optimize tool design and minimize forming tool wear. Drawing force is estimated using the mechanics of beam bending and stretching. The maximum required drawing force can be estimated using equation 2 [17]

$$F_{draw} = \pi D_p \mathrm{t}(TS)\left(\frac{D_b}{D_p} - 0.7\right) \quad (2)$$

where F_{draw}=drawing force [N], D_p=punch diameter [m], TS=material ultimate tensile strength [Pa], D_P=punch diameter[m], and D_b =blank diameter[m]. In order to provide an overestimate of the forming force, D_p and D_b was estimated as the long dimension of the embossed area in lamina A. Table 1 provides typical material properties for Haynes 214.

Table 1: Material properties of Haynes® 214

Haynes 214 Material Properties		
Property	Room Temp	(900[C]
Ultimate Tensile Strength [MPa]	995	320
Yield Strength [MPa]	605	240
Youngs Modulus [Gpa]	218	151
Density [Kg/m3]	8050	8050
Thermal Conductivity [W/m-K]	12	31.4

The required forming force needed to generate the flow path on *lamina A* was found to be 46[kN]. To generate the embossed header on lamina B, the required force was found to be 5.9[kN]. These forces are much lower than the forces required to draw shapes such as a small aluminum can drinking cup (D_p=50[mm], t=2[mm], D_b=100[mm], F_{draw}≈108[kN]) owing to the hundred-micrometer scale thickness of the material. Further, tool wear is likely to be concentrated along the edges of the tool which would not significantly affect the critical dimension of microchannels (i.e. depth) assuming the channel width to depth aspect ratio is quite large (> 10:1) which is the current case. Due to the expense

of tool production, the tool wear and stamping characteristics of the laminae were not thoroughly investigated for the HTMR laminae in this work.

1.3.2 Shim Deflection during Operation

Due to the size scale of microchannel devices, it is important that the critical dimensions of the device (channel height) do not vary by more than 5%. Dimensional variation beyond this amount is expected to lead to flow maldistribution at a level to significantly reduce heat exchanger effectiveness.[3] For this reason, the microchannel fin deflection due to differential pressure across high pressure and low pressure channels was calculated to ensure proper device function. Although the MPTN design will be discussed in greater detail below, it is important to note that an idealized network will support the above shim in a regular pattern, allowing for a simple plate mechanics model to evaluate deflection. Equation 3[18] below was used for this estimate. This estimate was based on a plate with uniform pressure and simply supported edges.

$$\delta = C * \frac{\mathrm{w} * P^4}{E * t_{shim}^3} \tag{3}$$

where C is a constant depending on the plate geometry, w is the load on the plate, P is the pitch of the MPTN, E is the material Young's Modulus of Elasticity, and t_{shim} is the shim thickness. The maximum deflection was estimated as 9.6 [nm]. Although this equation will be an underestimate as the MPTN will only simply support the shim on the corners, the extremely low value found provides peace of mind that the device will meet functional criteria. A thorough analysis of deflection was not performed as it was not expected to be the main mode of device failure.

1.3.3 Pressure Drop across the HPHA

The pressure drop across the high pressure side of the microchannel array was required to be less than one psi (6.9[kPa]). Consequently, the HPHA was evaluated with regards to pressure drop.

Pressure drop through the HPHA was determined by summing the pressure drop through the interconnects, layer headers, channel headers and across the microchannel array. Pressure drops for 90 degree bends into and out of HPHA layers were also added. Figure 6 shows the flow of fluid through the HPHA. The Reynolds numbers found for interconnects and lamina headers are all well above the laminar flow transition range. Therefore the pressure drop through these areas was found from the Darcy-Weisbach equation below (equation 4), with the friction factor being estimated by the Churchill solution[19] (equations 5-7) to the Colebrook-White equation[20]

$$\Delta P = f\left(\frac{L}{D_h}\right) 2\rho V^2 \tag{4}$$

$$f = 8\left[\left(\frac{8}{Re}\right)^{12} + (A+B)^{-1.5}\right]^{\frac{1}{12}} \tag{5}$$

$$A = \left(2.457 \ln\left(\left(\frac{7}{Re}\right)^{0.9} + \frac{.27e}{D_h}\right)^{-1}\right)^{16} \tag{6}$$

$$B = \left(\frac{37530}{Re}\right)^{16} \tag{7}$$

where ΔP=Pressure drop[Pa], f= Fanning friction factor, L=flow length[m], D_h=hydraulic diameter[m], ρ=fluid density[Kg/m3], Re=Reynolds number $= \left(\frac{D_h Q \rho}{\mu A}\right)$, Q=volumetric flow rate[m3/s], μ=fluid viscosity[Pa*s], A=cross sectional area[m2], and e=roughness height[m].

The HPHA is a system of parallel flow paths so that the pressure drop across the array can be estimated based on the volume flow rate through a single layer [21].

Figure 6: Flow diagram for the HPHA

For any change in pipe diameter through fittings, the pressure change can be estimated using equation 8 below known as the Bernoulli equation[22], which has been simplified by assuming the energy change due to gravity is negligible. For corners, expansions, and contractions, the pressure drop is found from a relationship between the flow geometry, represented by a loss coefficient, K_L and the density and velocity of the fluid. This relationship is shown in equation 9[21] below. For a sharp corner, K_L is estimated to be 1.1[21]. The Reynolds number within the HPHA microchannel was estimated to be 0.017, with the channel headers estimated to be not much higher. This, combined with the high aspect ratio of channel width to height (>175), the pressure drop in all the HPHA flow regions can be estimated by the Navier-Stokes equations assuming steady state laminar flow between infinite parallel plates. The pressure drop is estimated by Equation 10[21].

$$\Delta P = \frac{K_L \rho V^2}{2} \tag{8}$$

$$\frac{v_1^2}{2} + \frac{\Delta P_1}{\rho} = \frac{v_2^2}{2} + \frac{\Delta P_2}{\rho} \tag{9}$$

$$\Delta P = \frac{3Q\mu L}{2H^3} \tag{10}$$

where *H* is the channel height[m]. In total, the pressure drop through the HPHA is found with the following equation 11:

$$\Delta P_{total} = \Delta P_{Inlet} + \Delta P_{LamH,in} + \Delta P_{lam} + \Delta P_{LamH,out} + \Delta P_{outlet} \quad (11)$$

Where ΔP_{total}= total P-drop, ΔP_{inlet}=HPHA inlet P-drop, $\Delta P_{lamh,in}$=lamina header inlet P-drop, ΔP_{lam}=lamina P-drop (including the channel headers and channel), $\Delta P_{lamH,out}$=lamina header outlet P-drop, and ΔP_{outlet}=HPHA outlet P-drop. The lamina header inlet pressure drop includes the vertical section of the inlet tubing along with the pressure drop associated with a sharp right angle bend. Using the fluid properties found for the cold, high pressure fluid shown below in Table 2, the pressure drop across the HPHA was estimated to be 3.57[kPa] or 0.52[psi], about half the 1[psi] design criteria. The contribution to the pressure drop from the interconnects and headering was found to be 99% of the total HPHA pressure drop. Pressure drop through the LPHA requires a discussion of the microchannel flow insert.

Table 2: Typical properties of the two fluids flowing in the HTMR used for predictive calculations

Fluid Properties		
	Cold(air)	Hot(Exhaust)
Temperature [°C]	209	900
Density[kg/m^3]	0.75	0.3
Viscosity[Pa*s]	2.64E-05	4.60E-05
Convective Heat Transfer Coefficient	208.51	535.9
Specific Heat [J/kg*K]	1027	1200
Thermal Conductivity [W/m^2*K]	.0386	
Volumetric Flow Rate[m^3/s]	0.03	.08

1.4 Microchannel Flow Insert Design and Characterization

In order to decrease the fin span and improve material utilization, a microchannel flow insert (MFI) was developed based on work by Queheillalt et al[23] and Desphande and Fleck[24] representing a micro-scale pyramidal truss network (MPTN). Figure 7 shows a schematic representation of the

MPTN describing physical variables. The MPTN is approximately 1/30th the size of pyramidal truss networks found in literature. Figure 10(a) shows an idealized 3D rendering of the MPTN design. The MPTN was designed to minimize deflection caused by the differential operating pressure between the high pressure and low pressure channels of the array. Further, by distributing the stress across many more supports, the MPTN can the maximum stress within the device during operation opening up the possibility for using cheaper, lower creep strength materials.

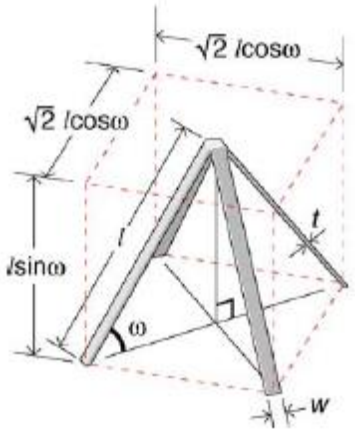

Figure 7: Schematic representation of a pyramidal truss network[23]

Although many iterations of the MTPN were generated before a truly feasible design was found, the first generation design, that which was built and tested, approximates an ideal MPTN meaning that the pitch(D_p), or distance between two nodes, in both x and y directions are the same ($D_{p,x} = D_{p,y}$). A second generation design is presented below that no longer fits this criterion and requires additional characterization analysis.

Two strategies exist for managing fin deflection due to the differential pressure across the fin. First, a slight interference fit within the microchannel can be used to pre-stress the MPTN elastically so that fin deflections are eliminated during device operation. However, these types of interferences were expected to make assembly of the HPHA difficult. Consequently, the MPTN was designed to have a stiff spring constant so that the differential pressure across the microchannel fin has little impact (< 5%)

on channel heights. It is important to note that the MPTN design presented here has no bonded nodes, and this will have a slight effect on the compressive response[25].

Based on the prior work of Queheillalt et al.[23] and Desphande and Fleck[24], the MPTN developed for this project was characterized with regards to compression strength, modulus of elasticity, pressure drop, Nusselt number, and creep life. The fabrication of the MPTN was evaluated using required bending force, springback, minimum bend radius, bend allowance, starting blank size, and dimensional tolerance. In some instances, experiments were required to evaluate the manufacturability of the design. Below, Table 3 summarizes the idealized MPTN design.

Table 3: Design parameters of the MPTN

Micro-Scale Pyramidal Truss Network	
Material	Haynes® 214
Material Thickness[t]	76[μm]
Strut Thickness[t_{strut}]	76[μm]
Designed Height[H]	450[μm]
Hydraulic Diameter[D_h]	810[μm]

1.4.1 Design Evaluation of Micro-Pyramidal Truss Network

The MPTN design was analyzed for five performance metrics; the network compressive modulus of elasticity, compression strength, pressure drop, Nusselt number, and creep life. These metrics are used to predict the devices performance during operating conditions and help improve design iterations.

1.4.1.1 MPTN Compressive Modulus of Elasticity

The ability to predict the MPTN compressive modulus of elasticity allows customization of the truss deflection under load. The compressive modulus of the MPTN was designed to minimize fin deflection due to the differential pressure across fins during operation. Deshpende and Fleck [24]

derived equation 12 to predict the compressive modulus (E_{33}) based on the strut angle (ω) and the relative density of the material ($\overline{\rho}$)

$$E_{33} = E\overline{\rho}\sin^4(\omega) \tag{12}$$

where E is the material Young's Modulus[Pa]. The idealized MPTN made of Haynes 214 results in a predicted compressive modulus of 1.6[GPa] under operating conditions. The relative density of the MPTN is calculated by equation 13[24].

$$\overline{\rho} = \frac{2wt_{strut}}{l^2\cos^2\omega\sin\omega} \tag{13}$$

where t_{strut} is the strut thickness[m], w is the strut width[m], and l is the strut length[m]. The relative density for the idealized MPTN was estimated as 0.11. Using the compressive modulus, a predictive value for network displacement can be found. The deflection was found using equation 14 and was calculated to be less than 1[μm], or less than 1% of the channel height.

$$d_{def} = \frac{w}{E_{33}} * h \tag{14}$$

where h is the MPTN height. This model was used by Biagi and Bart-Smith to predict the performance of truss-core sandwiches with bound nodes. They then performed an analysis to understand the correlation between mechanical performance and the amount of bonded nodes. This sensitivity analysis revealed a pyramidal truss network with 90% unbonded nodes shows a decrease in the measured modulus[25]. To simplify the results of their work, the authors presented their results in terms of normalized variables. For the compressive modulus of elasticity, the network modulus is divided by the relative density times the bulk modulus ($E_{33}/(E\overline{\rho})$). At 90% unbonded nodes, the normalized bulk modulus was found to be about 0.15. Extrapolating this further to 100% yields an estimated normalized modulus for the MPTN of 0.1. Using this value, the estimated modulus is found to be 1.7[GPa], which is in agreement with the model calculation shown in equation 12.

1.4.1.2 MPTN Compressive Strength

Although creep is the most likely mode of failure for the HTMR design, it is important to check that the MPTN will not fail by yielding or buckling under operating conditions. Deshpende and Fleck[24] derived Equation 15 to find the maximum compressive strength based on an expected failure mode of plastic yielding.

$$\sigma_{max} = \sigma_y \bar{\rho} \sin(\omega) \tag{15}$$

$$\sigma_{EY} = \frac{\pi^2 k^2 EI}{Al} \tag{16}$$

If elastic buckling or elastic yielding is expected as the failure mode of the MPTN, the material yield strength, σ_y, in equation 15 can be replaced with σ_B for buckling stress, or σ_{EY} for elastic yielding stress. Deshpende and Fleck[24] found that these failure modes are more likely to occur when the struts are longer than they are wide or thick based on the geometric relationship to compressive buckling. As the MPTN strut has a square cross section with a side dimension of 76.2[μm] and a relatively long length, it is expected that they will fail by elastic buckling, however after calculating the critical compressive buckling stress of the MPTN to be 22.51[MPa] using equation 16, we expect that the critical yielding stress is lower at 17.1[MPa]. *k* was assumed to be 1. Baigi and Bart-Smith also investigated this mechanical response in their sensitivity analysis. They found that a pyramidal truss network with 90% unbounded nodes shows a factor of 2 decrease in compressive strength[25]. At this percentage the normalized peak compressive stress ($\sigma_{max}/(\sigma_y \bar{\rho})$ was found to be about 0.4. Extrapolating this further yields an estimated normalized peak compressive stress for the MPTN of 0.3. Using this value, the peak compressive stress for the MPTN is estimated to be 7.8[MPa] providing a safety factor of nearly 8 at operating temperature and pressure.

1.4.1.3 MPTN Creep Life

The HTMR has a design requirement of either a 10 year service life, or low enough cost to afford intermittent replacement. Using Larson-Miller Parameter (LMP) data for Haynes 214, 0.05%

strain creep life can be estimated for a given internal stress. To perform a creep life analysis, likely failure modes must be considered in order to establish the maximum internal stress. Figure 8 shows three locations within the HTMR expected to experience large internal stresses. The system shown is a mix of the fin and the MPTN strut providing regions to note; these are average compressive stress within the strut, the contact stress between the fin and the MPTN, and the bending stress within the fin itself.

Figure 9 shows the estimated creep life for Haynes 214 at given stress values at the 900[°C] operating temperature based on the Larson-Miller Parameter (LMP) data supplied by Haynes international. It is important to note that this calculation is based on extrapolated data for any creep life beyond 1000 hrs. Using a safety factor of 2.0, it was found that the internal device stress should be kept below about 2[MPa]. This value was considered the creep stress criterion for this analysis.

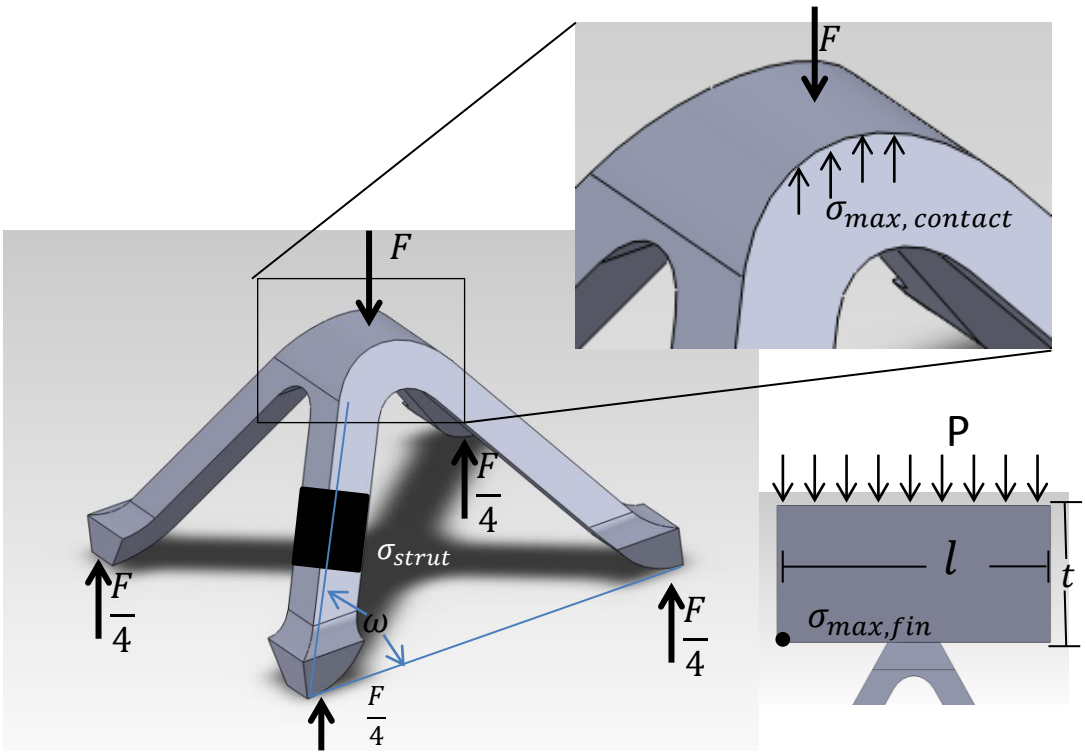

Figure 8: Various possible locations for the maximum internal stress within the device. Two additional stresses associated with contact are not shown for clarity.

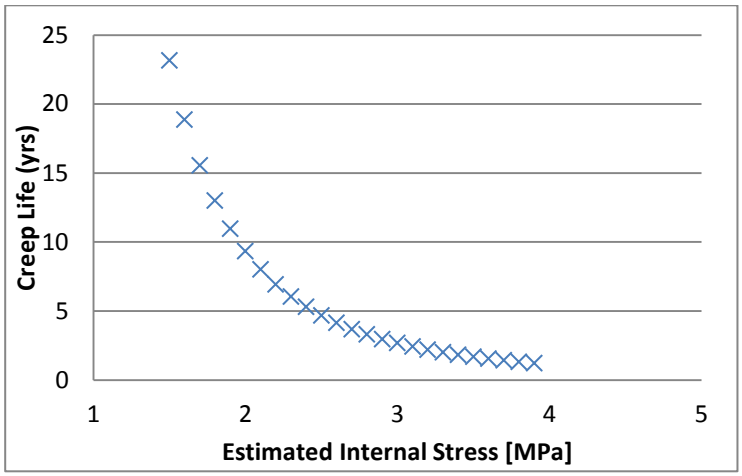

Figure 9: Estimated 0.05% creep life for the half-array HTMR design based on maximum internal stress within the device.

The maximum internal stress at the three locations was used as an input for the LMP equation in order to assess creep failure. Due to the periodic design of the pyramidal truss network, simple plate mechanics was used to provide an estimation of the maximum internal stress within the fin due to plate deflection. Assuming a square plate with simply supported edges (not corner supports), the maximum bending stress within the fin was found using equation 17[18].

$$\sigma_{max,fin} = \frac{\beta w P^2}{t_{shim}^2} \tag{17}$$

where β is a constant dependent on the length to width ratio ($\beta = 0.2874$ for a square plate). For the idealized MPTN, the maximum internal bending stress was estimated to be 0.767[MPa] which is significantly below the creep stress criterion established above. The average stress within the strut was found using equation 18.

$$\sigma_{strut} = \frac{wA_{unit}\cos(90-\omega)}{2A_{strut}} \tag{18}$$

where A_{unit} is the fin cross sectional area of an MPTN unit cell and A_{strut} is the strut cross-sectional area[m^2]. The stress is multiplied by 2 in order to account for the differential pressure being applied to both the top and bottom of the MPTN. Given the dimensions in Table 3, F_{strut} was found to be 0.21[N]

yielding an average stress within the strut of 33[MPa], far exceeding the creep stress criterion. As a result, the idealized MPTN results in a creep life of approximately 0.02 years.

There are three main stresses that are of concern for the contact region of the MPTN. These are the maximum compressive stress σ_C, the maximum tensile stress σ_T, and the maximum shear stress σ_S. Below are the equations used to estimate these stresses for a material with a Poisson ratio of 1/3[27]. In this case, the force (F) is found by multiplying the differential pressure by the area covering a single MPTN unit cell.

$$a = 0.7\left(\frac{FR}{E}\right)^{\frac{1}{3}} \tag{19}$$

$$\sigma_C = \frac{3F}{2\pi a^2} \tag{20}$$

$$\sigma_T = \frac{F}{2\pi a^2} \tag{21}$$

$$\sigma_S = \frac{F}{6\pi a^2} \tag{22}$$

In equation 19 R is the radius of contact. The compressive contact stress σ_C was estimated to be 6240[MPa] far in excess of the 2.0[MPa] creep stress criterion. The shear stress was found to be small with a value of 1.55[kPa].

Due to the nature of the contact stress, it is expected that creep in the contact region will occur until the fin contact has deformed enough to significantly increase the contact area between the MPTN and the fin, lowering the contact stress to a point below the creep threshold. Consequently, the creeping of the strut under compression was set as the expected failure mode. A proposed design change is presented in the future work section below capable of meeting the HTMR creep life design limit of 10 years.

1.4.1.4 MPTN Pressure Drop

Kim et al. established an empirical model for the estimation of the pressure drop for a fluid flowing through a tetrahedral truss network (TTN)[28]. Due to the anisotropic nature of a tetrahedral truss network, one flow direction closely resembles that of a pyramidal truss network, allowing the application of the predictive models to the MPTN design. In this model, based on a pressure drop dependence on form drag rather than viscous drag, pressure drop is calculated as a function of the Reynolds number of the truss network, which is found by Equation 23.

$$\mathrm{Re_{Dp}} = \frac{\rho \mathrm{U_{truss}} \mathrm{D_p}}{\mu} \tag{23}$$

where U_{truss}= the mean entrance velocity through the truss network[m/s] and D_p is the pitch (the length of one unit cell) of the pyramidal truss network[m]. A variation of the MTPN Reynolds number, Re_d, is to use the diameter of the truss strut as the characteristic dimension. In this case D_p is replaced with t for our network as our struts have a square cross-section. The MPTN in the HTMR flows the hot fuel cell exhaust. Properties for this fluid stream can be found in Table 2. Kim et al. established Equation 24 to find the pressure drop coefficient per unit cell for a truss network[28].

$$\mathrm{K_{cell}} = \frac{2\Delta \mathrm{P_{cell}}}{\rho * \mathrm{U}^2} \approx \frac{\mathrm{C}}{\mathrm{Re_{Dp}}} \tag{24}$$

where *C* is a constant dependent on the orientation of the truss network design. Kim et al. found that for the pressure drop for a flow orientation closely resembling a pyramidal truss network, C can be estimated to be 500. Because Kim et al. did their analysis with a TTN having $\overline{\rho} = .062$, it was expected that this value for C may decrease due to the increased density of the MPTN, and will require experimentation to improve the accuracy of the model. Manipulating equation 24 above offers one an estimate for the pressure drop through the network. This calculation yields the pressure drop for an individual unit cell. For a full MPTN network, the pressure drop is multiplied by the number of unit cells in the flow direction. For the HTMR, there are approximately 213 unit cells, yielding a pressure drop estimation of 92.2[kPa]. This exceeds the design requirement for pressure drop through the HTMR

device by over 13 times. A customization of the MPTN designed to meet the pressure drop requirement of the HTMR is presented in the future work section 0 below.

1.4.1.5 Nusselt Number for MPTN

Along with pressure drop, Kim et al. established a relationship between Nusselt number and Reynolds number for the tetrahedral truss network[29]. This empirical correlation is based on Re_d, assumes a constant Prandlt number (Pr) of 0.71, and is given by equation 25. They found that the heat transfer performance is not dependent on flow orientation, so only one correlation was presented. The MPTN offers increased mixing of the fluid around the struts, improving heat transfer. Indeed, Kim et al. in 2004[30] showed that flow mixing as a result of a truss network alone can improve the heat transfer performance of a heat exchanger (based on Nusselt number) by a factor of three. If the increased conduction area is accounted for as well as flow mixing, bonded nodes of a truss network can improve heat transfer performance almost seven fold when compared to a fluid channel containing no structures. Although the analysis by Kim et al. was performed on a network of different design, the trends in performance are applicable to any design of a truss network embedded in a fluid flow path. To roughly account for the unbonded nodes in the half array design, as well as to account for the difference in conductivity of Haynes 214 versus aluminum, a factor of 0.5 was included in the correlation.

$$\mathrm{Nu_d} = 0.5 * 0.428(\mathrm{Re}_d)^{0.56}\mathrm{Pr}^{0.36} \tag{25}$$

where Nu_d is the Nusselt number based on the MPTN strut diameter and the equation constants are found experimentally. For the MPTN design, the Nusselt number is estimated to be 1.77.

1.4.2 Fabrication of the Micro-Scale Pyramidal Truss Network

Due to the periodic nature of a MPTN, expanded metal foils lend themselves well as the starting raw material for the fabrication of an MPTN. Figure 10b is a micrograph of the expanded Haynes 214 metal foil supplied by Dexmet Corporation. Ideally, the expanded metal foil would be bent at the junction of the formed diamonds generating the peaks and valleys of the MPTN shown in Figure

10a. Consequently, a punch and die tool set (Figure 11) was designed to corrugate the expanded metal foil. Resulting geometry after forming can be seen in Figure 5 above. Initially the MPTN was designed with a slight interference fit. As a result, the MPTN forming calculations were based on an idealized 475[μm] tall network. This called for a 25[μm] interference. A raw material thickness of 0.0762[mm] was selected for the MPTN.

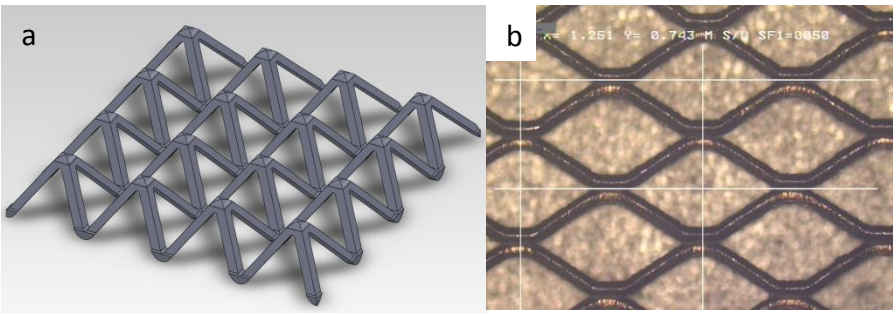

Figure 10: (a) An idealized 3D model of the micro-scale pyramidal truss network (MPTN); (b) Micrograph of the Dexmet Corporation supplied expanded Haynes 214. The vertical white lines represent the proposed bend line locations to produce an ideal truss network.

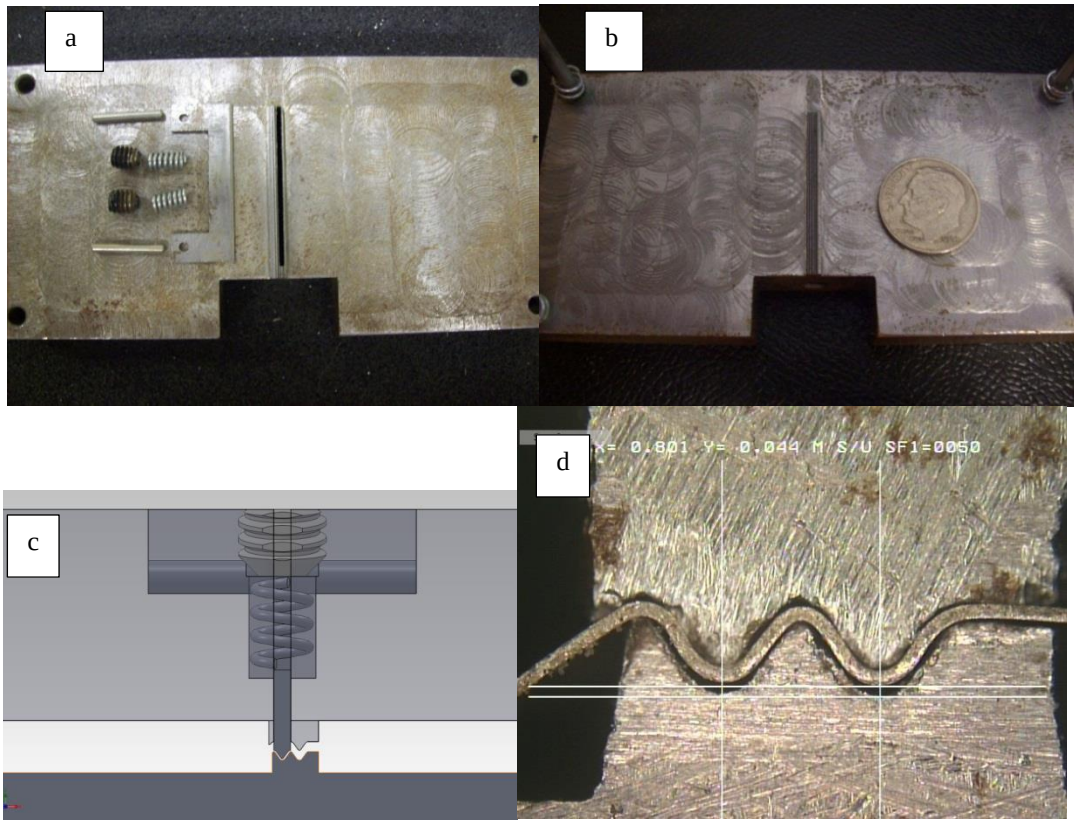

Figure 11: The corrugating punch and die built for MPTN forming. (a) Disassembled punch showing the spring-backed workholding insert assembly. (b) MPTN Forming die. The forming area is a small 5x26[mm] section in the center of the pieces. (c) a solid model showing the punch and die geometry. (d) a micrograph of the punch and die making contact with the material during forming.

The equation for required bending force is below. In this equation 26, K_{bf}=bending constant and $D_{opening}$=die opening width[m][17]

$$F_{Bending} = \frac{K_{bf} T S w t^2}{D_{opening}} \quad (26)$$

The die opening width was determined based on a MPTN pitch of 0.810[μm]. For v-bending, K_{bf}=1.33, giving a bending force of 1.7[kN]. This value theoretically overestimates the bending force as it assumes the diamond perforations are solid metal; however it also accounts only for the forming of one of the tool grooves. The second, indexing and workholding section, will add required force to the forming in order to ensure good contact between the workholding insert assembly and the raw material.

1.4.2.1 Bend Allowance and Starting Blank Size

Bend allowances (A_b) are used to find the initial blank size required to achieve proper size tolerances after bending. For the MPTN, the bend allowance was also used to properly size the diamond dimensions of the raw expanded foil. The bend allowance for v-die bending is found in Equation 27[17].

$$A_b = 2\pi\left(\frac{\alpha}{360}\right)(R + K_{ba}t) \tag{27}$$

where α is the bend angle, *R* is the bend radius [mm] and K_{ba} is the k-factor for bending. For v-bending, K_{ba}=0.42. The MPTN has a bend angle of 126^0 and a bend radius (limited by machining capabilities) of 0.075[mm], resulting in a bend allowance of 0.235[mm]. Using this value to find the starting blank size for a single diamond in the raw material will yield the desired diamond dimensions. For this blank, 2 bends were considered (1 full bend in center of diamond, 2 half bends on edges). Equation 28 is used to find the blank size.

$$\text{Blank Size} = (n + 1)l + nA_b \tag{28}$$

where *n* is the number of bends and *l* is the bending strut length[mm] (distance between adjacent bends along the diamond edge). For an *l*=.4[mm], the diamond blank size was found to be 1.271[mm]. For the full-scale HTMR design, the truss network has final dimensions of 174[mm]x 84[mm] with the bend lines parallel to the long edge. This design results in *n*=213, giving a starting blank size of 174[mm]x 135.72[mm].

1.4.2.2 Springback

Springback is a result of the elastic behavior of metals. In v-bending, springback causes the final included bend angle to be increased. In order to account for springback, the material is bent beyond the designed bend angle a specific amount, so that upon load removal the material will relax to the desired bend angle. An estimation for springback can be found using equation 29[16]. In this equation, R_i is the initial bend radii[m] and $R_{f\text{ is the}}$ final bend radii. For the MPTN, the final bend radius

was estimated to only increase by .6[μm]. Experiments were conducted with the MPTN. The measured bend angle after forming (taken over 4 samples) was found to be 70.6° with a standard deviation of 2.7° compared to an original included angle in the die of approximately 72°. Consequently, the effect of springback on the final MPTN shape was neglected when designing the punch and die.

$$\frac{R_i}{R_f} = 4\left(\frac{R_i \sigma_y}{Et}\right)^3 - 3\left(\frac{R_i \sigma_y}{Et}\right) + 1 \tag{29}$$

1.5 Housing Design

The HTMR housing serves the function of hermetically sealing the low-pressure fluid from atmosphere. In general, the housing consists of two hollow rectangular halves that have thru-holes for interconnect alignment. For the HTMR, the preferred embodiment of the housing is shown in Figure 12. This housing design is generated by a deep drawing process that creates the hollow cavity. The housing is designed with bosses formed into the sides that are perpendicular to the flow direction. These bosses prevent flow bypass that could result given the loose achievable tolerances in stamping processes compared to those required for MPT devices. These bosses are also intended to help ensure proper part registration within the housing.

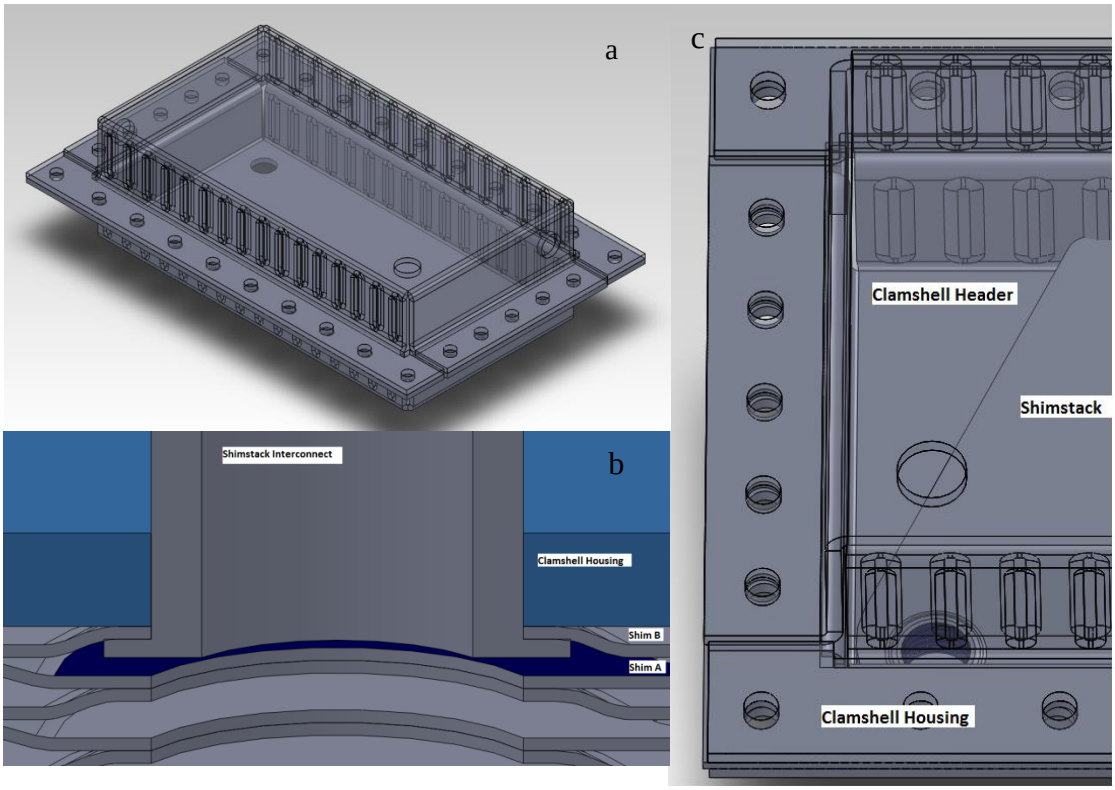

Figure 12: HTMR Housing design. (a) shows the assembled housing with the top half transparent for internal visualization. (b) Interconnect detail showing the interconnect-top shim-gasket-housing interface. A high temperature gasket is compressed between the top shim and the housing. (c) View of the housing showing the header created by the shape of the HPHA, or laminae stack. Also seen are the formed ribs along the edges used to help array registration and prevent flow bypass.

Because the formed shims are not rectangular, when inserted into the clamshell housing a large triangular plenum-like header is created for the low pressure fluid. This header acts as a lamina and channel header, reducing the required design work found for traditional MPT devices. The thickness of the housing was selected as 2.286[mm] based on a reasonable estimated forming force and economical material availability. Because the housing will be under positive internal pressure, housing deflection can have an effect on the useful life of the device as well as provide alternative flow paths for the low pressure fluid. A simple FEA analysis was performed in ANSYS Workbench to find the expected maximum deflection in order to estimate the occurrence of flow maldistribution around the HPHA stack. The maximum deflection was estimated to be 51 [μm] for a completely corrugated housing

including an additional transverse-corrugated external stiffening plate (Figure 13). For use in other high pressure applications, various other housing strengthening mechanisms could be employed like additional thick plate inserts.

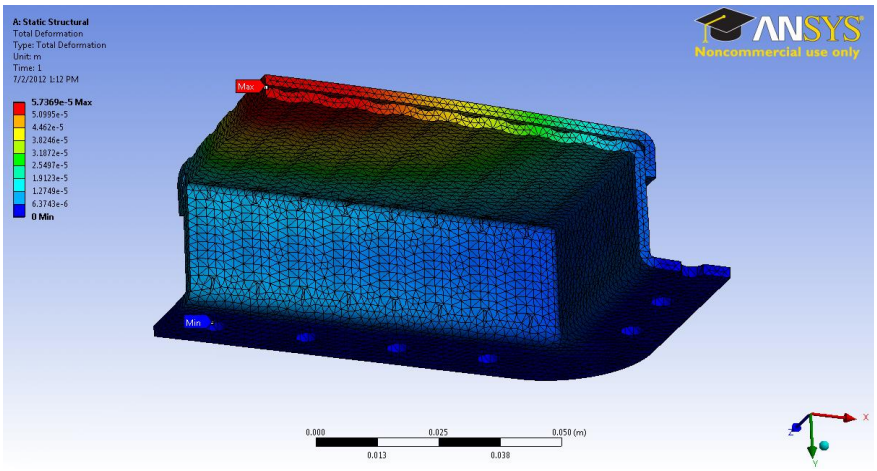

Figure 13: FEA deflection results of the clamshell hosing during operation.

Various values were calculated to explore the feasibility of drawing the housing. The worst case dimensions were used where the long dimension of the starting blank is the blank diameter(D_b), and the long internal dimension is the punch diameter (D_p). The drawing ratio(D_b/D_p) is 1.4, well below the standard limit of 2.0[17]. Additionally, the thickness($t_{housing}$) to blank diameter ratio was found to be 0.009, putting the design at risk for some potential drawing defects such as wrinkling. The drawing force required to form the housing half was estimated by using a worst case scenario with the drawing punch diameter estimated as the longest internal dimension. The maximum drawing force for the housing was found to be $1.2x10^6[N]$using equation 2. This operation would require a 500 metric ton press, which is a reasonable high volume manufacturing press size. In order to seal the housing, a high temperature ceramic compression gasket was designed to be stamped and used at the seam. The gasket material selected is Fibrofrax 110 paper.

1.5.1 Interconnects

Interconnects were designed for the HTMR in such a way that they would be compatible with a laser welding system. The designed interconnects are flanged 20[mm] ID tubing made of Haynes 214 high temperature alloy. The two high-pressure interconnects that attach to the HPHA are welded directly to the top and bottom shims, modified to have only one hole. A high temperature gasket is also used to seal the seam between the interconnect and the housing thru-hole. The low-pressure interconnects are welded directly to the Haynes 214 clamshell housing.

1.5.2 Pressure Drop Across the LPHA

The pressure drop for the entire LPHA must include not only the effects of the MPTN but also the effects of the fluid interconnects and the channel and layer headering. Figure 14 shows the fluid flow paths through the LPHA.

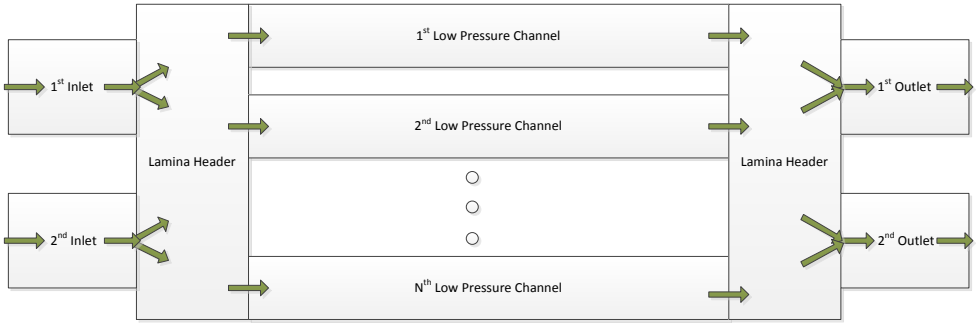

Figure 14: Fluid flow path through the LPHA

The pressure drop through this system is found by summing the pressure drop through the MPTN with the pressure drop estimated by equations 4-10. In order to maximize the allowable pressure drop through the various MPTN layers, the inlet and outlet interconnects were designed to be parallel to the MPTN flow direction. This eliminates any 90° bends, reducing the amount of minor pressure losses. While it is not straight forward to calculate the contraction loss coefficient for this system, an explicit relationship between the flow geometry and expansion loss coefficient is shown in equation 30 [21].

$$K_L = \left(1 - \frac{A_1}{A_2}\right)^2 \quad (30)$$

The K_L value for the contraction was found to be 0.464 based on Colebrook[20]. For this analysis, half of the low pressure fluid enters each inlet and expands into half of the inlet header. Using fluid properties given in Table 2 above, a pressure drop estimation for the LPHA was found to be 9.5[kPa] or 13.78[psi]. The interconnects and headering account for 0.02% of the LPHA pressure drop.

1.6 Heat Transfer Performance

The HTMR was designed to meet certain performance metrics, some of which have already been discussed (pressure drop and creep life). Two other design criteria were also to be met with the HTMR design. These two criteria are heat exchanger effectiveness, ε_{axial}, of at least 90%, and heat exchange duty of 15[kW]. Heat exchanger effectiveness is the ratio of the actual amount of heat transferred between the two fluids over the maximum possible amount of heat transferred. This is how the quality of a heat exchanger can be measured. An estimate for the HPHA Nusselt number was used to find the convective heat transfer coefficient for the SOFC inlet gas. This estimate, in conjunction with equations 31 through 34 below, was used to estimate effectiveness. These equations include an estimate for axial conduction in which energy is not transferred from fluid to fluid, but rather from fluid to outside environment through conduction down the fin length.

$$\lambda = \frac{k_{mtl} A_{mtl}}{L C_{min}} \quad (31)$$

$$\Phi = \left(\frac{\lambda * NTU}{1 + \lambda * NTU}\right)^{\frac{1}{2}} \quad (32)$$

$$\varepsilon_{axial} = 1 - \frac{1}{1 + \frac{NTU(1+\lambda\Phi)}{1+\lambda*NTU}} \quad (33)$$

$$NTU = \frac{UA}{C_{min}} \quad (34)$$

$$U = \frac{1}{\frac{1}{h_{hp}} + \frac{1}{h_{lp}} + \frac{t_{shim}}{k_{mtl}}} \tag{35}$$

where *U* is the overall heat transfer coefficient which is estimated by equation 35, *A* is the total heat transfer surface area of the device, C_{min} is the minimum $\dot{m}C_p$ of the two fluids, and , C_{max} is the maximum $\dot{m}C_p$of the two fluids. $\dot{m}$ is the mass flow rate of the fluid and C_p is the fluid specific heat. h_i is the convective heat transfer coefficient for either fluid and k_{mtl} and A_{mtl} are the material thermal conductivity and effective surface area. *L* is the flow length. The estimate for effectiveness came in at 90.02% and the overall heat transfer coefficient was estimated as 338 [W/m^{2}K]. Estimates for the convective heat transfer coefficient were based on the equation for Nusselt number shown below (equation 36).

$$Nu_i = \frac{h_i D_d}{k_i} \tag{36}$$

where *D* is the hydraulic diameter based on the strut thickness. For laminar flow through a rectangular microchannel with a constant axial heat flux, the Nusselt number can be estimated using a geometric correlation of $\frac{\sqrt{A}}{P}$ as presented by Sedeghi et al[31]. Equations 37, 38, and 39 were used to find an estimate for the high pressure fluid Nusselt number.

$$Nu_{\sqrt{A}} = 108.84(I_P^*)^{1.04}\left(\frac{\sqrt{A}}{P}\right)^{1.09} \tag{37}$$

where,

$$I_P^* = \frac{1+e^2}{12e} \tag{38}$$

$$e = \frac{H}{W} \tag{39}$$

where W is the channel width. To improve this model for future high temperature designs, the inclusion of terms in the effectiveness calculation to describe the conduction through any oxide layers that form will be required.

Duty is calculated based on the estimated effectiveness of the heat exchanger. This calculation is based on the desired temperature difference and C_{min}. This relationship is found in equation 40.

$$\mathrm{Q} = \varepsilon_{\mathrm{axial}} * \mathrm{C}_{\mathrm{min}} * \Delta \mathrm{T}_{\mathrm{inlet}} \tag{40}$$

where Q is the heat exchanger duty [W] and ΔT_{inlet} is the difference between the two fluid inlet temperatures. Based on this calculation, the HTMR is expected to have a duty of just below 16[kW].

2 Experimental Approach

Various experiments were carried out on the various design components to evaluate the feasibility of the half-array system. Experimental objectives, experimental designs, setups and protocols are discussed below.

2.1 Micro-Pyramidal Truss Network

2.1.1 Dimensional Tolerances of MPTN

The dimensional accuracy of the MPTN height was investigated as a function of forming force in order to find the minimum required force needed to produce the MPTN with good repeatability. Figure 15 shows the experimental setup for all MPTN forming experiments. To investigate the forming force, 5 strikes of the punch and die were performed at various forming forces. All forces were investigated on a single 20[mm] wide sample of the Dexmet expanded foil, long enough to accommodate a few millimeters separation between each formed section. Three height measurements were randomly taken at each forming force both on the edge of the sample and on a cross-section of the same sample.

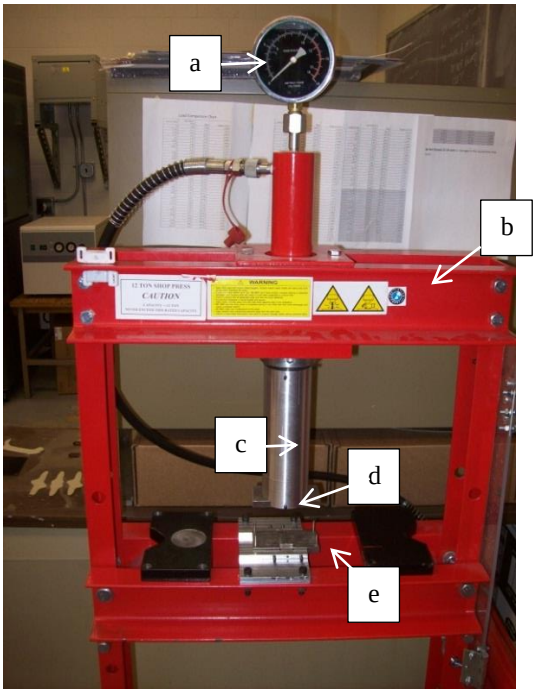

Figure 15: Experimental setup for all MPTN forming tests. (a) 160psi pressure gauge. (b) Rigid steel press frame built by Atlas Tools. (c) Punch support arm. (d) MPTN forming punch. (e) MPTN forming die.

To investigate the forming force, 5 strikes of the punch and die were performed at various forming forces. Between each set of strikes, the applied force was increased by approximately 3.1[kg] up to a final force of 50.0[kg]. All forces were investigated on a single 20[mm] wide sample of the Dexmet expanded foil, long enough to accommodate a few millimeters separation between each formed section. Three height measurements were randomly taken at each forming force both on the edge of the sample and on a cross-section of the same sample.

For final dimensional analysis, two MPTN dimensions were characterized: the formed truss pitch and the formed truss height. To characterize these dimensions, three separate strips of MPTN were formed at a forming force of at least 40.8[kg]. These formed sections were 20[mm] wide and 20[mm] long, with 10 height measurements taken from each.

2.1.2 MPTN Compression Response

The modulus of elasticity and compression strength of the MPTN were explored to validate the models described above. To test for the effect of work hardening on the MPTN, five 20[mm]x20[mm] MPTN samples were made and tested for compression strength. The compression tests were carried out on an Instron universal testing system (model number 5969) at room temperature.

2.1.3 MPTN Pressure Drop Tests

In order to evaluate the pressure drop across the MPTN, both welding hermeticity experiments and MPTN integration trials were needed. In prior work, Lajevardi[15] explored the required processing parameters to successfully weld Haynes 214 and found the need to penetrate at least half way through the bottom shim in order to provide joint hermeticity. For 0.312[mm] thick Haynes 214, Lajevardi found that hermetic welds were achieved with a laser power of 1000[W], a laser galvo-head raster speed of 600[mm\s] and a clamping pressure of 20[psi][15]. Although Lajevardi showed successful implementation of laser welding to the geometry described in this work, additional requirements were addressed in this study to ensure repeatability of the welding technique. Firstly, magnetic workholding was used rather than edge clamping to keep the shims in tight contact. This was required for multi-layer welding which was required to implement the technology demonstration vehicle (TDV) below. Also, degradation of the edge clamp surfaces, mainly weld spatter build-up, started to affect the fitup of the laminae which affected weld quality. Secondly, in order to improve shim fit-up during the welding process, pussy willow spot tack welds were performed prior to hermetic welds. These effectively tacked the shims together to help avoid deflection caused by the thermal gradients encountered during laser welding. Thirdly, methods were worked out to repair welds that leaked consisting of adding a weld line on the interior side of the failed weld.

All weld hermeticity and pressure drop test articles for the welding experiments were all square 29.4[mm] x 29.4[mm] samples of Haynes 214 designed for stamping but prototyped by

photochemical machining (PCM). All the test articles were designed to be stamped out of 0.312[mm] thick shim stock. The PCM prototypes consisted of a top shim with a thickness of 0.312 [mm] with welding bosses around inlets/outlets and a. The bottom shim with a fin thickness of 0.312 [mm] within the channel and 0.762 [mm] thickness on the edge. Test articles were designed to simulate the TDV test article below which was designed to be stamped out of 0.312 [mm] thick shim stock. The edge thickness was to simulate a hemmed joint.

Figure 16(b) shows the two shims used for the initial feasibility trial to work out the magnetic workholding. These 29.4[mm] x 29.4[mm] test articles (Haynes 214) used to evaluate weld hermeticity were designed for stamping but prototyped by photochemical machining (PCM). All laser welding was carried out using a 1000[W] 1.1[μm] continuous Yb fiber laser installed within a Rofin (Model FL 010) laser welding system setup in the galvo welding mode. Three of these test articles were welded and tested for hermiticity for each of the two weld designs (flange and boss) to demonstrate some level of repeatability using magnetic workholding.

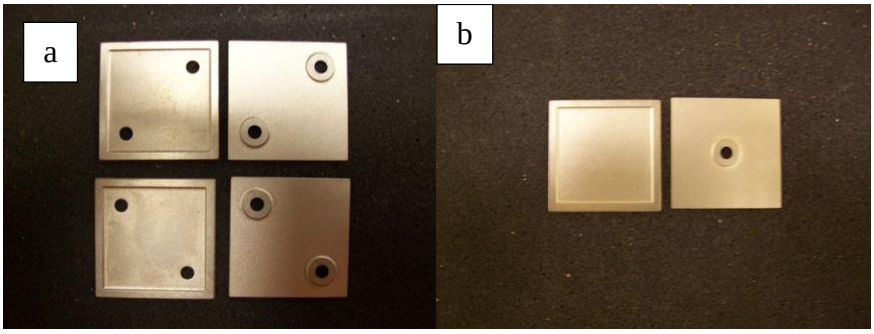

Figure 16: MPTN pressure drop and laser welding test coupons. (a) Two sets of unassembled laminae used to evaluate the pressure drop across a single MPTN, and (b) One set of laminae used to evaluate the hermeticity of laser welds produced using magnetic workholding.

Figure 17 shows the final pressure drop test article used for evaluating the pressure drop of the MPTN. Figure 16(a) shows the two shim designs used for MPTN pressure drop experiments. To ensure that magnetic workholding would work for a multi-layer stack, two short stacks of these laminae were produced and tested for hermiticity. Two pressure drop test articles were produced. One with the MTPN oriented with the bend lines parallel to the flow path, and one without any MPTN installed.

Interconnects were laser-welded onto the inlet and outlet, and leaks were sealed with JB-Weld. A strap clamp was produced, designed to stop shim deflection as a result of pressurizing the test article. This part tightens down over the area which contains the MPTN but does not affect channel height.

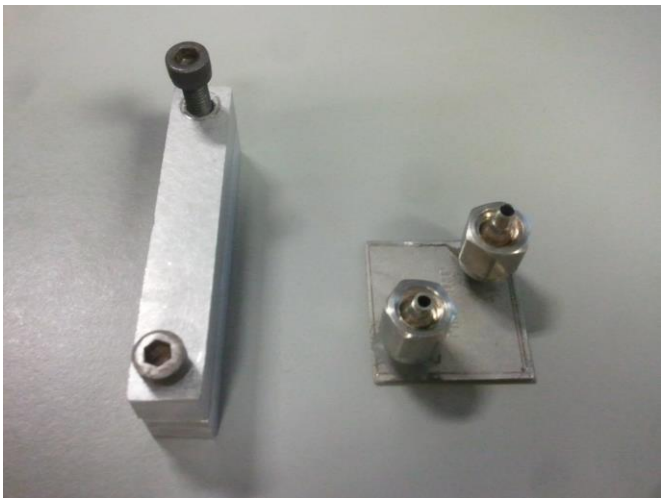

Figure 17: Photograph of the MPTN pressure drop test article (right) and the deflection clamp used (left).

As conceived, the idealized MPTN would have identical pressure drop measurements whether the fluid was flowing down the bend lines or perpendicular to them. Based on forming experience, it was found to be difficult to accurately align the pitch of the Dexmet foil with the pitch of the punch and die. Therefore, pressure drop experiments were carried out with the MPTN bendlines oriented parallel to flow to provide the largest open cross sectional area and the lowest pressure drop.

Pressure drop was found using a differential pressure reading taken from pressure transducers on the inlet and outlet of the test article. House air was controlled to various flow rates using a flow meter calibrated for air. Figure 18 shows the test loop design for these experiments. The pressure drop experiment involved passing air through the test articles setup on the test loop at various flow rates. To obtain the contribution to the pressure drop solely by the MPTN, the pressure drop from an empty test article (without an MPTN produced above) was subtracted from that of the test article containing the MPTN.

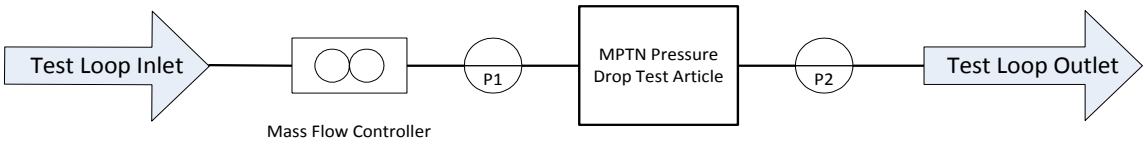

Figure 18: MPTN pressure drop test loop design

2.2 Functional Testing

The objective of this experiment was to evaluate the feasibility of implementing the half-array design described above. A sub-scale HTMR was designed, fabricated and tested as a technology demonstration vehicle (TDV) containing four sets of high pressure and low pressure flow channels.

2.2.1 TDV Testing

A TDV was built and installed in a test loop that mimics the conditions of the proposed HTMR system with regards to scaled flow rates and controllable differential pressure at high temperatures. The TDV was directly tested for pressure drop and heat exchanger effectiveness using a test loop shown in Figure 19 with insulation removed. Figure 20 shows a block diagram of the test loop design including individual measurement points. Temperature data was also used to validate models for predicting the heat transfer coefficient and the MPTN Nusselt number. The TDV was tested at a maximum temperature of 300[°C]. A combination of flow rates and fluid temperatures were selected in order to obtain a range of Reynolds numbers from 50 to 350 in order to capture the Reynolds number (≈250) of the full scale HTMR design.

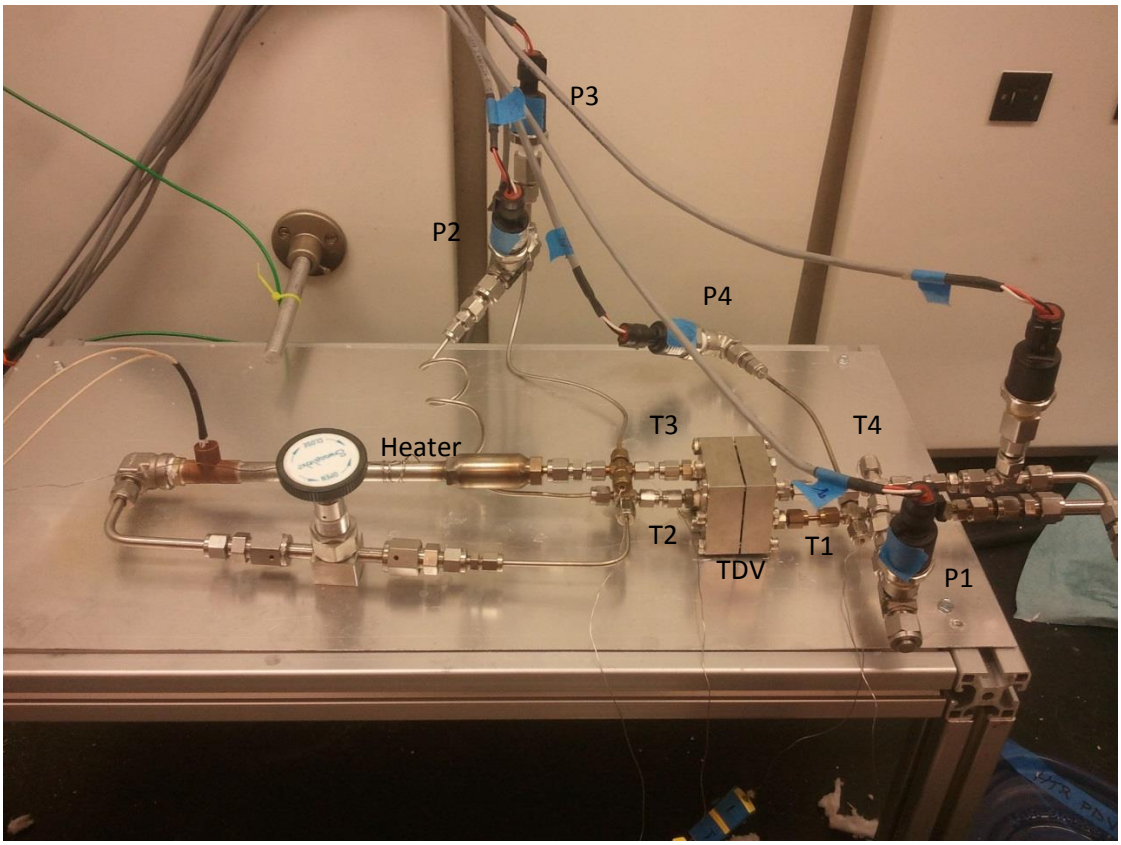

Figure 19: Final TDV test loop shown before insulating. Original design courtesy of The Pacific Northwest National Labs located in Corvallis Oregon.

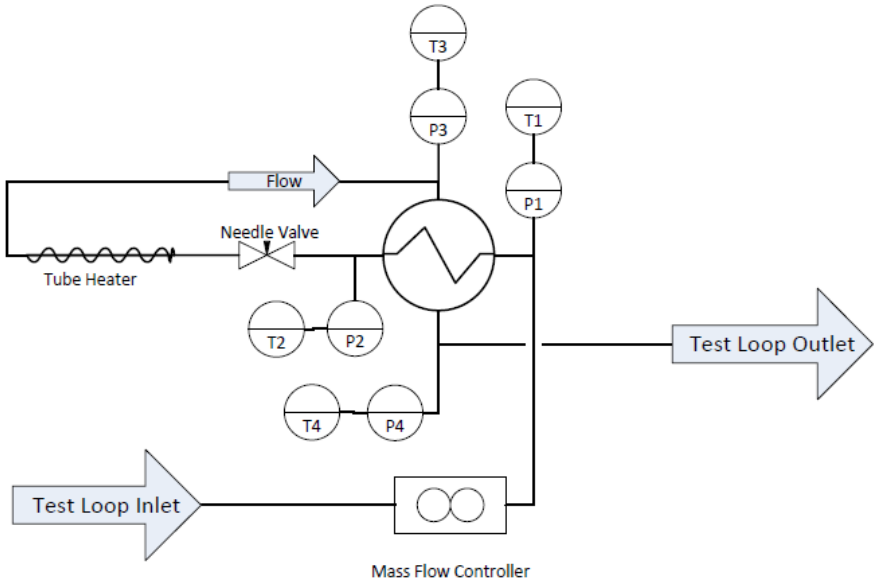

Figure 20: Block diagram of the HTMR TDV test loop. The heat exchanger represents the HTMR.

2.2.2 TDV Design

Due to the scale difference between the HTMR and the TDV, variations to the TDV fluid flow rates and differential pressures were made to match the Reynolds number of the HTMR. The TDV was tested with a constant low pressure inlet temperature of 300 [°C] at various flow rates.

Table 4 lists the test loop parameters. Due to the design of the test loop, the full scale HTMR operating differential pressure of about 50 [psi] was not achievable, so the highest differential pressure was used at each flow rate during TDV testing.

Table 4: TDV test loop temperatures and differential pressures at various flow rates.

Flow Rate [L/min]	LP Inlet Temperature [C]	Shim Differential Pressure [psi]	Low Pressure Half Array Reynolds Number
4.0	300	1.06	67
6.0	300	1.93	100
8.0	300	2.95	133
10.0	300	3.98	167
12.0	300	5.15	200
14.0	300	6.25	232
16.0	300	7.58	265
18.0	300	8.85	298
20.0	300	9.93	331

The pressure drop through the two fluid streams was found experimentally by subtracting the test loop pressure drop from the measured pressure drop. To find the test loop pressure drop, two short length tubes were inserted in place of the TDV and the pressure drop across these tubes was measured using the test loop setup above. The pressure drop of the test loop between the two pressure transducers was obtained by removing the pressure drop of the tubes from the overall pressure drop. These calculations are summarized in equations 41 and 42 below.

$$\Delta \mathrm{P}_{\mathrm{loop}} = \Delta \mathrm{P}_{\mathrm{measured}} - \Delta \mathrm{P}_{\mathrm{tube}} \tag{41}$$

$$\Delta \mathrm{P}_{\mathrm{FluidTDV}} = \Delta \mathrm{P}_{\mathrm{measured}} - \Delta \mathrm{P}_{\mathrm{loop}} \tag{42}$$

Where ΔP_{loop} is the pressure drop through the test loop between the two measurement points, $\Delta P_{neasured}$ is the measured pressure drop taken from the test loop, ΔP_{tube} is the pressure drop through the small diameter tube, and ΔP_{TDV} is the pressure drop through the TDV (either the HPHA or

LPHA).The tube used to replace the heat exchanger flow paths was 2.28[mm] diameter and 10[mm] long. Based on the calculated Reynolds number at the various flow rates, the flow through the tubes was both laminar and turbulent. For this reason, an estimation of 0.0045[mm] was used for the interior wall surface roughness used in calculating turbulent flow pressure drop. The Haaland solution (equation 43) to the Churchill-Whineboch equation was used for the estimation of friction factor through the tubes.

$$\frac{1}{\sqrt{f}} = -1.8\log_{10}\left(\left(\frac{\frac{\varepsilon}{D}}{3.7}\right)^{1.11} + \frac{6.9}{Re}\right) \tag{43}$$

The prediction of the pressure drop performance was carried out in the same manner used for the full scale HTMR design and includes all headering required. Due to the TDV design, both fluids enter the housing at right angles to the fluid channels, so 90º elbow calculations were included in both fluid pressure drop equations.

The performance of the heat exchanger was analyzed for effectiveness, Nusselt number, and heat transfer coefficient of the MPTN fluid path. This data was then compared to predicted data. Due to the inability to take temperature measurements along the flow length, calculations were performed using average temperature fluid properties; specifically values for thermal conductivity, specific heat, dynamic viscosity, and density.

Using the measurements taken from the TDV test loop, imperial values for heat exchanger effectiveness, duty, Nusselt number, and convective heat transfer coefficient were calculated. In order to find *Q* and U, equation 44 below was used.

$$\frac{(\dot{m}C_P\Delta T)_{hot}}{A} = \dot{Q} = U\Delta T_{LTMD} \tag{44}$$

where,

$$\Delta T_{LTMD} = \frac{\Delta T_A - \Delta T_B}{\ln\left(\frac{\Delta T_A}{\Delta T_B}\right)} \tag{45}$$

Based on the calculated estimate for *U* and the convective heat transfer coefficient for the high pressure fluid, an estimate for the low pressure fluid convective heat transfer coefficient was found using equation 46 below.

$$h_{LP} = \frac{1}{\frac{1}{U} - \frac{1}{h_{HP}} - \frac{t_{shim}}{k_{mtl}}} \tag{46}$$

This estimate was then used to find the low pressure fluid Nusselt number.

Experimentally it was found that the high pressure fluid has a lower $\dot{m}C_p$, so this fluid was used in estimating the heat exchanger effectiveness in equation 47 below. In order to take our results and compare them better to a device with perfect insulation like our equations predict, a prediction of heat loss was added to the effectiveness estimate. This addition takes into account all heat loss, but due to little or no leakage between fluids and similar specific heats for the fluids, it is assumed that the majority of the heat loss is due to natural convection in air through the device housing and surrounding insulation. The delta T in this portion of the equation was found as the difference in the delta T of the two fluids.

$$\varepsilon = \frac{(\dot{m}C_P\Delta T)_{cold} + (\dot{m}C_P\Delta T)_{heat\ loss}}{(\dot{m}C_P)_{min} * (T_{hotin} - T_{coldin})} \tag{47}$$

2.2.3 TDV Fabrication

Due to the high costs of forming die sets, TDV laminae were produced using photochemical machining to simulate the geometry of the formed laminae (Figure 21(a)). Laminae were produced by photochemically-machining (Great Lakes Engineering) 0.762[mm] thick Haynes 214 sheetstock. Due to the scale of the TDV (50.8[mm] x 50.8[mm], the flow directing bosses (Figure 1) were not included in the etched lamina A design. The hemmed flange on the edge of lamina A was represented by an un-etched edge on lamina A. For lamina B the important feature is the large boss that forms the header and

sets the channel height for the low pressure fluid. This feature was generated by etching both sides of the shimstock.

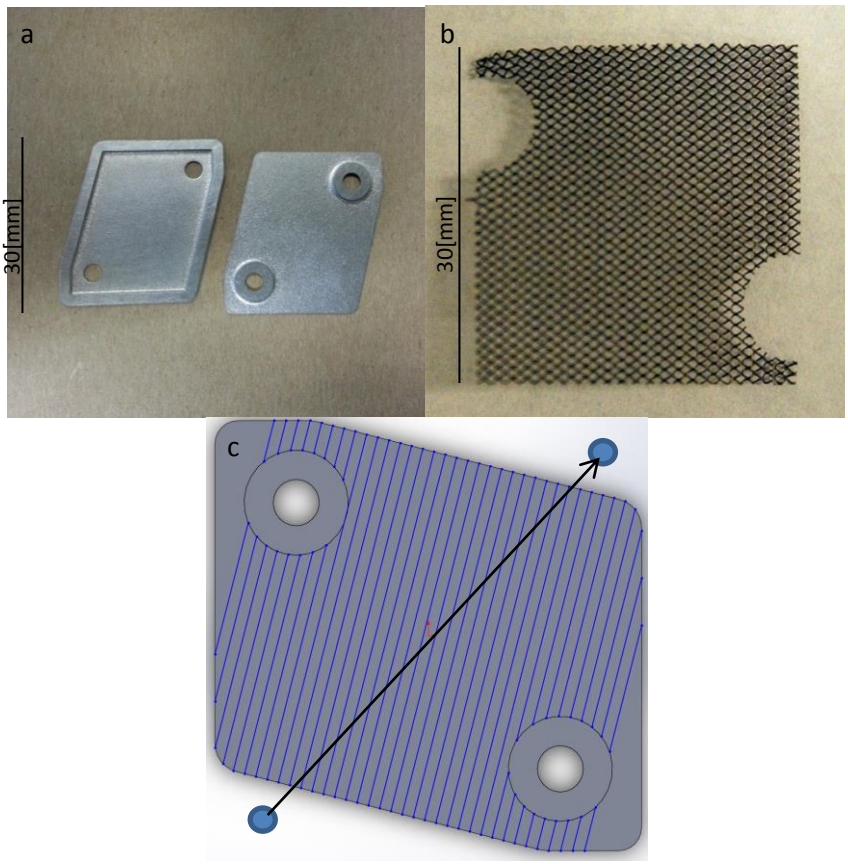

Figure 21: TDV parts that make up the HPHA. (a) Two PCM laminae (shims) made to mimic the embossed laminae designs. (b) Laser cut MPTN network. (c) Shows the approximate orientation of the MPTN bend lines relative to the flow path with the arrow indicating the flow direction from fluid inlet to outlet.

The MPTN within the TDV is the same design as that for the full scale design. Cutouts in the MPTN are used to mate with the interconnect bosses on lamina B in order to locate the MPTN during lamina welding and operation. A 5[W] pulsed 355 nm Nd:YAG laser on a ESI 5330 laser processing workstation was utilized to cut the MPTN layout. A sample MPTN used in the TDV fabrication can be seen in Figure 21(b). Figure 21(c) shows the orientation of the MPTN bend lines relative to the orientation of the fluid flow.

Laminae were hermetically welded within the same laser welding setup discussed above. An in-process method of weld hermiticity testing was developed to test all welds performed. The design of the clamp allowed testing of devices of any number of unit cells. Figure 22 shows the apparatus developed. This apparatus seals the four inlet/outlet ports by compression using o-rings connecting one of the ports to lab air and the other three ports to dead ends. Air leakage from the test articles was checked by immersing the device within a beaker of water. All samples were tested to 80 [psi] and left to settle for one minute to allow microscopic pin-hole leaks to become apparent.

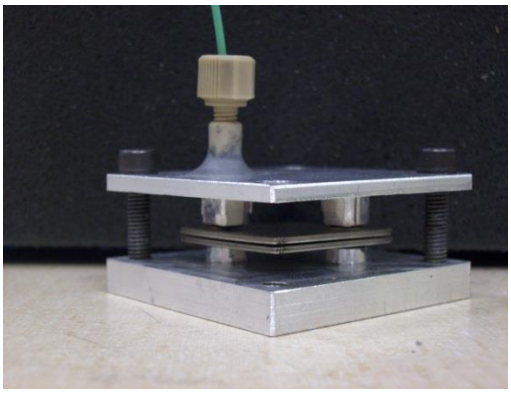

Figure 22: In-process hermiticity testing of the first two unit cells of the HPHA.

The TDV housing was machined from solid 316 stainless steel barstock by Viper Northwest in Albany OR. The 316 stainless steel was selected due to the lower temperature requirement of the test loop, and due to availability and cost of thick Haynes 214 barstock. The TDV housing was designed to be assembled and disassembled. Graphite gaskets were made by laser machining a 1/16” thick compressible high temperature graphite sheet. The resulting gaskets were used to seal the housing and interconnect seals. Figure 23 shows the TDV before and after final assembly.

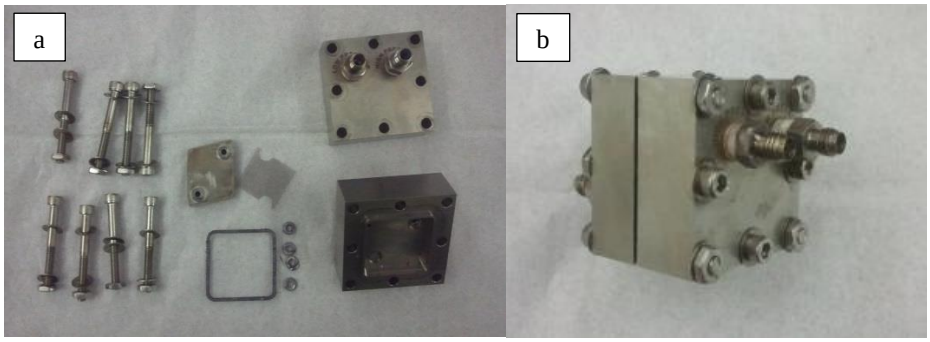

Figure 23: The Technology Development Vehicle before (a) and after (b) assembly.

It was originally planned to have interconnects that mimic the full scale design: Haynes 214 flanged tubes laser welded to the housing. Due to the limited availability of Haynes 214 roundstock and the difficulty in machining the material, the fluid interconnects were made using high-temperature compressive gaskets and NPT Swagelok pipe fittings.

3 Results and Discussion

3.1 Micro-Pyramidal Truss Network

3.1.1 Dimensional Tolerances of MPTN

Dimensional tolerances of the MPTN as a function of forming force were explored in order to find the minimum required force needed for each bend. Figure 24 shows the formed height response as a function of forming force. The formed height approaches 420[µm] at about 337[N] and increases in accuracy and precision beyond about 399[N]. At 399[N] and beyond, the average truss height was found to be 0.416[mm] with a standard deviation of 29[µm]. The coefficient of variation (CV) of the channel height was calculated to be just below 7% which is close to the desired CV of 5%. The measured pitch was 0.803[mm] with a standard deviation of 19[µm]. The measured pitch was within 1% of the desired size of 0.810[mm], however the measured truss height was 12.4% smaller than the desired height of 0.475[mm].

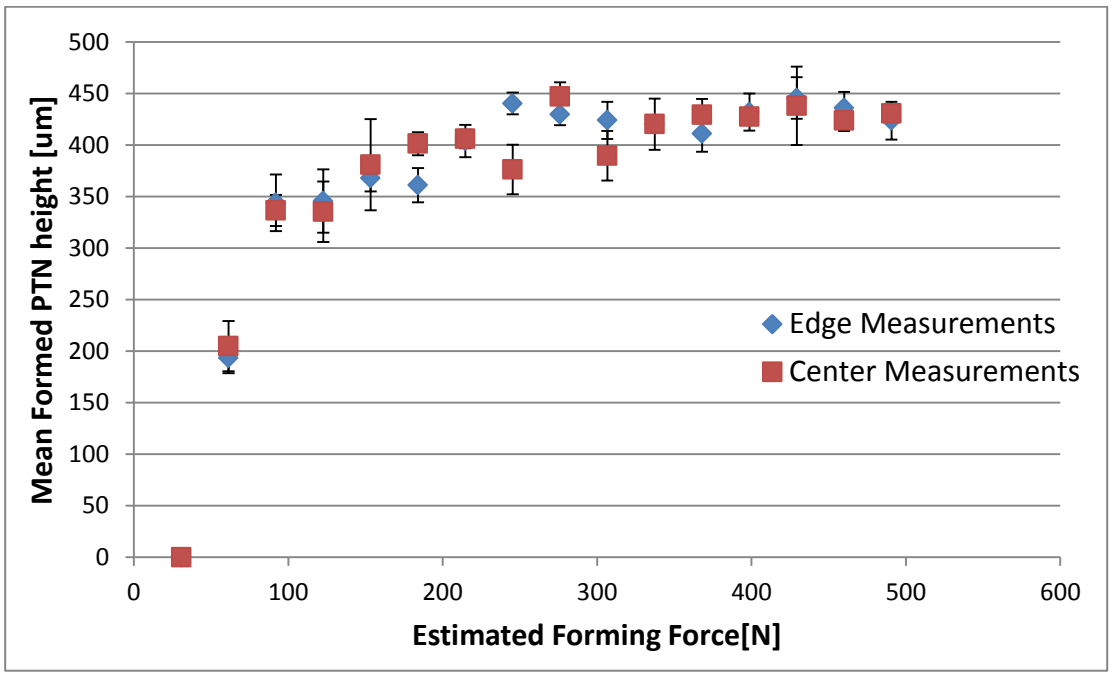

Figure 24: MPTN forming forces required to achieve a specific MPTN height.

One source of the height error was likely due to inaccuracies in the forming tool. Figure 25 is a Zescope 3D optical image of one of the die surfaces showing the depth of the first die feature (right) to be shallower than that of the second feature (left). This was done to reduce the forming stresses for the first feature which required taking the material from flat form to net embossed form. However, the top picture in Figure 25 shows a top view of embossing die which clearly shows that the distance between peaks and valleys varies.

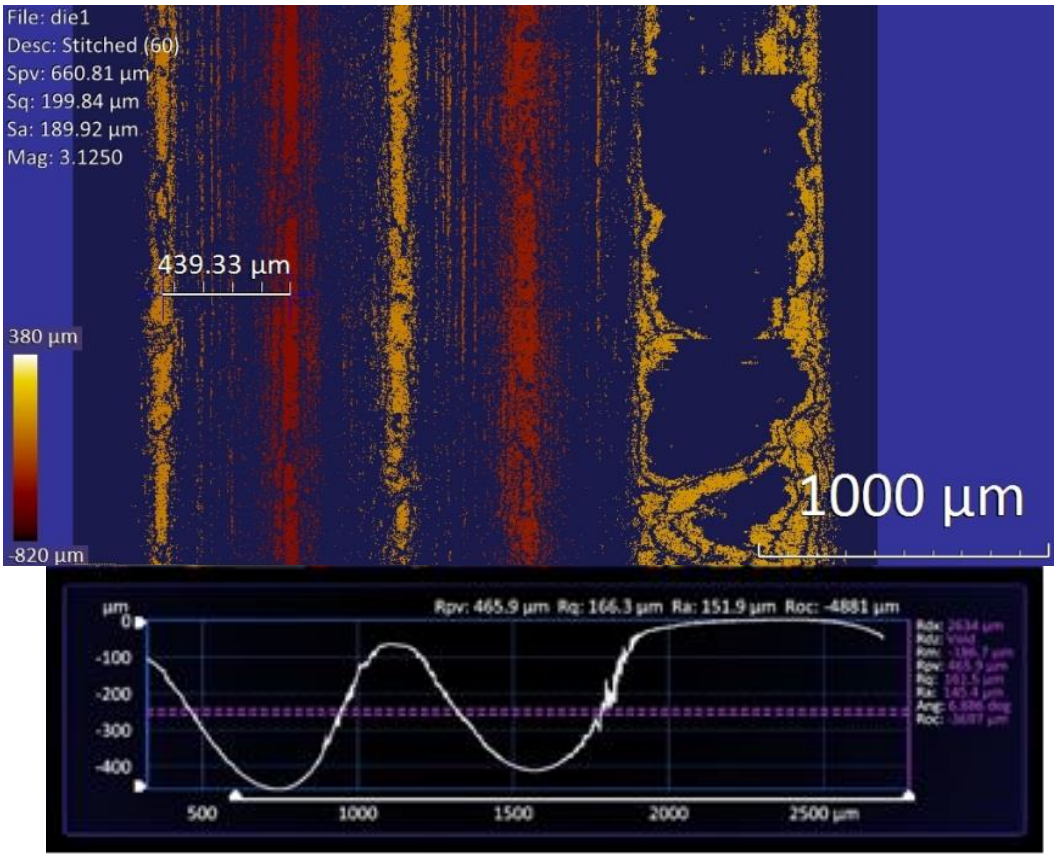

Figure 25: Zescope image showing the variation in die peaks and valleys, combined with die profile

Another source of the height inaccuracies of the truss network was attributed to tool wear. Figure 24 shows a slight trend of decreased truss height with an increase in force which tracks with the chronology of experiments. The punch and die were built of mild steel and were produced using traditional micro-milling techniques. Due to the high strength of the Haynes metal compared to the mild steel, it is expected that the tight radius corners of the punch and die were rounded off over time.

Compounding this was the inaccuracies in the forming die discussed above which likely would have caused more friction between the mating die sets and accelerating tool wear in certain areas of the die. This is consistent with the fact that the force required to produce the truss networks was considerably higher than expected (discussed in more detail below).

Other sources of height inaccuracies can be attributed to incomplete die fill during forming or springback. As shown above in Figure 11(d), a 44 μm gap can be seen between the formed material and the punch and die tooling. These measurements were taken with forming pressure and, therefore, represent the gap due to incomplete die fill. Bend angle measurements were taken on the truss within the die cavity and after forming (Figure 26). As mentioned above, springback measurements revealed no appreciable springback.

Figure 26: Bend angle measurements taken during forming (left) and after forming (right).

Another important discussion is the periodicity of the network in both the x and y directions. All of the pitch and height measurements were taken viewing down the bend line and not across it. In Figure 5(b) above, it can be seen that the peaks of the bends do not properly align with the proposed bend lines along the diamond crossings. This led to the "X" of the mesh not being on top of the hills and valleys but somewhere in between which likely affected the flow and mechanical characteristics of the MPTN. These dimensional variations were due to the inability to properly align the pitch of the expanded metal foil with the pitch of the punch and die.

As suggested above, our initial estimates of the required V-bending force showed an expected force of only 118.4[N] which is about one-half to one-third the force required. The additional force is likely due to excessive friction within the die in part caused by improper fit-up of the punch and die. Evidence of this can be seen in examining one of the die faces using the optical profiler as shown in Figure 25 above. The fit up problem extends out of the non-equivalent distance between peaks and valleys of the forming tool surface suggesting the need for better positional tolerance in producing the forming die.

From the forming results, the height of the truss network provided an average of 0.034[mm] clearance within the channel. Plate mechanics (rectangular plate, simply supported sides) calculations of the TDV fin deflection under load at 300°C estimates a central maximum deflection of 0.224[mm] suggesting that the shim will make contact with the truss network during TDV operation.

.

3.1.2 MPTN Compressive Response

Figure 27 shows the stress-strain curves obtained for each sample compressed. The predicted compressive stress for the network tests was calculated to be 19[MPa] while the measured compressive strength was found to be 10.2[MPa] based on the onset of plastic deformation. Looking at the graph below, the response appears to be fairly linear up to about 15 MPa and above. Assuming this is an elastic response, this is much closer to 19 MPa than the 10.2 MPa provided by the Instron software. The measured modulus of elasticity is over an order of magnitude different than the predicted model. However, based on empirical results seen in Figure 27, the expected network deflection given the operating pressure yields only a deflection of 6.6[μm] which is less than determined by finding the percent strain expected by the network under load, calculated by dividing twice the differential operating pressure by the average modulus of elasticity. This value was then multiplied by the height of the network (essentially 100% strain) to determine the height change expected at a given temperature and pressure. Because this experiment was performed at room temperature, to apply the results to the

HTMR design at 900[°C] a correlation was used to reduce the estimate. This correlation was based on a ratio of the bulk modulus at room temperature over the bulk modulus at 900[°C].

The variations in mechanical performance of the MPTN can mainly be attributed to the imperfect geometry of the MPTN as described above. This was exacerbated by the micro-scale dimensions of the MPTN compared with those in the literature with dimensions well above mm scale. For instance, the radius of curvature of the bends was nominally 150 µm which on both ends of the network takes up 300 µm for a span the length of 700 µm. That means over 40% of the span was curved compared to those in the literature in which the curvature did not factor. Further, the variations in the geometry discussed above all change the size and shape of the truss elements which would have a significant impact on the strength of the network. Finally, it is known that the mechanical properties of materials can vary significantly as the size scale of the feature approaches the material grain size which may have had some impact on the network response[32]. The MPTN samples analyzed under microscope had a material thickness to grain size ratio of approximately 3. Literature has shown a reduction in mechanical performance for sheet metal with a thickness to grain size ratio of 12[32], Future investigations are needed to evaluate the effect of geometry and material properties on the mechanical performance of the MPTN.

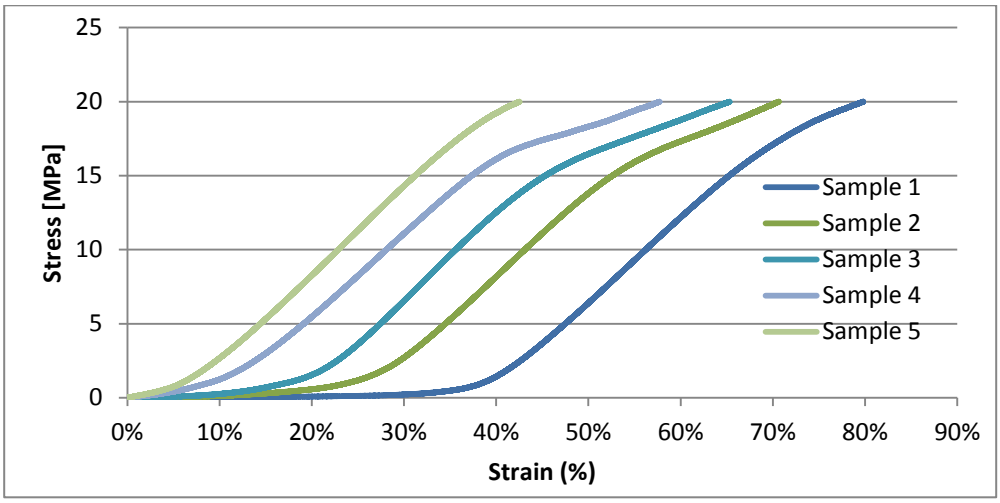

Figure 27: compression strength lines compressive response for MPTN5 different MPTNs. Results for sample 2 through 5 are offset for clarity

Even with the significant variation in the mechanical response of the truss network, the expected network deflection based on the empirical results above and the expected operating pressure yields only a deflection of 6.6[μm] which is less than 2% of the channel height meeting the design criteria for flow maldistribution[3], [13]. This deflection was determined by finding the percent strain expected by the network under load, calculated by dividing the differential operating pressure by the average modulus of elasticity. This value was then doubled to account for both stop and bottom fins deflecting. To correct the modulus for temperature effects, the modulus used was adjusted by a percentage equal to the ratio of the bulk material Young's modulus at room temperature and at operating temperature.

3.1.3 MPTN Pressure Drop

Figure 28 shows the experimentally determined pressure drop at various Reynolds numbers for a single layer device with MPTN inserted. The pressure drop experiments show a similar trend to the predictive models. It was stated earlier that these models were based on a similar, but not identical truss network design, and the constant associated with the model could vary depending on our results. To

improve model fit, it was found that a constant of C=250 reduces the average percent error from 162% to 31%. In the predictive equation, C is dependent on the amount of flow blockage encountered in the fluid flow path. As C decreases less flow blockage is encountered causing a reduction in local flow velocities. As mentioned above, the average height of the MPTN was about 7% below the intended height of the channel depth. As described in the approach above, a strap clamp was needed to minimize deflection of the sample fin during operation. These two observations suggest that there might have been significant distance between the top of the MPTN and the channel fin in the middle of the array for the fluid to bypass the MPTN. This might justify the reduction in C value.

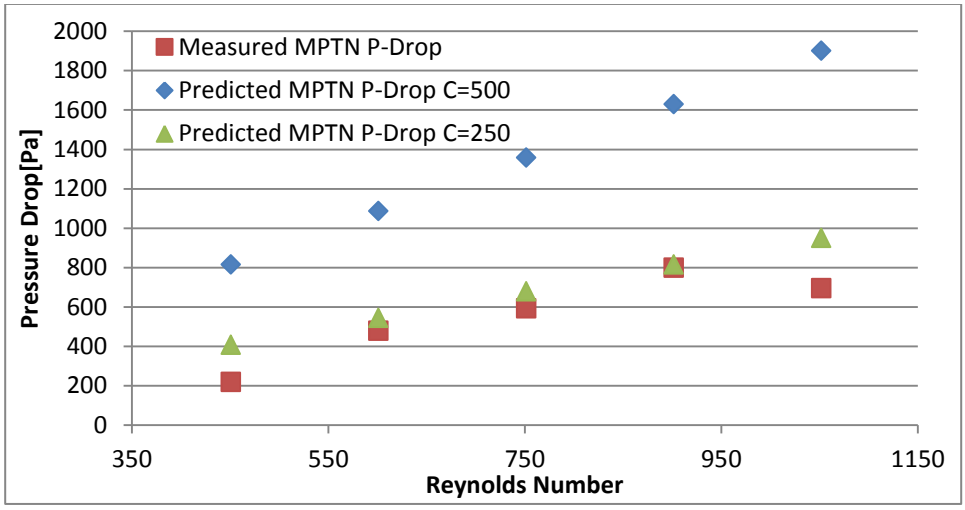

Figure 28: Pressure drop through the MPTN at various Reynolds Numbers

In preliminary testing of the weld hermiticity test articles, it was found that large and un-repairable leaks occurred at the start and end of the weld lines. This was found to be due to the ramp-up and ramp-down in the speed of the galvo mirrors leading to a difference in weld depth and weld quality for a constant power. To compensate, the laser power was ramped-up and down at the start and end of the laser weld path. The laser power was made to start at 70% of full power and ramped up to 100% over the first millimeter of weld path. The ramp down was to 70% percent starting 0.75[mm] from the end of the weld line. Round corners in the weld program will also cause the raster speed to decrease,

leading to additional variation in weld depth. To control this effect, only straight lines were used and the line lengths were longer than the side dimensions, causing the weld to start and stop outside of the shim area. The laminae stacks were tested for hermiticity after each weld by adapting the welding fixture to allow for hermeticity testing within the welding fixture. A procedure was developed using these methods to produce hermetic welds within multi-layer stacks.

For pressure drop test articles, three sets of single layer welds were performed for each weld type (flange and boss) and tested for hermiticity.

All test articles passed hermiticity testing after welding except one flange weld which required repairing. Figure 29(b) shows the device on which a successful repair weld was made. The two test articles shown in Figure 29 have MPTN integrated within the channel. Both passed pressure testing. The left weld on the test article in Figure 29(b) required a second repair weld placed inside the prior weld.

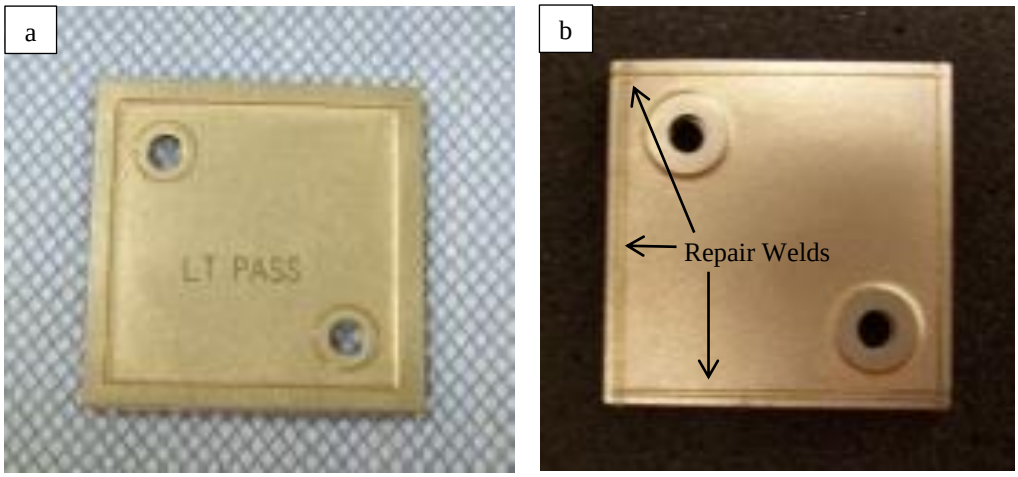

Figure 29: Examples of successful header (a) and flange (b) welds. Repair welds can be seen on the flange weld sample.

3.2 Functional Testing

3.2.1 Pressure Drop

Pressure drop measurements were taken for both fluid paths at various flow rates. Figure 30 gives pressure drop data through the HPHA compared to predictions. Pressure drop results through the HPHA match the predictive model with an average percent error of 14% which indicates good agreement. This error is best attributed to variations in geometric dimensions. Channel height estimates may not fully take into account the expected deflection of the shim during operation due to the MPTN modulus of elasticity and the measured truss heights presented above. Further, as shown in the figure, pressure drop deviations are higher at low flow rates. This is likely due to flow maldistribution across the channel which would have been worse at low flow rates as shown in Figure 31 below. At low Reynolds numbers, the fluid is most likely flowing straight across the shim and not all the surface area is being used for heat exchange. This channeling between inlet and outlet headers is more likely at lower flow rates which possess less energy for fanning out the flow between laminae.

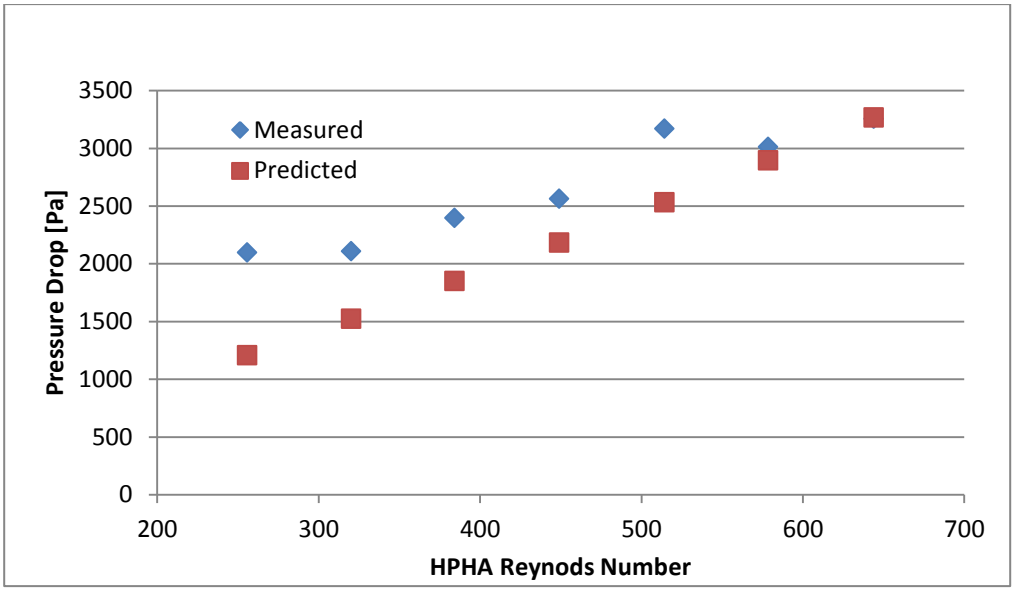

Figure 30: TDV pressure drop through the HPHA

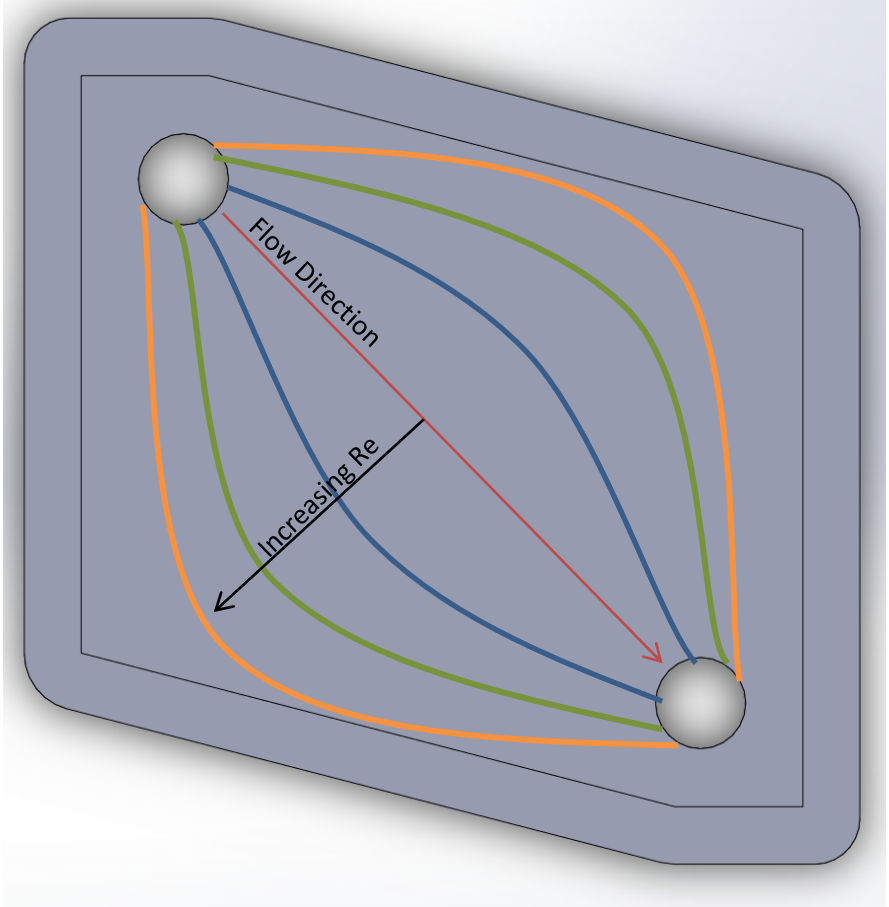

Figure 31: Sketch showing increase utilization of heat transfer surface area with increased flow rate through the shim.

Figure 32 shows the resulting pressure drop through the LPHA. The pressure drop results for the low pressure fluid were two to six times the predicted value. This demonstrates that the MPTNs are not well characterized for pressure drop. Prior studies report that the form drag is considered the largest influence on the pressure drop through a truss network [28]. It is expected that the geometric variations in the MPTN are largely the cause of this increased pressure drop which could have several sources. As was mentioned above, the periodicity of the diamond-shaped pattern did not match the periodicity of

the stamped corrugations within the MPTN. Therefore, it is possible that sections of the MPTN, where the convergence of the diamond-shaped patterns into an "X", were located between the peak and valley of the MPTN, causing significant fluid resistance. An example of a network formed like this can be seen in Figure 5(c) above. Further, the MPTN corrugations were not ideally oriented with the flow as shown in Figure 20c.

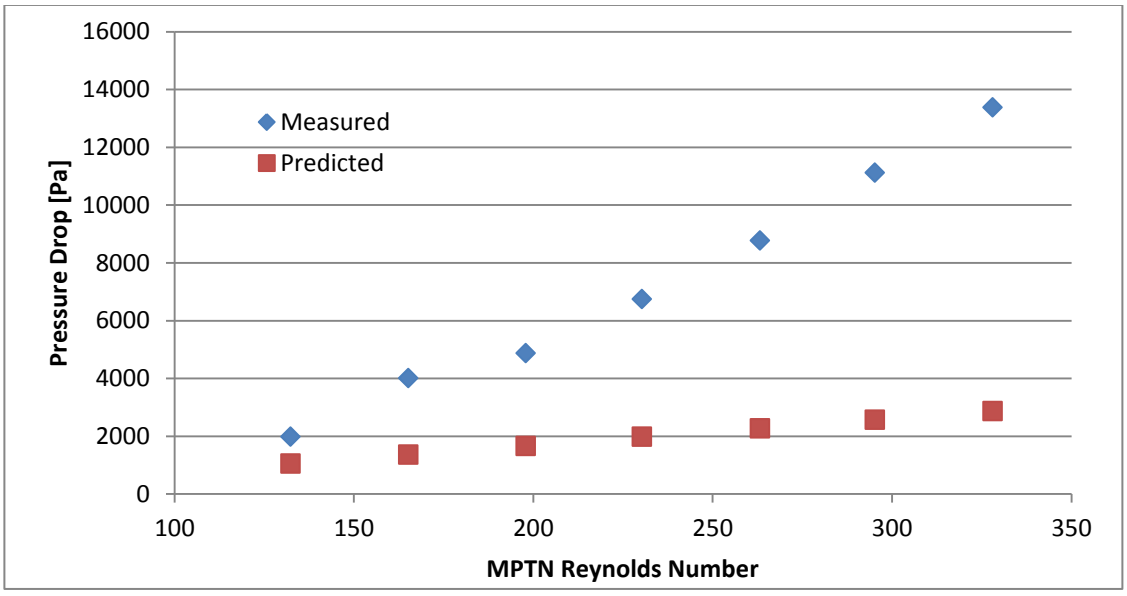

Figure 32: TDV Pressure drop through the LPHA

Another consideration is the effect of various design features. The header bosses on shim B is expected to have added significant resistance to flow as they take up a large percentage of the channel cross-sectional area. These were not accounted for in pressure drop calculations. Also, the networks reported in the literature are larger than the MPTN by a factor of almost 30. With a minimum bend radius of 0.151[mm] and a bend angle of 72°, the radius at both ends for a strut length of 0.62[mm] take up 35% of the strut length. This percentage is insignificant in the literature. The percent projected surface area underneath these bends was calculated to be less than 4%. These areas could be vulnerable to flow stagnation or vortices which could have added appreciably to pressure drop. Finally, as already discussed, the MPTN height was already 7% below the actual height. Since this was a two fluid

experiment, it is likely that the blowby that may have been experienced in the single layer experiment, was not experienced here.

Based on these observations, the flow blockage constant used in the pressure drop model was changed back to the literature value of 500 to determine the influence of the flow blockage constant. This decreased the average percent error from 68% down to 49%. Given that the maximum percent error is still 68% at the highest flow rate, results show the need for additional pressure drop characterization of the MPTN.

Other variations with the design include misalignment of laminae during welding and small burrs on the edge of the laminae (Figure 33) caused by the etching process which elongate the shim dimensions. The final HPHA used in testing had a width variation of almost 200[μm] between layers which had to be added to the pocket of the housing. This width variation creates gaps on both sides of the HPHA when inserted into the housing. As shown in Figure 33, another source of variation was a gap between the edge of the MPTN and the housing wall within the LPHA. However, if either of these two factors were significant, the pressure drop of the LPHA would have been smaller than it was.

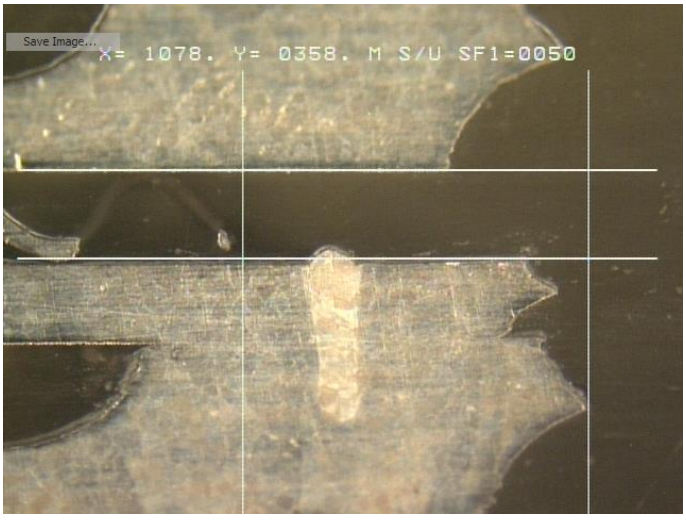

Figure 33: Micrograph of HTMR cross-section showing large (1.08[mm]) gap between the edge of the MPTN and the edge of the shim.

3.2.2 Heat Exchanger Performance

Heat exchange performance was characterized for thermal duty, MPTN Nusselt number, heat transfer coefficient, and exchanger effectiveness and compared with theoretical models as a function of Reynolds number. Results are shown in Figure 34 throughFigure 37 below.

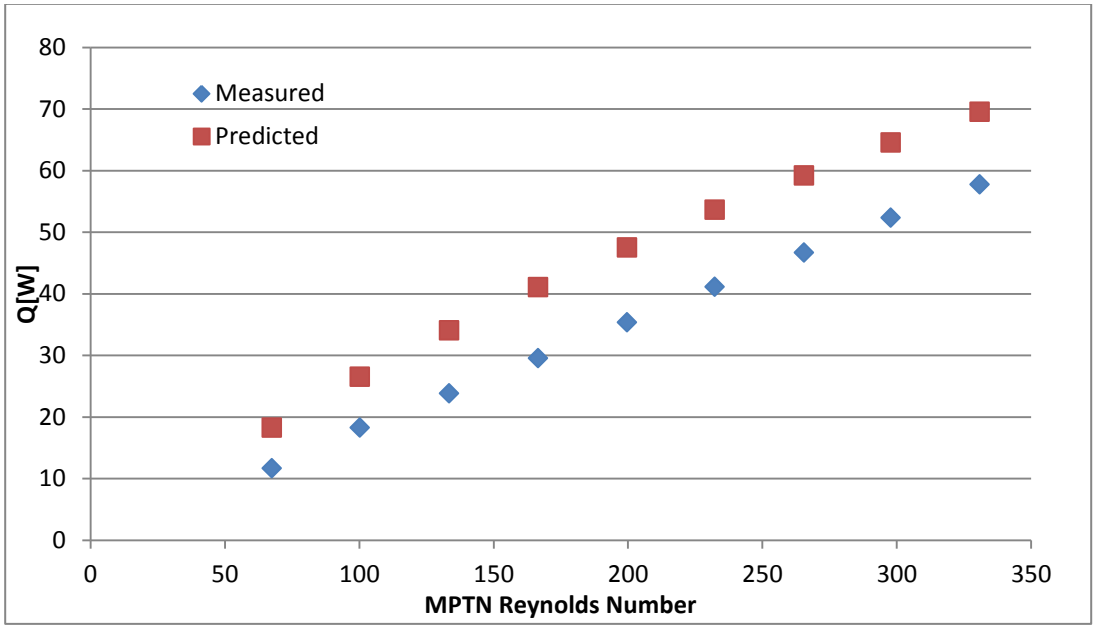

Figure 34: Experimental results for TDV thermal duty.

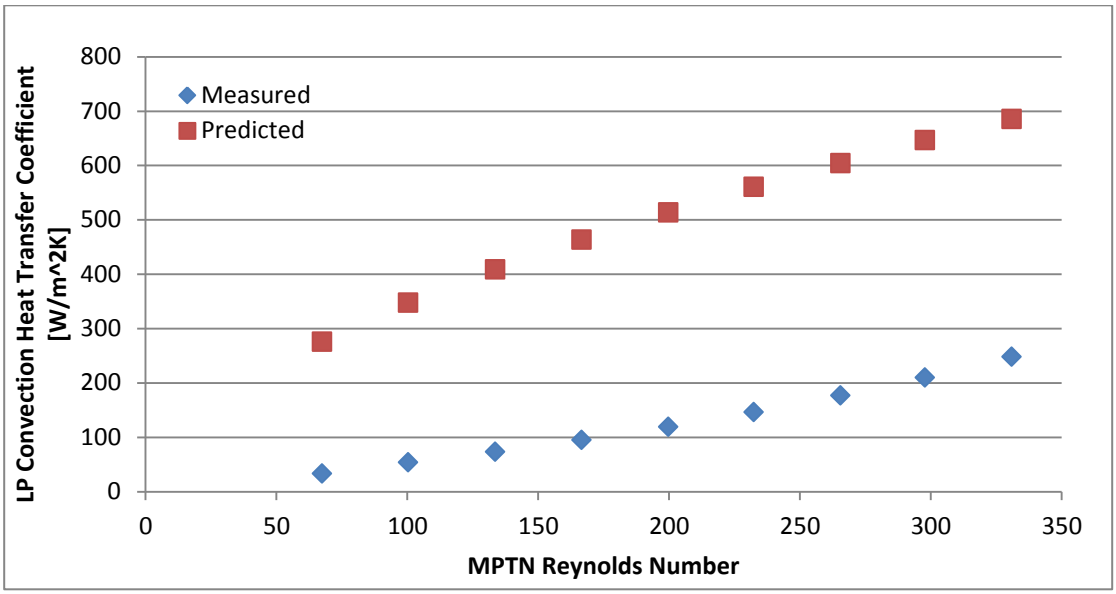

Figure 35: Experimental results for the convection heat transfer coefficient of the low pressure fluid. These results are compared to the predictive model calculated from the MPTN Nusselt number

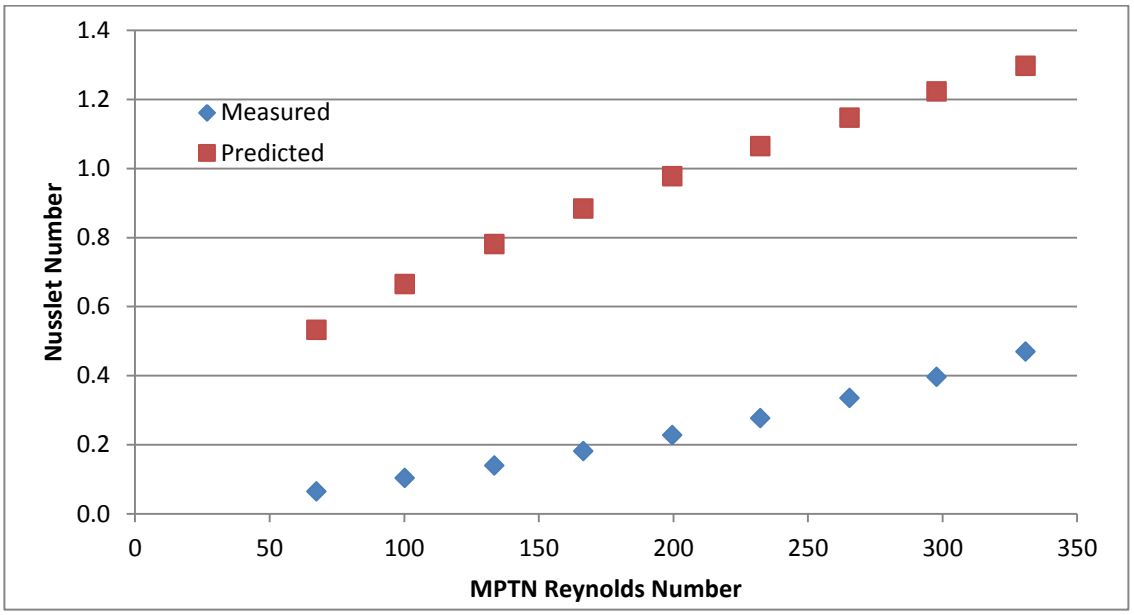

Figure 36: Nusselt number of the MPTN network within the LPHA of the TDV as a function of Reynolds Number.

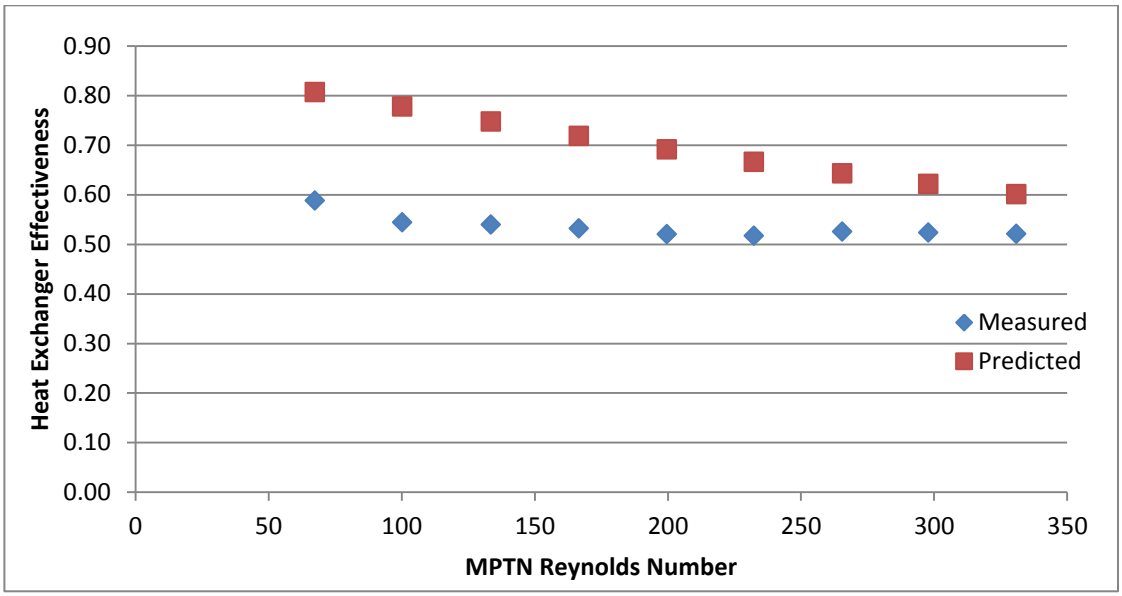

Figure 37: Experimental results for TDV effectiveness. The predicted performance includes an estimate for axial conduction.

In all cases, the TDV performed worse than predicted. The most likely cause for this lower performance is flow maldistribution particularly at the lowest flow rates as explained above. Figure 31 shows a scheme of what this flow distribution could look like within the HPHA from low to high Re number. As the flow rate increases, more of the area is utilized, and therefore the heat exchanger performance increases. This helps explain the reduction in percent error for thermal duty at higher Re. Another contributing factor to this reduction in error could be improved contact between the MPTN and the fin due to increased differential pressure. It is expected that in all cases, the surface area in all four corners is most likely not utilized. Further, as mentioned above, the MPTN that was fabricated for testing was fundamentally different than the designs used in the literature. This difference includes geometric scale differences as well as fabrication issues that can have a significant effect on the flow through the MPTN. The imperfect truss network has dead space at the MPTN-fin interface and, more importantly, creates significant flow blockage within the channel. In particular, the welding boss for the layer header in the LPHA design creates significant blockage which is accounted for as a reduction in heat transfer area in the model. The effect of flow dynamics around these features however is not

accounted for. The dead space reduces the amount of heat exchange area available for heat transfer which as discussed above is likely minor.

Some of the thermal performance issues could have been due to heat loss to the outside environment and potential fluid cross-talk (small leaks between the fluids). Heat loss was minimized through the use of large, tight wraps of insolation around the device and was also included in the calculation for effectiveness. Estimates for heat loss show a 12% impact on effectiveness at the lowest tested Reynolds number. At higher Re numbers, the effect of heat loss was estimated to be only one to three percent.

Cross-talk between the fluids could occur as a result of weld failure from the cyclical heating of the test loop, or more likely, it could occur at the high pressure fluid inlet and the low pressure fluid outlet due to the high pressure gradient experienced on the graphite gasket. If this leakage occurs, the mass flow rate used to calculate the performance of the device would be lower, as some fluid would bypass nearly the entire test loop. Before running the experiments, fluid leak tests were performed in which a single fluid channel was pressurized and sealed. A decrease in pressure occurred in the high pressure channel, but the rise in pressure in the low pressure side of the test loop was within the noise of the measurement resolution suggesting that cross-talk, likely had a minimal impact on thermal performance. To ensure that the welds had not failed, the HPHA was pressure tested after the TDV testing using the same leak test procedure used during fabrication and no leaks were found. Further, cross-talk would be expected to get worse at higher operating pressures and temperatures, which is inconsistent with the data. In an effort to try to account for the performance loss due to the cross-talk of the fluids in the effectiveness calculation, the high pressure fluid temperatures and properties were used in the numerator of the effectiveness equation.

Due to the large discrepancy in the expected thermal performance, further investigations are needed to characterize the thermal performance of the MPTN at the smaller size scale. In addition, the heat exchanger design must be modified to improve flow distribution.

3.3 Device Cost Comparison

The goal of this project was to reduce the overall cost of the HTMR relative to an original HTMR design based upon traditional photochemical machining and diffusion brazing. Table 5 shows an overall performance comparison of the scaled-up half-array HTMR design with the original scaled-up HTMR design developed using a standard microchannel lamination approach. Two cost model results are given in this section. First, the design proposed here is applied to the cost model. Secondly, a proposed half-array design that is expected to meet the project requirements for pressure drop and creep life is presented. This particular adapted design is the second design discussed in the future work section below regarding the design of the MPTN.

Table 5: Comparative chart of HTMR designs based on the various performance metrics.

Performance Metric	Targets	Conventional HTMR	Half Array HTMR
Material Selection		Haynes 214	Haynes 214
Exhaust Processing Capacity	91.6 [kg/hr]	91.6 [kg/hr]	91.6 [kg/hr]
Material Cost		$112.9/kg	$112.9/kg
Raw Material mass		69.5 [kg]	4.7[kg]
Final Device Volume		3,680 [cc]	489 [cc]
Material Utilization		55%	91%
Pressure Drop	1[psi]	<1[psi]	14[psi]
Effectiveness	90%	90%	90%
Creep Life	10[years]	10[years]	0.01[years]
Cost	$5,000	$9,266	$1,765

Two methods were employed to estimate the costs of the designs for comparison. First, a simple material-based cost was used to directly compare the cost of the half-array HTMR to that of the original HTMR. The material based cost estimate entails the summation of the total mass of the starting raw material for all parts within the HTMR, and multiplying this by the at-volume cost of Haynes 214

and Haynes 224 for the original HTMR end plates. The resulting material cost was then multiplied by 3 in order to estimate the cost of goods sold (COGS). The starting mass of the raw material for the half-array HTMR was found to be 4.7[kg] compared to a starting mass of 66.3[kg] for the original HTMR. For a raw material cost of $112.9[$/kg] for Haynes 214, the expected cost of goods sold for the half-array HTMR would be $1,340 compared to a cost of $22,179 for the original design. This suggests cost reductions of 17 times, based on improved raw material utilization and mass reduction.

The second costing method utilized to estimate the COGS was a bottom-up process-based cost model developed in Excel. This bottom up cost model was adapted by researchers at the Microproducts Breakthrough Institute and assumes the use of dedicated capital equipment for the production of the devices.[8],[9]. These cost models account for 7 cost categories; raw material, labor, tool capital equipment, equipment maintenance, utilities, capital building, and process consumables. Section 7.2 in the appendix explores the important assumptions made for these cost categories in detail. Figure 38 below shows the cost breakout by processing step for the HTMR for various production amounts as well as the percent change in cost from the previous production rate. The model applies a cost for every step in the production plan for the half-array HTMR, which is presented in appendix 7 below. The percent change values are presented in order to help identify the “knee in the curve” which represents the production volume at which a competitor could not produce the device for any cheaper by building a factory with same sized capital equipment at a higher production capacity. The “knee” can be defined as being around a production volume of 50,000 units per year where additional investment leads to a 5% or lower improvement in COGS.

The cost model results show that costs can be reduced to below the original cost target of $5,000 per device at a production rate of about 500 devices per year. These results also show that at any production volume of 1,000 or greater the largest contributing factor to cost is raw material, which is to be expected for devices utilizing high-temperature alloys. At an expected production rate of 1,000 units per year as provided by clients in the market, the estimated COGS for the half-array HTMR is $1,765 well below the original unit cost target of $5,000.

Table 6 shows the cost breakdown at this production rate. The largest contributing factor to cost is material, followed by consumables. Consumables are a large contributor due to the imprecise estimates for forming tool cost and tool life. This can be seen by the percent total of the cost due to the patterning step. The heat treatment row in this analysis is included because it is expected that future versions of the half-array HTMR will require post-process heat treating, but as this requirement was not fully investigated in this work, the process requirements were unknown and therefore not applicable to the cost model. This possible heat treatment is discussed in better detail in the future work section 5.3. Although this is the case, heat treatments are expected to be a small portion of production cost. The bottom-up analysis shows a cost reduction over the $9,266 cost of the original HTMR of five times.

The design changes to the half-array HTMR needed to meet project requirements more than double the raw material mass adding cost to this design. This mass change is mainly due to increased shim dimensions and a taller housing design that contains more material. The COGS for the modified half-array design is $2,879 for the bottom-up model. This leads to a cost reduction for the modified half-array of three times the cost of the conventionally manufactured HTMR.

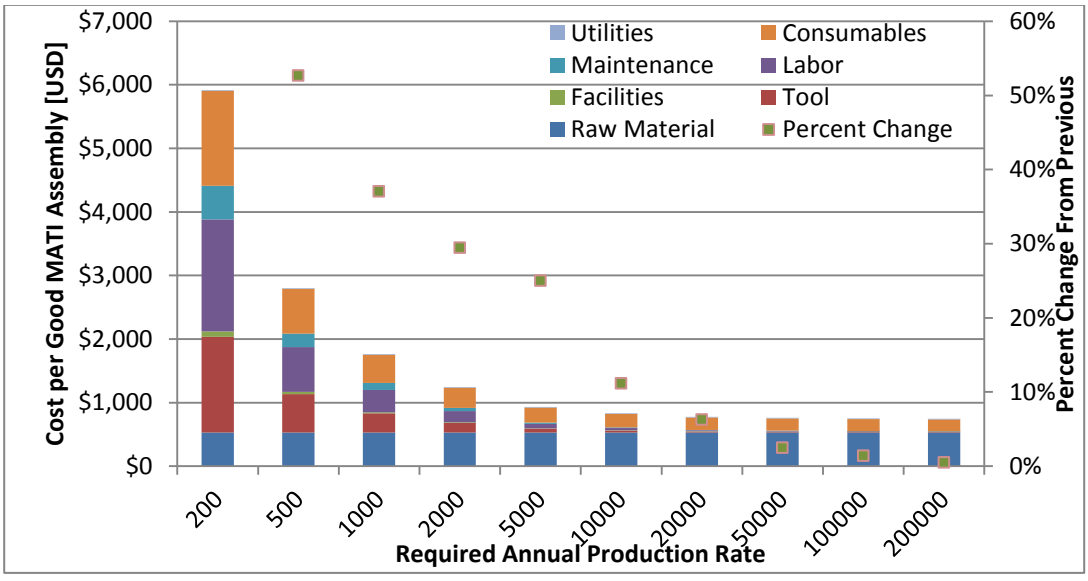

Figure 38: Cost of goods sold estimate for the half-array HTMR design at various annual production volumes. The price starts to be cost effective following 500 devices sold per year.

Table 6: Cost break down for the half-array HTMR proposed in this paper at a production rate of 1,000 units per year.

COST SUMMARIES					
Cost Summary by Category		**Percent of Total**	**Cost Summary by Process**		**Percent of Total**
Tool	**$301**	**17%**	**Patterning**	**$593**	**34%**
Facilities	**$17**	**1%**	**Bonding**	**$511**	**29%**
Labor	**$352**	**20%**	**Assembly**	**$39**	**2%**
Maintenance	**$106**	**6%**	**Inspection**	**$1**	**0%**
Material	**$532**	**30%**	**Heat Treatment**	**N/A**	**-**
Consumables	**$447**	**25%**	**Raw Material**	**$532**	**30%**
Utilities	**$10**	**1%**	**Header**	**$89**	**5%**
Total Per Device[USD]	**$1,765**		**Total**	**$1,765**	

4 Conclusions

This work has demonstrated a new means for producing a high temperature microchannel recuperator (HTMR) based on the production and packaging of a microchannel half-array that greatly improves the raw material utilization and improves production yields. The design of the device through the use of a microchannel flow insert accommodates stamping of the laminae which provides for improved material utilization and lower production costs over photochemical machining. Laser welding of the half array requires less bond area and the promise of higher bonding yields. Process-based cost estimates suggest that the new manufacturing architecture could reduce costs by over 70% over devices made using traditional photochemical machining and diffusion brazing methods. Testing of the half-array design shows additional pressure drop and thermal performance characterization is needed of the micro-scale pyramidal truss network developed in this thesis.

While this microchannel lamination architecture was developed for an HTMR, it has potential application to a broad host of microchannel components and applications. The unique design of the device lends itself well to any two-fluid device designs. The use of a housing to package half of the microchannel array lends itself well to disassembly of the array for microchannel de-fouling or catalyst regeneration.

5 Future Work

The main objective of this research was to demonstrate new microchannel lamination methods for producing a high-termperature microchannel recuperator that allows for reduced costs. While a manufacturing approach was demonstrated with the potential to meet this objective, various design changes and a more thorough flow, pressure drop and thermal characterization of the device are needed in order for the design to be used for any commercial applications. There are four main areas where changes and investigations are required as follows:

- MPTN geometric changes and performance characterization to meet design criteria
- Flow path optimization for flow distribution
- Laser-material interaction
- Shim and housing geometric tolerances due to forming

5.1 MPTN Geometric Changes

As discussed previously, the original micro-scale pyramidal truss network developed for the high temp recuperator was found to not meet the design criteria for creep life, pressure drop and thermal performance. Performing a basic analysis of pressure drop and using the same creep failure criteria as described above, a modified MPTN has been proposed. An isometric view of this design can be seen in Figure 39.

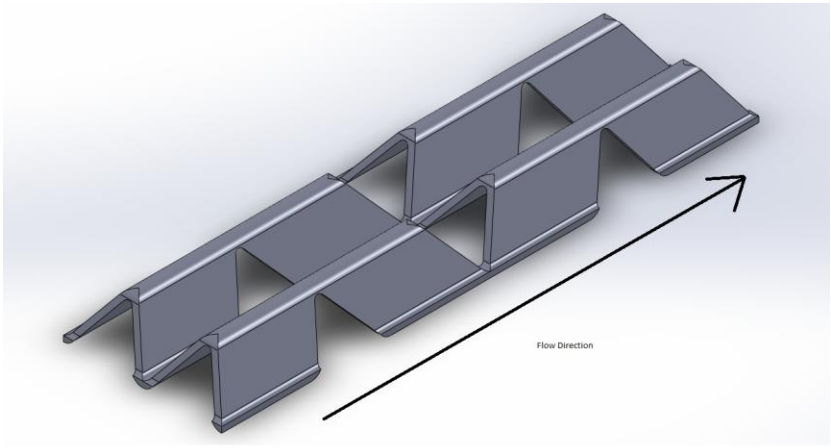

Figure 39: Small section of the modified MPTN that, in conjunction with flow length changes, meets the HTR design goals

This possible redesign of the MPTN is manufactured in the same manner as an ideal truss network; however a change in the raw material design is required to offset the diamond perforations to allow thicker struts. In order to meet the pressure drop requirement of one [psi] two changes were required. First, the inlet flow velocity was reduced by increasing the channel cross-sectional area. This was achieved by both increasing the width of the channel from 84[mm] to 120[mm] as well as changing the channel height from 450[μm] to 650[μm]. Secondly, the flow length was reduced to 85[mm]. Using first pass estimates for performance, the modified design is expected to provide a pressure drop of 0.83[psi] and a buckling stress of 1.14 [MPa] at operating temperature providing an estimated creep life of 27 years (using a safety factor of two).

All the predictive modeling surrounding small-scale truss networks of various designs have been done around an ideal network with a pitch dimension that is identical in both x and y directions. Due to the proposed modifications to the MPTN, these predictive models will not provide accurate values with which to develop device designs. For this reason, further investigation into the flow and heat transfer performance of MPTN devices will need to be investigated. These models will help designers understand early on in the design stage whether the MPTN or other microchannel flow inserts (MFIs) will be capable of meeting the requirements of a specific MPT application.

The bottom-up cost model discussed in section 3.3 was adopted to a scaled up MPTN design and provided a per unit cost of $2,237 at 1000 units produced per year. This still meets the price target for this project showing that a low cost half-array HTMR is possible even with modifications to meet design specs. Even though this design is an ideal network, the reduced size scale compared to literature networks will still introduce changes in the performance characteristics that will need to be investigated to improve the design tools for future half-array applications.

To remain an ideal pyramidal truss network and meet pressure drop and creep life calculations, an ideal MPTN would need to have a height of around 2.4[mm] and a pitch of 2.3[mm]. This network would be made from an expanded foil with a starting thickness of 400[μm] in order to maintain the required creep life. It is not known whether these dimensions would not permit the compact form factor and weight reduction associated with microchannel heat exchangers.

5.2 Flow Path Optimization

As seen above in Figure 1(b), representative embossed features are shown inside the HPHA that are used to evenly distribute flow across the lamina. These features were found to be inadequate for flow distribution. The placement, size, and shape of layer and channel headers must be determined to ensure proper flow distribution. In order to bring the HTMR into the next stage of development, computational fluid dynamic simulations will be needed to help improve flow distribution which is important to ensuring proper device function.

5.3 Laser-Material Interaction

The initial process of weld parameter optimization for Haynes 214 only found welding parameters that provided a strong hermetic seal. There are a few effects of the high heat input into the material that need to be explored such as loss of alloying elements due to vaporization, diffusion of

alloying elements to or away from the weld line, and changes in material microstructure as a result of the welding process. Lajavardi.[15] found the shear strength of laser lap welds performed with Haynes 214 approached the bulk yield strength leading to a hypothesis that there is not a significant loss in strength due to the addition of the weldment. It is expected however that chemical compositional changes will have a larger effect on high temperature performance for both creep and corrosion. It will be important to perform a more detail examination of the material microstructure before and after welding, examining both the grain size and compositional effects in order to discover whether an additional heat treatment is required. A post weld heat treatment may be needed to return the material back to its annealed properties, which for Haynes 214, is a solution hardened state with little or no precipitates.

One option worth exploring would be the adaptation of the laser welding system to perform a localized heat treatment with a defocused beam and slow raster speeds. A benefit of this experimentation would be reduced heat treatment cycle times as the annealing temperature for Haynes 214 is 1094 [°C] with only enough hold time to bring all the material to temperature. Without having to heat the entire part this cycle time will be further reduced.

5.4 Forming Tolerances

Due to budget constraints, the forming characteristics of the flow shims and of the proposed deep drawn housing were not investigated. As a result, it cannot be said concretely that the designed heights and dimensions of the shims and housing can be met with reliable accuracy and repeatability. Metal embossing experiments are needed to investigate the dimensional tolerances achievable in these forming processes, and how these tolerances can be improved through the use of new process technologies such as electrically-assisted forming.

6 References

[1] A. B. Stambouli and E. Traversa, “Solid oxide fuel cells (SOFCs): a review of an environmentally clean and efficient source of energy,” *Renewable and Sustainable Energy Reviews*, vol. 6, no. 5, pp. 433–455, Oct. 2002.

[2] I. and I. P. G. International Conference on Gas Turbines in Cogeneration and Utility, H. W. Holland, and ASME International Gas Turbine Institute, “Introduction of a Fuel Cell Into a Combined Cycle: A Competitive Choice for Future Cogeneration,” New York, 1993.

[3] B. K. Paul, *Micro Energy and Chemical Systems and Multi-scale Fabrication*. Germany: Springer-Verlag, 2005.

[4] H. Cao, G. Chen, and Q. Yuan, “Testing and Design of a Microchannel Heat Exchanger with Multiple Plates,” *Industrial & Engineering Chemistry Research*, vol. 48, no. 9, pp. 4535–4541, May 2009.

[5] P. M. Martin, D. W. Matson, and W. D. Bennett, “Microfabrication Methods For Microchannel Reactors And Separations Systems,” *Chemical Engineering Communications*, vol. 173, no. 1, pp. 245–254, Jun. 1999.

[6] K. Yoshida, S. Tanaka, H. Hiraki, and M. Esashi, “A micro fuel reformer integrated with a combustor and a microchannel evaporator,” *Journal of Micromechanics and Microengineering*, vol. 16, no. 9, pp. S191–S197, Sep. 2006.

[7] W. A. Little, “Microminiature refrigerators for Joule-Thomson cooling of electronic chips and devices,” in *Advances in cryogenic engineering*, lost angeles, CA, 1989, pp. 1325–1333.

[8] S. D. Leith, D. . King, and B. K. Paul, “Toward Low-Cost Fabrication of Microchannel Process Technologies- Cost Modeling for Manufacturing Development,” in *Innovations of Green Process Engineering for Sustainable Energy and Environment*, Salt Lace City, UT, 2010.

[9] B. Lajevardi, S. D. Leith, D. . King, and B. K. Paul, “Arrayed Microchannel Manufacturing Costs for an Auxiliary Power Unit Heat Exchanger,” in *Proceedings of the 2011 Industrial Engineering Research Conference*, Reno, NV, 2011.

[10] P. Paulraj and B. K. Paul, “Metal microchannel lamination using surface mount adhesives for low-temperature heat exchangers,” *Journal of Manufacturing Processes*, vol. 13, no. 2, pp. 85–95, Aug. 2011.

[11] P. Paulraj, B. K. Paul, and R. B. Peterson, “Development of an adhesive-bonded counterflow microchannel heat exchanger,” *Applied Thermal Engineering*, vol. 48, pp. 194–201, Dec. 2012.

[12] B. K. Paul and G. K. Lingam, “Cooling rate limitations in the diffusion bonding of microchannel arrays,” presented at the 39th Annual North American Manufacturing Research Conference, NAMRC39, 2011, vol. 39, pp. 500–508.

[13] B. K. Paul and G. K. Lingam, “Cooling rate limitations in the diffusion bonding of microchannel arrays,” *Journal of Manufacturing Processes*, vol. 14, no. 2, pp. 119–125, Apr. 2012.

[14] B. K. Paul, S. Bose, and D. Palo, “An internal convective heating technique for diffusion bonding arrayed microchannel architectures,” *Precision Engineering*, vol. 34, no. 3, pp. 554–562, Jul. 2010.

[15] B. Lajevardi, “Laser keyhole welding for microlaminating a high-temperature microchannel array,” Oregon State University, Corvallis Oregon, 2012.

[16] S. Kalpakjian and S. R. Schmid, *Manufacturing processes for engineering materials*. Upper Saddle River, N.J.: Prentice Hall, 2003.

[17] M. P. Groover, “Fundamentals of modern manufacturing materials, processes, and systems,” 2007. [Online]. Available: http://www.books24x7.com/marc.asp?bookid=26029. [Accessed: 14-Jun-2012].

[18] R. J. Roark, R. G. Budynas, and W. C. Young, *Roark's formulas for stress and strain*. New York: McGraw-Hill, 2002.

[19] S. W. Churchill, "Friction-Factor Equation Spans All Fluid Flow Eegimes," *Chemical Engineering*, vol. 84, no. 24, pp. 91–92, 1977.

[20] C. F. Colebrook, "Turbulent Flow In Pipes, With Particular Reference To The Transition Region Between The Smooth And Rough Pipe Laws," *Journal of the ICE*, vol. 11, no. 4, pp. 133–156, Feb. 1939.

[21] B. R. Munson, T. H. Okiishi, W. W. Huebsch, and A. P. Rothmayer, *Fundamentals of fluid mechanics*. Hoboken, NJ: John Wiley & Sons, Inc., 2013.

[22] J. R. Welty, *Fundamentals of momentum, heat, and mass transfer*. New York: Wiley, 2001.

[23] D. T. Queheillalt and H. N. G. Wadley, "Pyramidal lattice truss structures with hollow trusses," *Materials Science and Engineering: A*, vol. 397, no. 1–2, pp. 132–137, Apr. 2005.

[24] V. . Deshpande and N. . Fleck, "Collapse of truss core sandwich beams in 3-point bending," *International Journal of Solids and Structures*, vol. 38, no. 36–37, pp. 6275–6305, Sep. 2001.

[25] R. Biagi and H. Bart-Smith, "Imperfection sensitivity of pyramidal core sandwich structures," *International Journal of Solids and Structures*, vol. 44, no. 14–15, pp. 4690–4706, Jul. 2007.

[26] H. Wadley, "Fabrication and structural performance of periodic cellular metal sandwich structures," *Composites Science and Technology*, vol. 63, no. 16, pp. 2331–2343, Dec. 2003.

[27] M. F. Ashby, "Materials selection in mechanical design," 2005. [Online]. Available: http://www.knovel.com/knovel2/Toc.jsp?BookID=1472. [Accessed: 19-Nov-2012].

[28] T. Kim, H. . Hodson, and T. . Lu, "Fluid-flow and endwall heat-transfer characteristics of an ultralight lattice-frame material," *International Journal of Heat and Mass Transfer*, vol. 47, no. 6–7, pp. 1129–1140, Mar. 2004.

[29] T. Kim, C. Y. Zhao, T. J. Lu, and H. P. Hodson, “Convective heat dissipation with lattice-frame materials,” *Mechanics of Materials*, vol. 36, no. 8, pp. 767–780, Aug. 2004.

[30] T. Kim, P. Hodson, and T. J. Lu, “Pressure loss and heat transfer mechanisms in a lattice-frame structured heat exchanger,” *Proceedings of the Institution of Mechanical Engineers*, vol. 218, no. 11, p. 1321, Nov. 2004.

[31] E. Sadeghi, M. Bahrami, and N. Djilali, “Estimation of Nusselt Number in Microchannels of Arbitrary Cross Section with Constant Axial Heat Flux,” *Heat Transfer Engineering*, vol. 31, no. 8, pp. 666–674, Jul. 2010.

[32] T. . Kals and R. Eckstein, “Miniaturization in sheet metal working,” *Journal of Materials Processing Technology*, vol. 103, no. 1, pp. 95–101, Jun. 2000.

APPENDICIES

7.1 Half Array HTMR Manufacturing Plan

The manufacturing plan for the HTMR is presented here. It consists of all the major steps that could be involved in the final manufacturing process for a commercial version of the HTMR. This process flow is the basis for the bottom-up cost model in development for the HTMR

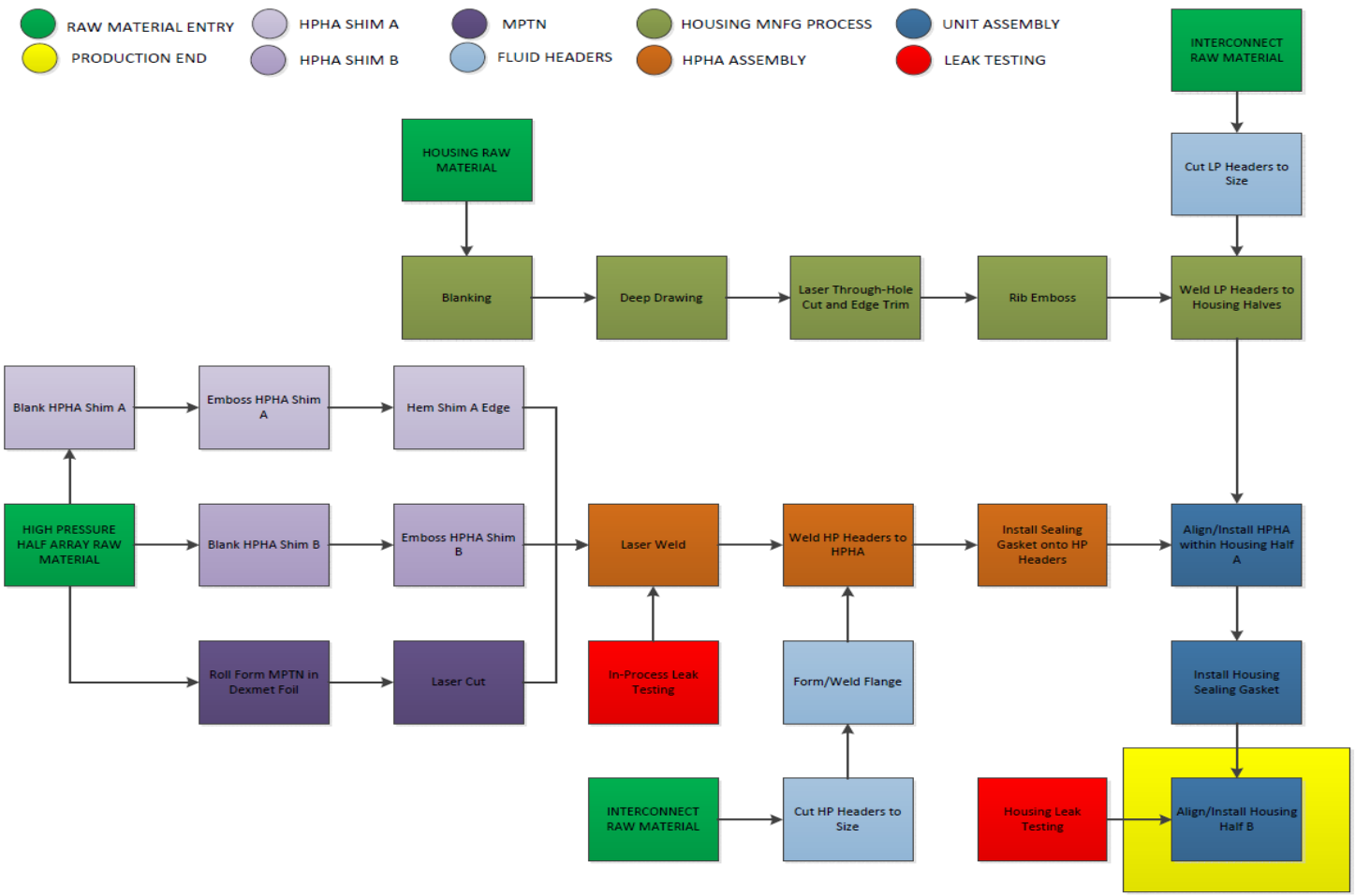
RAW MATERIAL ENTRY
PRODUCTION END
HPHA SHIM A
HPHA SHIM B
MPTN
FLUID HEADERS
HOUSING MNFG PROCESS
HPHA ASSEMBLY
UNIT ASSEMBLY
LEAK TESTING
INTERCONNECT RAW MATERIAL
HOUSING RAW MATERIAL
Cut LP Headers to Size
Blanking
Deep Drawing
Laser Through-Hole Cut and Edge Trim
Rib Emboss
Weld LP Headers to Housing Halves
Blank HPHA Shim A
Emboss HPHA Shim A
Hem Shim A Edge
HIGH PRESSURE HALF ARRAY RAW MATERIAL
Blank HPHA Shim B
Emboss HPHA Shim B
Laser Weld
Weld HP Headers to HPHA
Install Sealing Gasket onto HP Headers
Align/Install HPHA within Housing Half A
Roll Form MPTN in Dexmet Foil
Laser Cut
In-Process Leak Testing
Form/Weld Flange
Install Housing Sealing Gasket
INTERCONNECT RAW MATERIAL
Cut HP Headers to Size
Housing Leak Testing
Align/Install Housing Half B

7.2 Description of Cost Model Assumptions

The bottom-up cost model developed for the half-array HTMR makes assumptions in the 7 cost categories in order to achieve an estimate for COGS. In order to validate these assumptions, process development and analysis is required that extends far outside the scope of any one research project and is an objective of work performed by the Microproducts Breakthrough Institute. This section gives a brief description of key assumptions for each cost category. The most important assumption made for this cost model is that it entails the production of an entire facility, also known as a green field plant. This assumptions leads to results that are more accurate at high production volumes, when costs start to be more consist ant and tool/labor utilization is high.

One key difference in the half-array model verses previous versions is the inclusion of tool sharing. In this model, under-utilized tools are shared between processes in order to reduce capital costs at lower production rates. Because the half-array HTMR is mainly formed, five or six processes can share the same capital equipment and therefore only require a tooling changeover. Previous models assumed a dedicated piece of capital equipment for each individual process step. Because four of the seven cost categories are driven by the number of production tools, this change propagates a cost savings over all four of these categories. These categories are capital tool depreciation, capital tool maintenance, facility costs, and labor costs.

7.2.1 Capital Tool Depreciation

Capital equipment is often a large cost contributor at low production volumes. This is mainly due to the scale of the machines and the overall tool utilization. To justify the building of a dedicated manufacturing line, equipment must be sized to have capacities that facilitate short production times at high production volumes. If the factory is only required to build one tenth the designed capacity of the tooling, the cost of the expensive tooling is shared over only a few devices, leading to large costs. Some

key assumptions for this category are process yields and tool depreciation years. Process yields are found based on either costumer quotes or standard yield rates for similar production processes. The latter is more often the case for processes that are being proposed or have not been fully characterized, like laser welding. In these instances, yields are left conservative. For the model presented here, the laser welding yield is assumed 95%, even though the use of in-process quality control should provide more useful welded parts. The cost of the tooling is expected to be deprecated over 7 years, so this is factored into the capital cost.

An installation cost is also added to the tooling depreciation. This is based on an estimated installation cost of 6% the capital equipment cost.

7.2.2 Facility Depreciation

A few assumptions are made in this cost category. First, a building cost depreciation life is assumed to be 25 years. Secondly, cost per square meter of floor space is estimated based on industry standards. Depending on the different types of tooling environmental requirements, this cost varies. As an example a process requiring a clean room environment will have a $5,000 per square meter cost versus a tool only requiring assembly space having a cost of $1,000 per square meter. The half-array HTMR production line only requires manufacturing floor space. Two additional assumptions are made about tool space requirements. An estimate of the required tool floor space is made based on tool footprint. In addition to this a multiplier of 2 is added to this estimate in order to account for any support equipment, piping/utilities, and workspace required for the tool.

7.2.3 Labor

There are three key assumptions made in this cost category. First, the cost of labor for one full time employee (FTE) is estimated to be $50,000 per year. Secondly, a multiplier is added to account for overhead like accounting, management, and employment benefits. For this cost model this multiplier is

estimated to be 1.5. The third assumption is the required amount of labor needed to handle each process step. For this cost model the majority of the processes will be semi-automated so an assumption of a 0.25FTE labor requirement is made for each tool. Improvements in production planning further down the commercialization process could improve labor efficiency and automation, which will reduce labor costs. This is beneficial as at the low production requirement for this device labor is highly under-utilized leading to idle hands.

7.2.4 Maintenance

One assumption is made in this cost category and that is the annual maintenance cost for each piece of capital equipment. This cost is based on a percentage of the capital cost for each process tool, and is estimated to be 3%.

7.2.5 Raw Material

The only assumption made in this cost category is the estimate for the bulk cost of sheet stock and bar stock for the material required. For Haynes 214, the cost estimate per kilogram is based on interactions with the supplier giving confidence to this value. Because this bulk cost of material is less expensive at very large order sizes, the cost for raw material is an underestimate at lower production volumes, when it is unlikely that a material order will be placed regularly and of high enough mass to enable large discounts.

7.2.6 Process Consumables

Without going into detail, the main assumptions made in this cost category revolve around consumable cost and useful life. Punch and die tooling for the forming processes in this cost model have an estimated tooling cost of $10,000 per die-set and varying useful lives depending on the scale of the required cycles or expected forces. These estimates can greatly influence the cost of stamped materials and need to be refined to improve model accuracy. One of the largest contributors to the half-

array cost is the cost of the laser welding diodes and lenses. This cost is attributed to a poor assumption made about the part life. It is assumed that the diode will be replaced every week regardless of production rate. Assumptions like this lead to large costs at lower production volumes.

7.2.7 Process Utilities

The cost of utilities is estimated for each process step. These costs are estimated based on the capital equipment utility requirements or the calculated requirements to perform a specific step. For example, the required power needed to cut a header tube to length can be explicitly calculated taking into account motor efficiencies and material properties. The costs for the supply of the utilities are based on industrial rates found for that utility.

7.3 Half Array HTR Engineering Packet

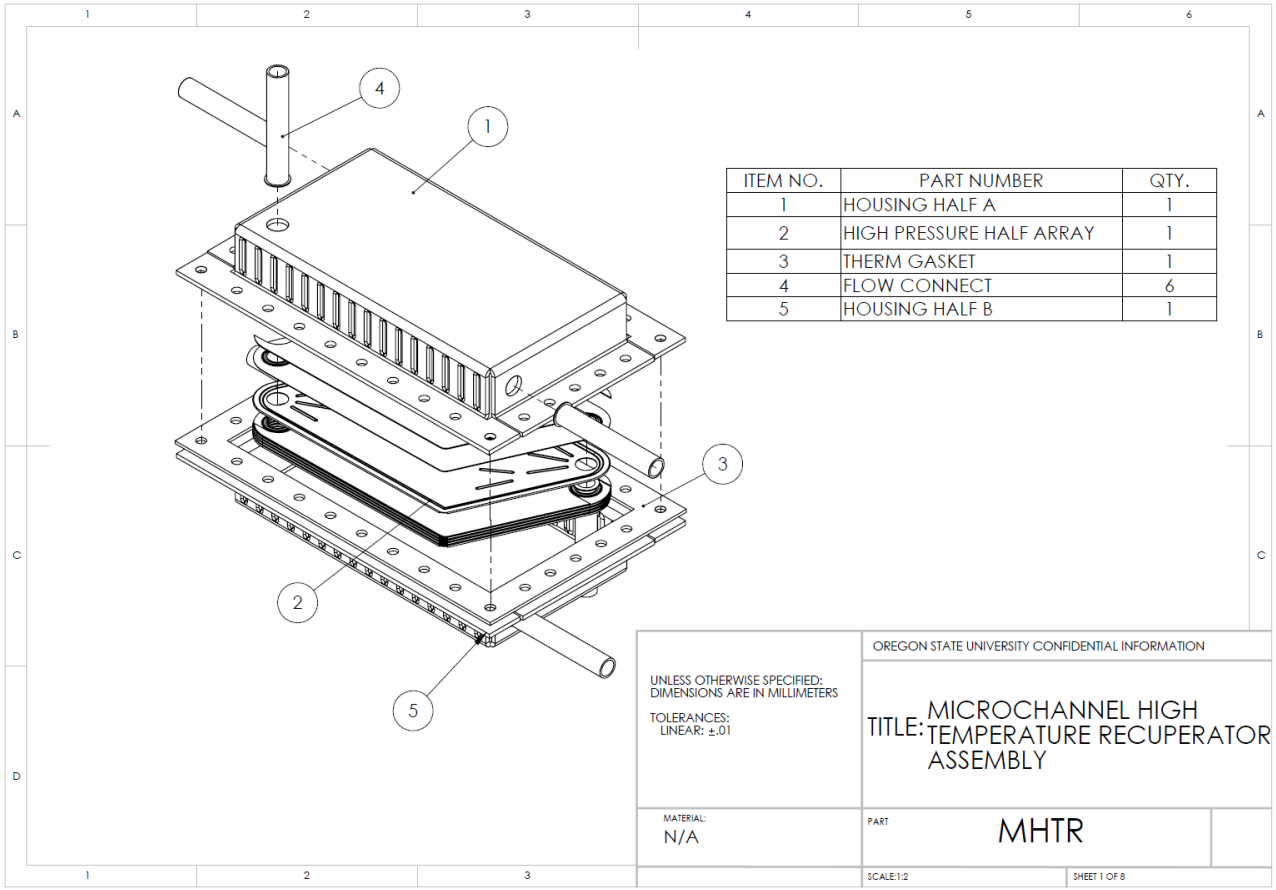

ITEM NO.	PART NUMBER	QTY.
1	HOUSING HALF A	1
2	HIGH PRESSURE HALF ARRAY	1
3	THERM GASKET	1
4	FLOW CONNECT	6
5	HOUSING HALF B	1

UNLESS OTHERWISE SPECIFIED:
DIMENSIONS ARE IN MILLIMETERS

TOLERANCES:
LINEAR: ±.01

OREGON STATE UNIVERSITY CONFIDENTIAL INFORMATION

TITLE: MICROCHANNEL HIGH TEMPERATURE RECUPERATOR ASSEMBLY

MATERIAL: N/A

PART: MHTR

SCALE:1:2

SHEET 1 OF 8

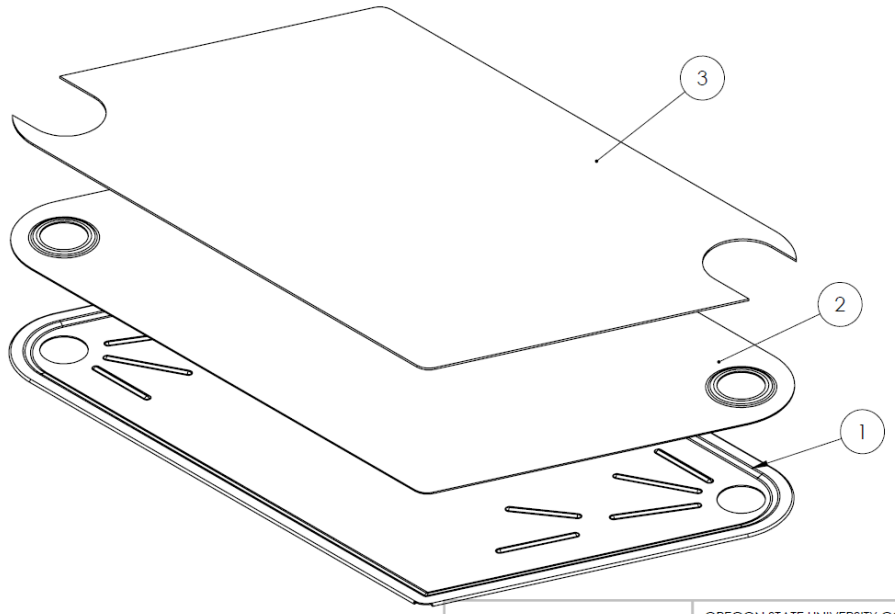

ITEM NO.	PART NUMBER	QTY.
1	CFC FLOW SHIM	1
2	CFC COVER	1
3	MPTN REPRESENTATION	1

UNLESS OTHERWISE SPECIFIED:
DIMENSIONS ARE IN MILLIMETERS

TOLERANCES:
LINEAR: ±.01

OREGON STATE UNIVERSITY CONFIDENTIAL INFORMATION

TITLE: HIGH PRESSURE HALF ARRAY ASSEMBLY

MATERIAL:
HAYNES 214

PART
HIGH PRESSURE HALF ARRAY

SCALE:1:1

SHEET 2 OF 8

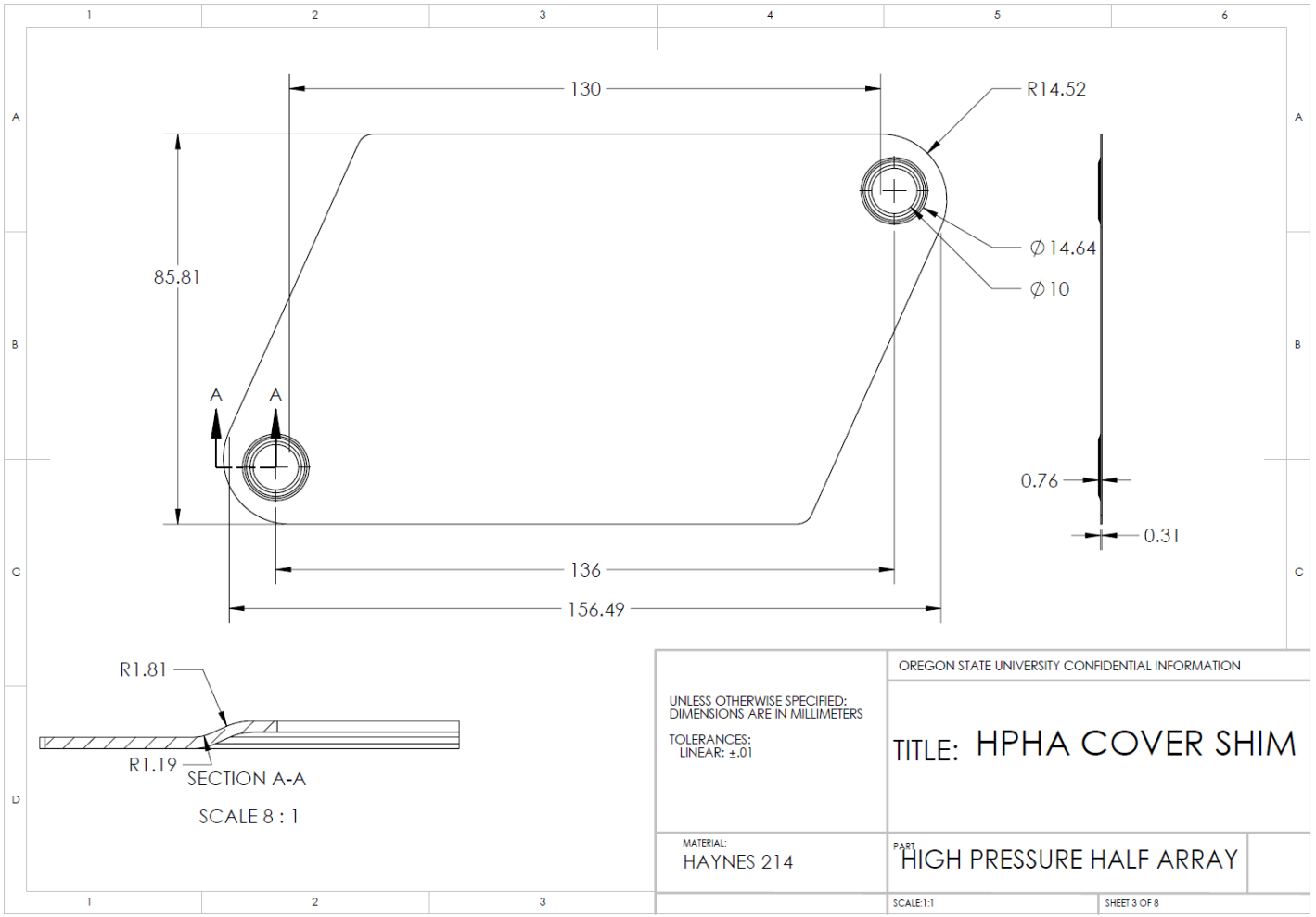
130
R14.52
85.81
∅14.64
∅10
A
A
0.76
0.31
136
156.49
R1.81
R1.19
SECTION A-A
SCALE 8 : 1
UNLESS OTHERWISE SPECIFIED:
DIMENSIONS ARE IN MILLIMETERS
TOLERANCES:
LINEAR: ±.01
OREGON STATE UNIVERSITY CONFIDENTIAL INFORMATION
TITLE: HPHA COVER SHIM
MATERIAL:
HAYNES 214
PART
HIGH PRESSURE HALF ARRAY
SCALE:1:1
SHEET 3 OF 8

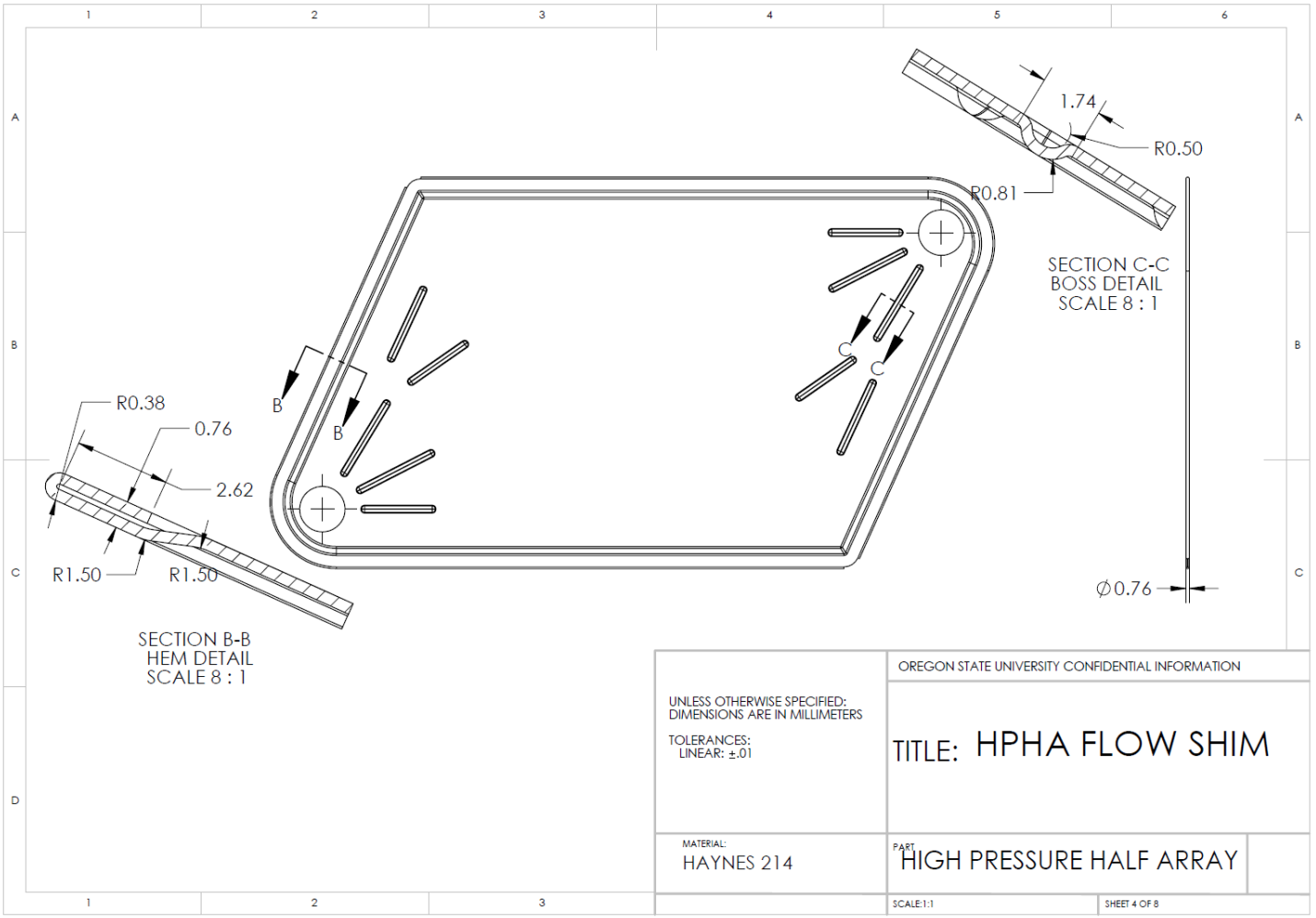
1.74
R0.50
R0.81
SECTION C-C
BOSS DETAIL
SCALE 8 : 1
B
B
C
C
R0.38
0.76
2.62
R1.50
R1.50
SECTION B-B
HEM DETAIL
SCALE 8 : 1
∅0.76
OREGON STATE UNIVERSITY CONFIDENTIAL INFORMATION
UNLESS OTHERWISE SPECIFIED:
DIMENSIONS ARE IN MILLIMETERS
TOLERANCES:
LINEAR: ±.01
TITLE: HPHA FLOW SHIM
MATERIAL:
HAYNES 214
PART
HIGH PRESSURE HALF ARRAY
SCALE:1:1
SHEET 4 OF 8

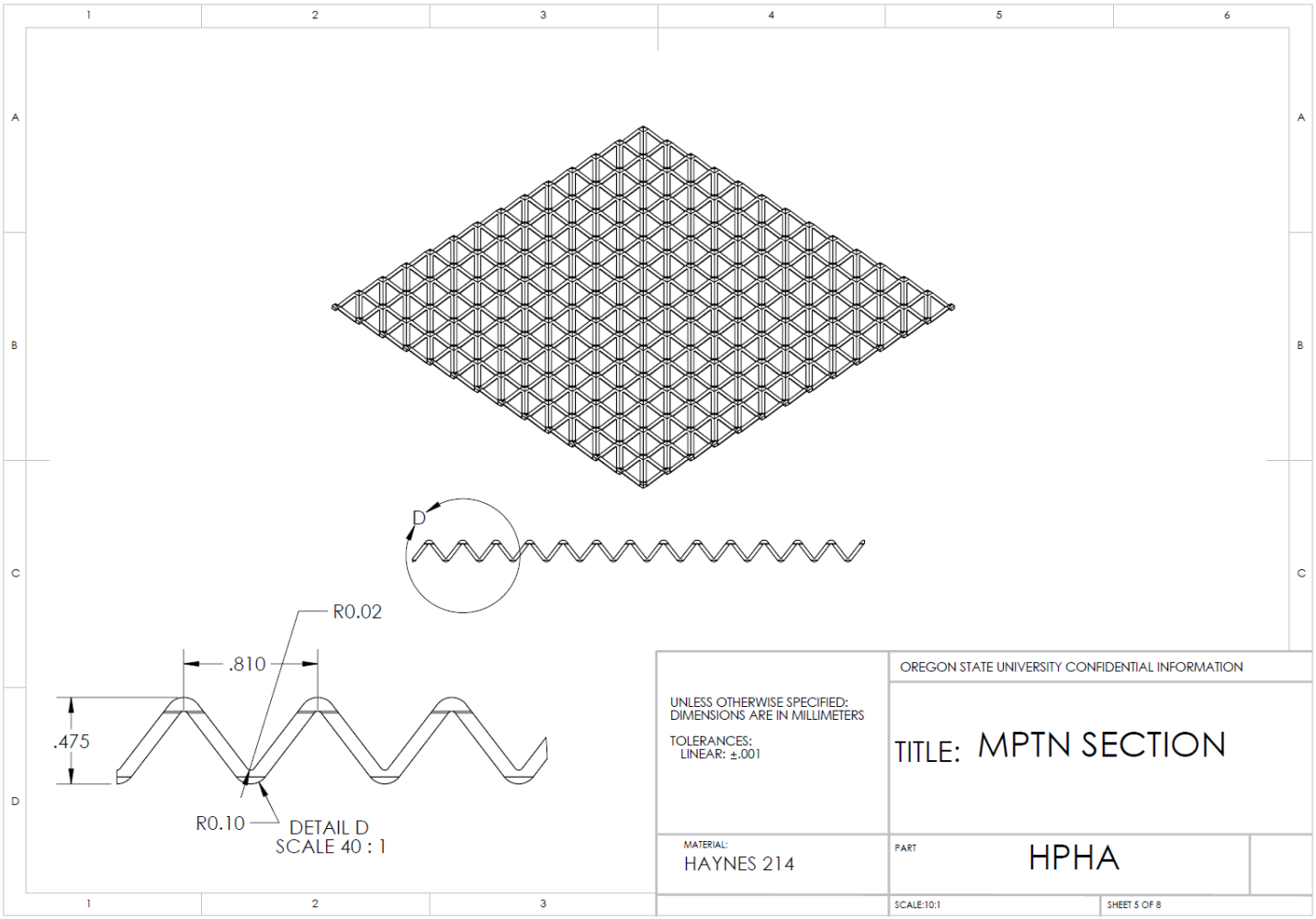
D
R0.02
.810
.475
R0.10
DETAIL D
SCALE 40 : 1
OREGON STATE UNIVERSITY CONFIDENTIAL INFORMATION
UNLESS OTHERWISE SPECIFIED:
DIMENSIONS ARE IN MILLIMETERS
TOLERANCES:
LINEAR: ±.001
TITLE: MPTN SECTION
MATERIAL:
HAYNES 214
PART
HPHA
SCALE:10:1
SHEET 5 OF 8

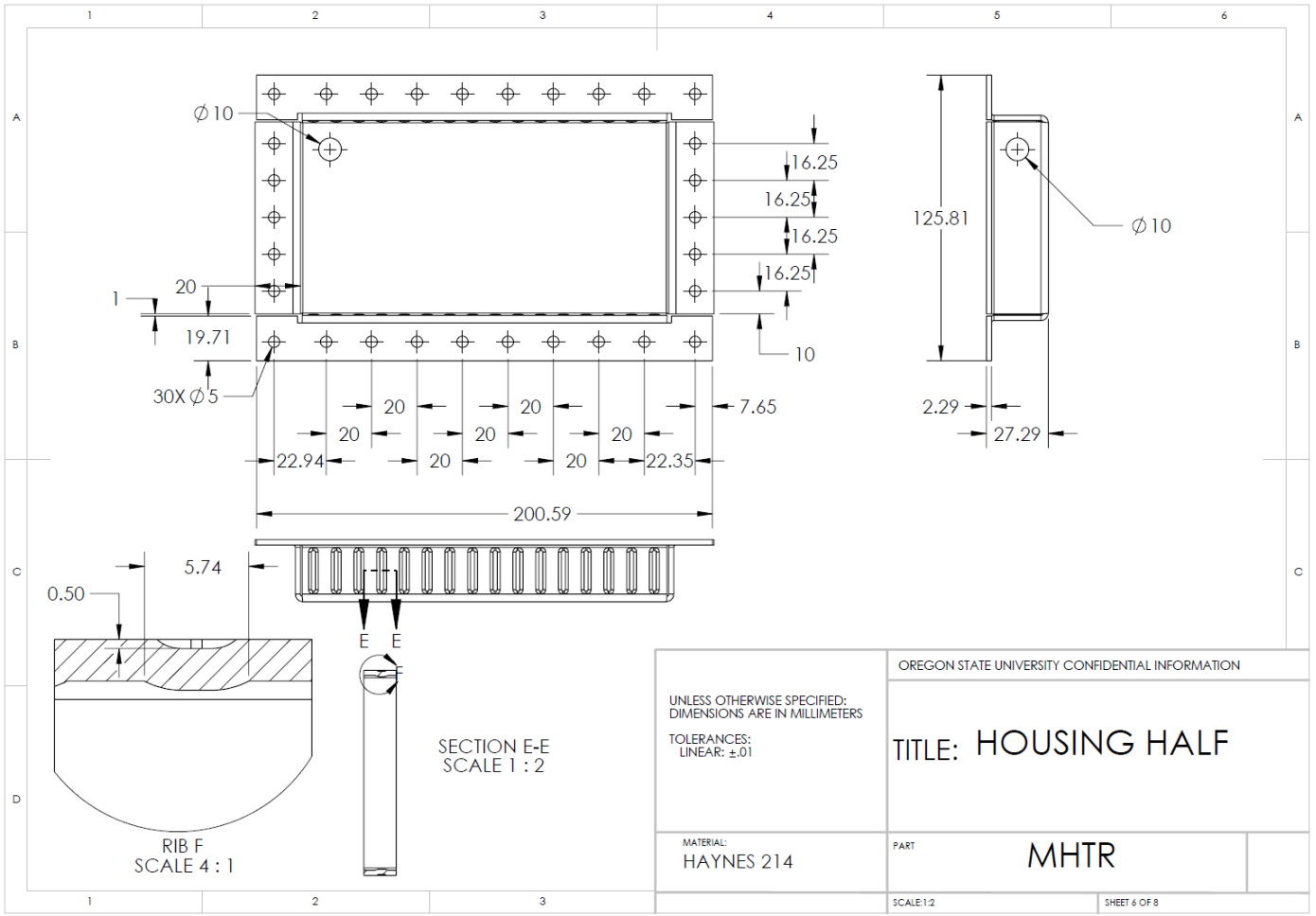
∅10
16.25
16.25
16.25
16.25
125.81
∅10
20
1
19.71
10
30X ∅5
20
20
7.65
20
20
20
22.94
20
20
22.35
200.59
5.74
0.50
E
E
RIB F
SCALE 4 : 1
SECTION E-E
SCALE 1 : 2
2.29
27.29
OREGON STATE UNIVERSITY CONFIDENTIAL INFORMATION
UNLESS OTHERWISE SPECIFIED:
DIMENSIONS ARE IN MILLIMETERS
TOLERANCES:
LINEAR: ±.01
TITLE: HOUSING HALF
MATERIAL:
HAYNES 214
PART
MHTR
SCALE:1:2
SHEET 6 OF 8

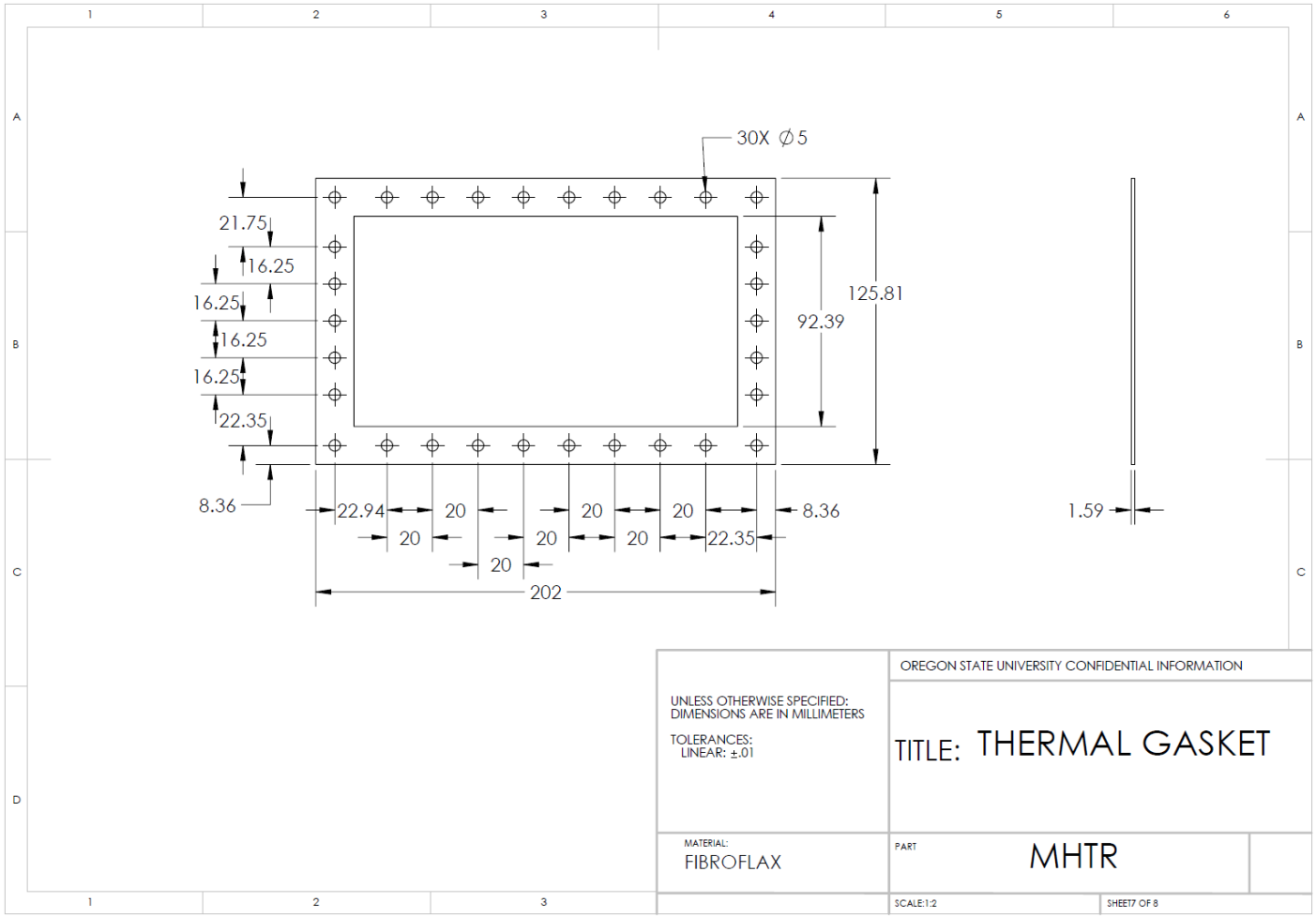
30X ∅5
21.75
16.25
16.25
16.25
16.25
22.35
8.36
125.81
92.39
22.94
20
20
20
20
20
20
20
20
22.35
8.36
202
1.59
OREGON STATE UNIVERSITY CONFIDENTIAL INFORMATION
UNLESS OTHERWISE SPECIFIED:
DIMENSIONS ARE IN MILLIMETERS
TOLERANCES:
LINEAR: ±.01
TITLE: THERMAL GASKET
MATERIAL:
FIBROFLAX
PART
MHTR
SCALE:1:2
SHEET7 OF 8

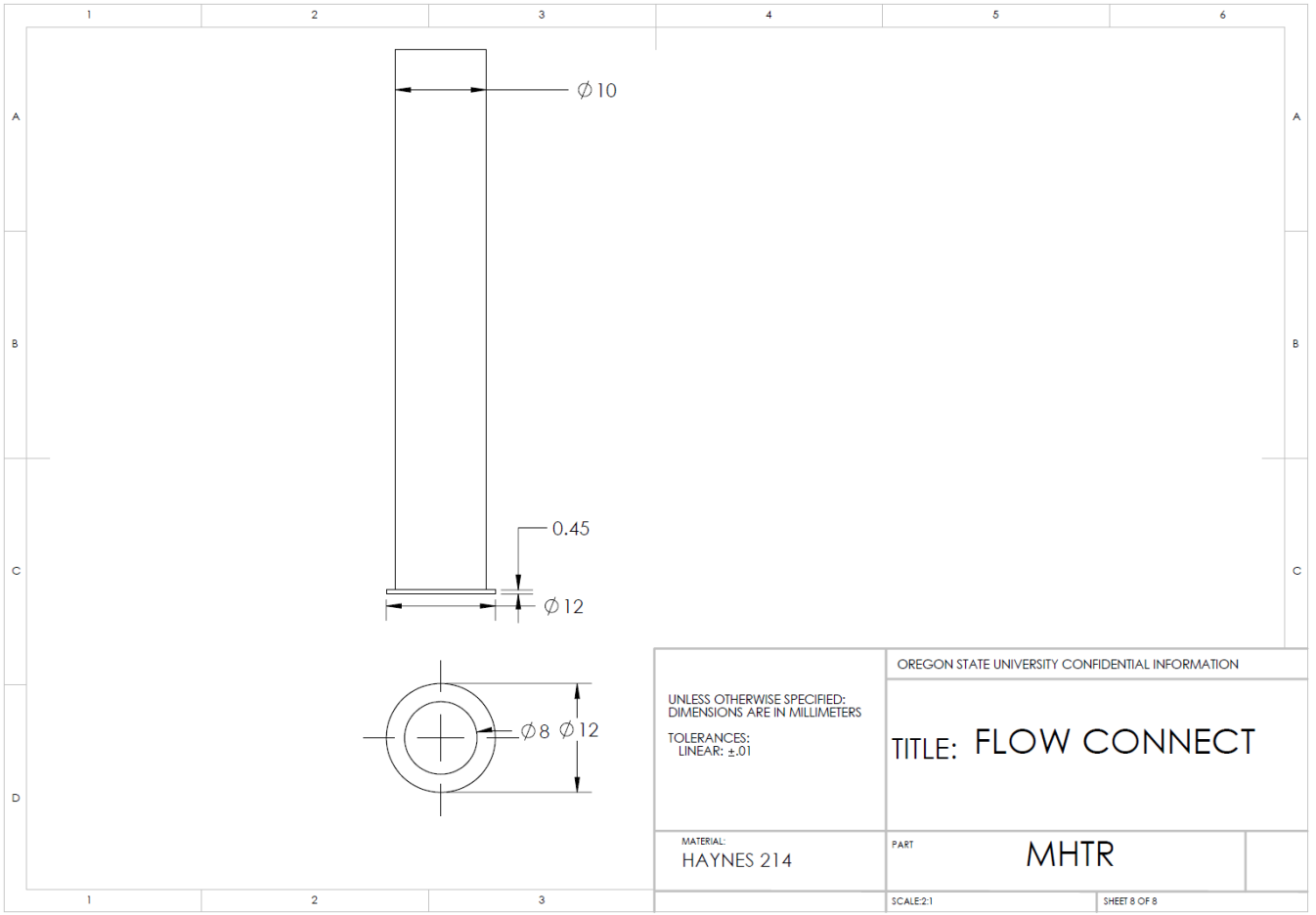
1
2
3
4
5
6
A
B
C
D
Ø10
0.45
Ø12
Ø8
Ø12
UNLESS OTHERWISE SPECIFIED:
DIMENSIONS ARE IN MILLIMETERS
TOLERANCES:
LINEAR: ±.01
OREGON STATE UNIVERSITY CONFIDENTIAL INFORMATION
TITLE: FLOW CONNECT
MATERIAL:
HAYNES 214
PART
MHTR
SCALE:2:1
SHEET 8 OF 8

7.4 Technology Demonstration Vehicle Engineering Packet

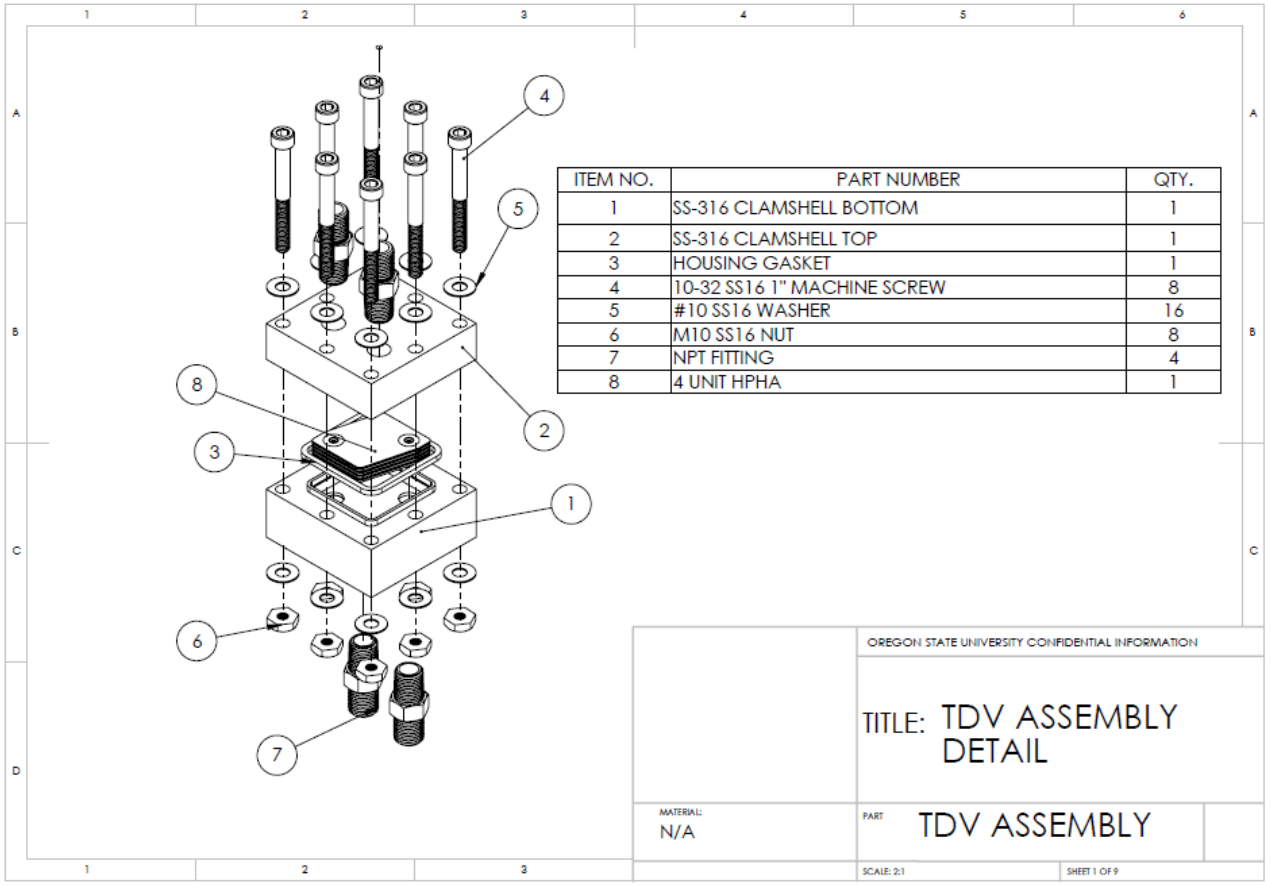

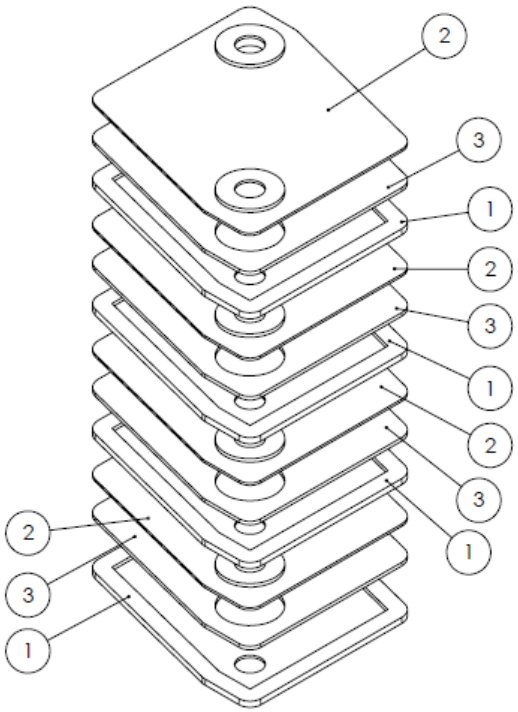

ITEM NO.	PART NUMBER	QTY.
1	HPHA FLOW SHIM A	4
2	HPHA FLOW SHIM B	4
3	MPTN REPRESENTATION	4

OREGON STATE UNIVERSITY CONFIDENTIAL INFORMATION

TITLE: 4 UNIT HPHA

MATERIAL: HAYNES 214

PART: TDV ASSEMBLY

SCALE: 2:1

SHEET 2 OF 9

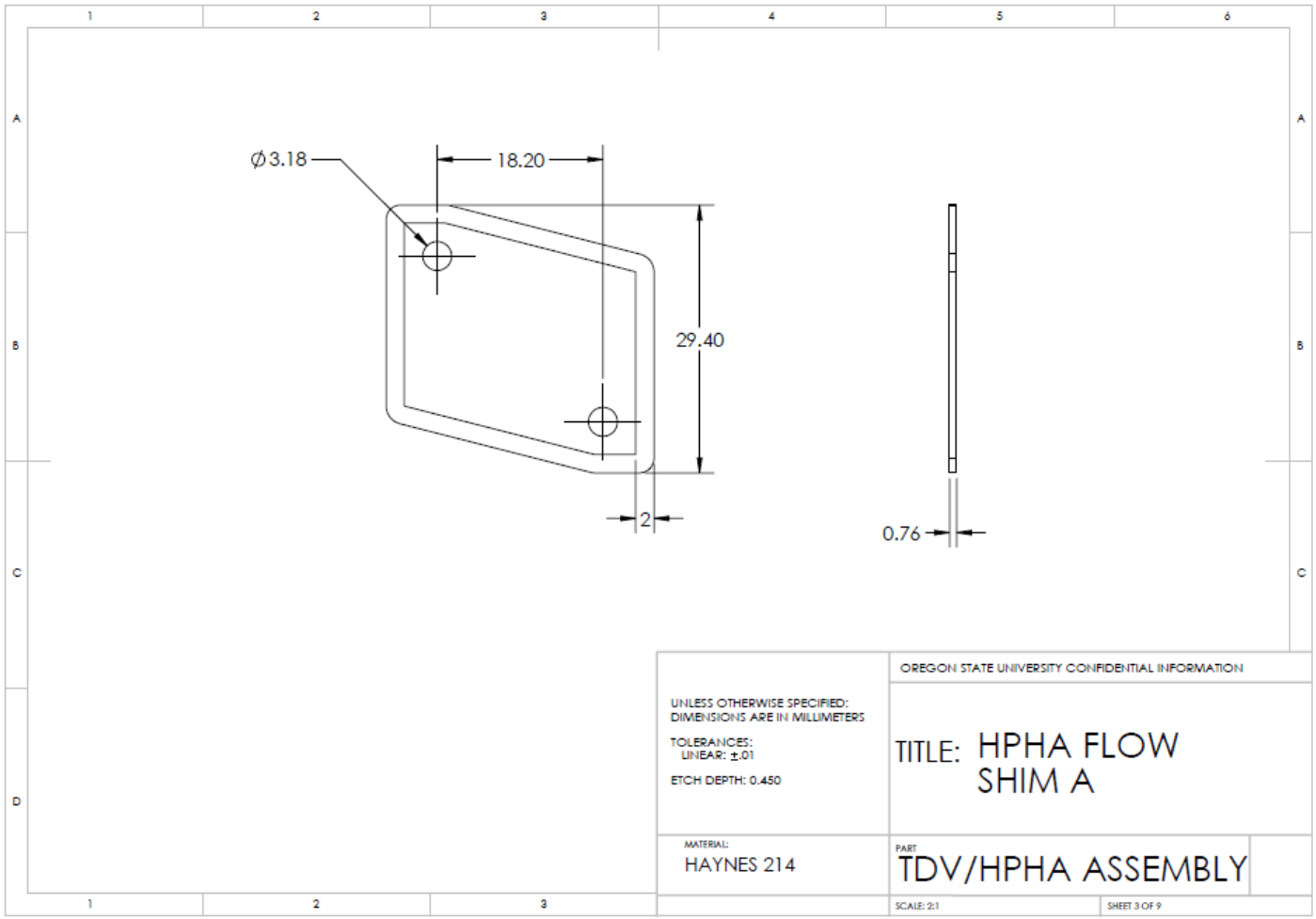
Ø3.18
18.20
29.40
2
0.76
OREGON STATE UNIVERSITY CONFIDENTIAL INFORMATION
UNLESS OTHERWISE SPECIFIED:
DIMENSIONS ARE IN MILLIMETERS
TOLERANCES:
LINEAR: ±.01
ETCH DEPTH: 0.450
TITLE: HPHA FLOW SHIM A
MATERIAL:
HAYNES 214
PART
TDV/HPHA ASSEMBLY
SCALE: 2:1
SHEET 3 OF 9

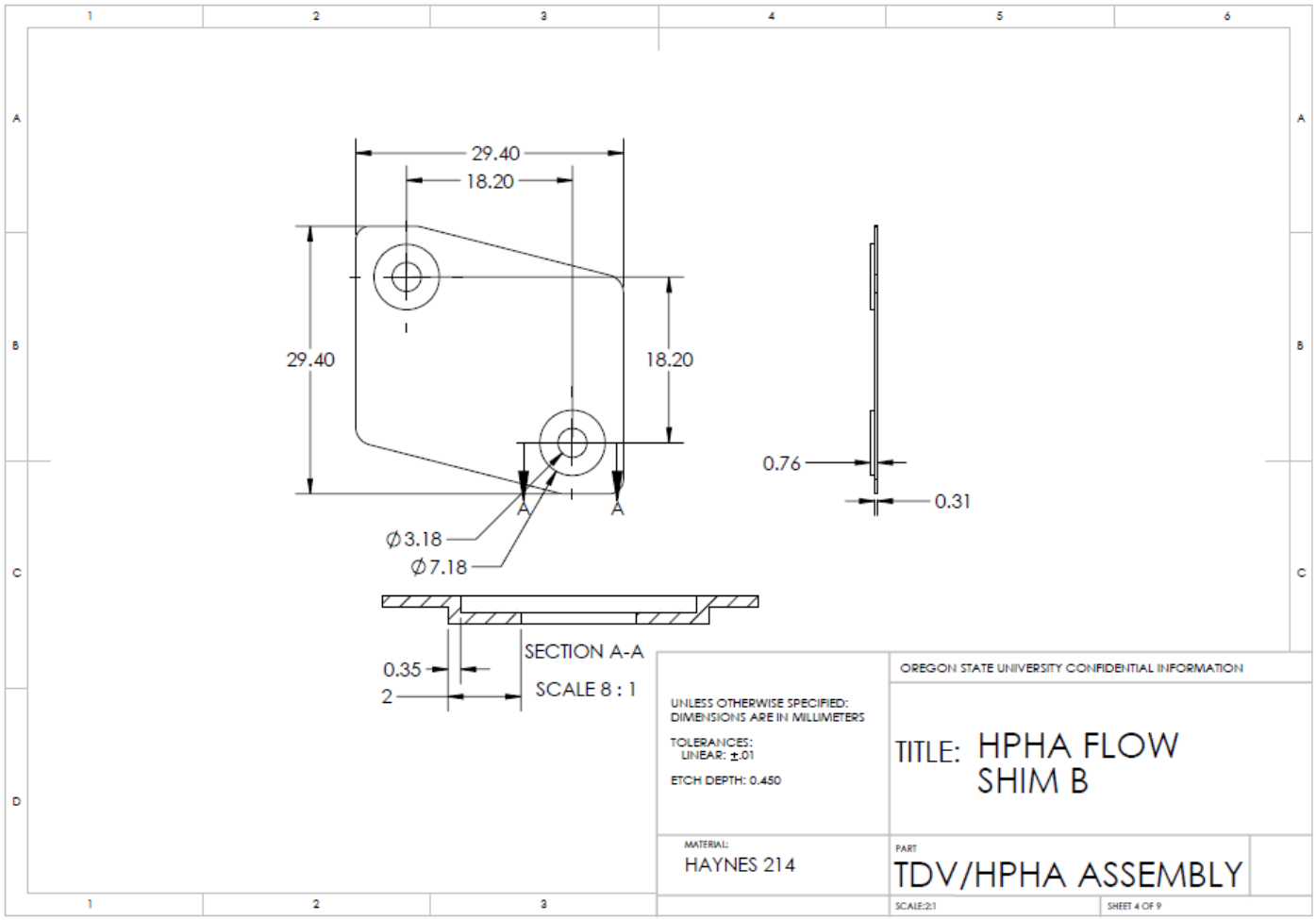
29.40
18.20
29.40
18.20
0.76
0.31
A
A
Ø3.18
Ø7.18
SECTION A-A
SCALE 8 : 1
0.35
2
OREGON STATE UNIVERSITY CONFIDENTIAL INFORMATION
UNLESS OTHERWISE SPECIFIED:
DIMENSIONS ARE IN MILLIMETERS
TOLERANCES:
LINEAR: ±.01
ETCH DEPTH: 0.450
TITLE: HPHA FLOW SHIM B
MATERIAL:
HAYNES 214
PART
TDV/HPHA ASSEMBLY
SCALE:2:1
SHEET 4 OF 9

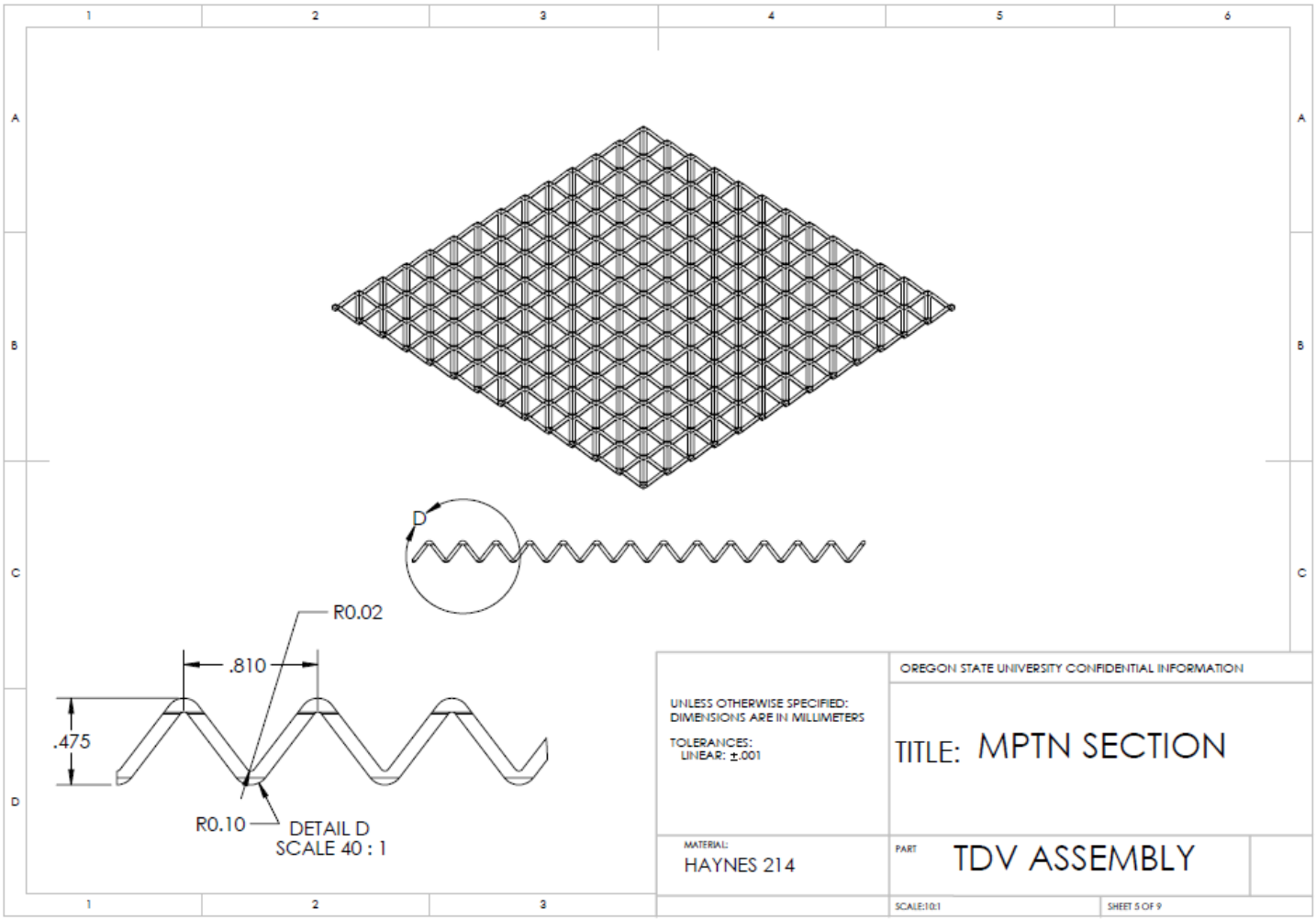
D
R0.02
.810
.475
R0.10
DETAIL D
SCALE 40 : 1
OREGON STATE UNIVERSITY CONFIDENTIAL INFORMATION
UNLESS OTHERWISE SPECIFIED:
DIMENSIONS ARE IN MILLIMETERS
TOLERANCES:
LINEAR: ±.001
TITLE: MPTN SECTION
MATERIAL:
HAYNES 214
PART
TDV ASSEMBLY
SCALE:10:1
SHEET 5 OF 9

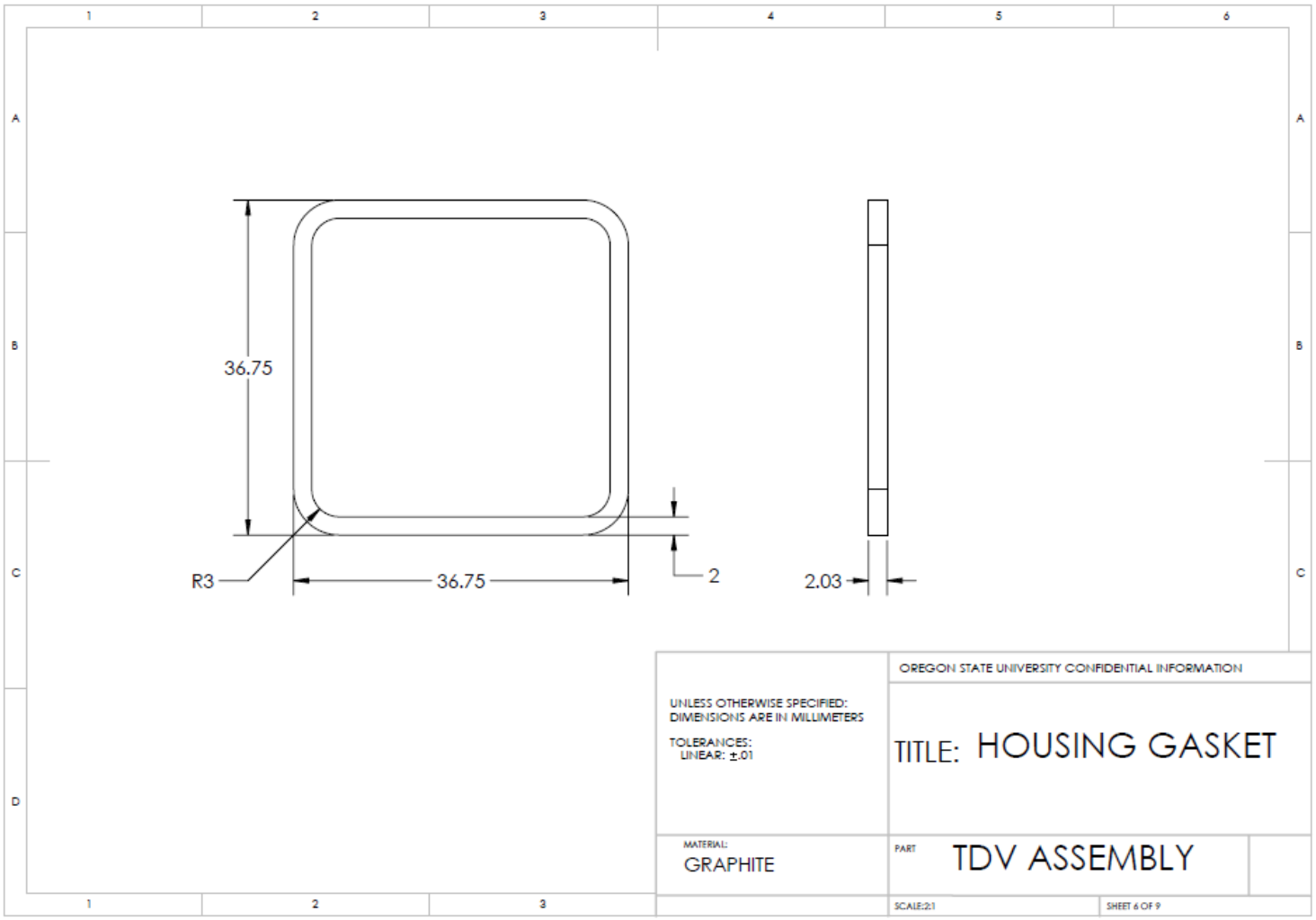
1
2
3
4
5
6
A
B
C
D
36.75
R3
36.75
2
2.03
OREGON STATE UNIVERSITY CONFIDENTIAL INFORMATION
UNLESS OTHERWISE SPECIFIED:
DIMENSIONS ARE IN MILLIMETERS
TOLERANCES:
LINEAR: ±.01
TITLE: HOUSING GASKET
MATERIAL:
GRAPHITE
PART
TDV ASSEMBLY
SCALE:2:1
SHEET 6 OF 9

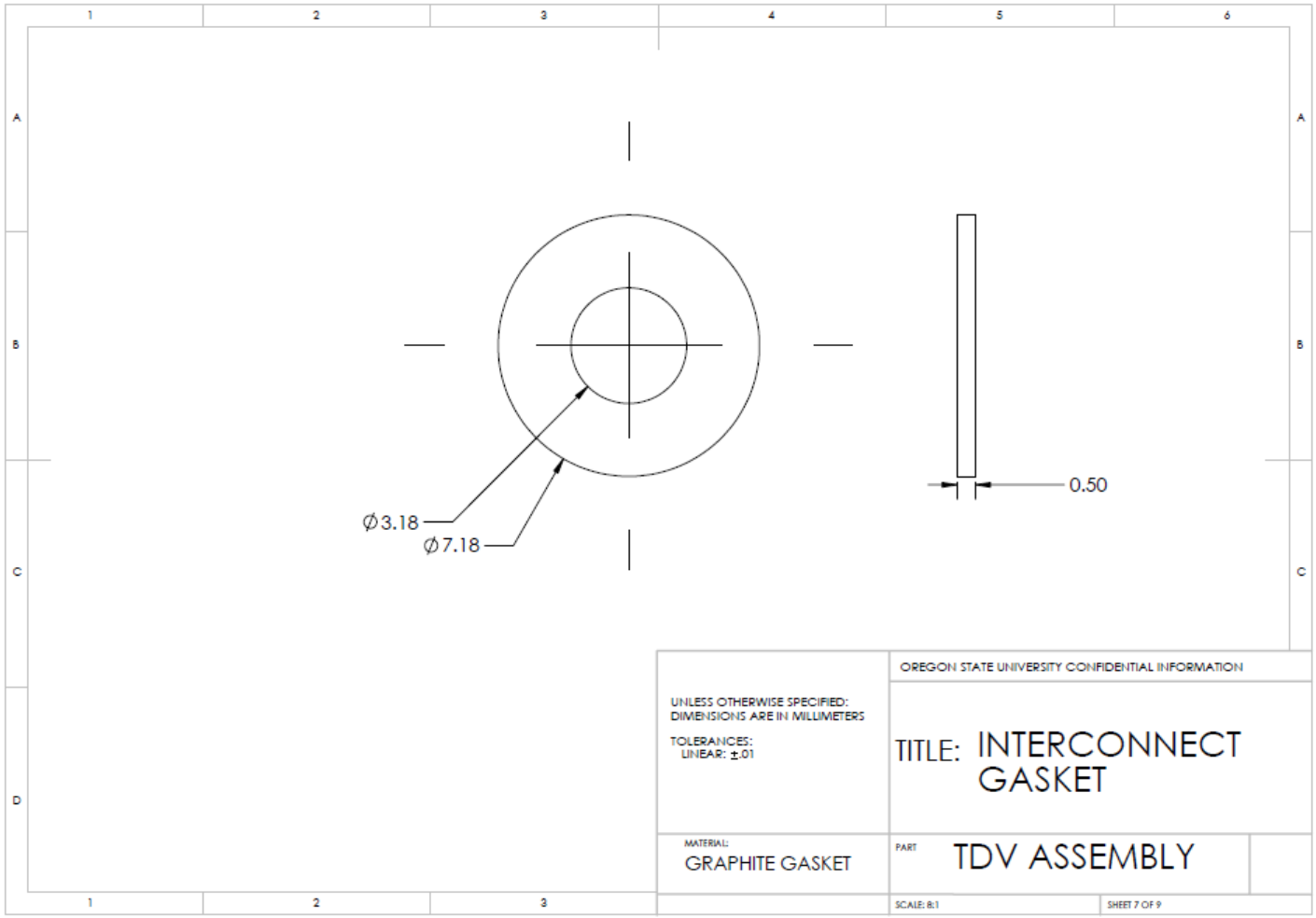
Ø3.18
Ø7.18
0.50
OREGON STATE UNIVERSITY CONFIDENTIAL INFORMATION
UNLESS OTHERWISE SPECIFIED:
DIMENSIONS ARE IN MILLIMETERS
TOLERANCES:
LINEAR: ±.01
TITLE: INTERCONNECT GASKET
MATERIAL:
GRAPHITE GASKET
PART
TDV ASSEMBLY
SCALE: 8:1
SHEET 7 OF 9

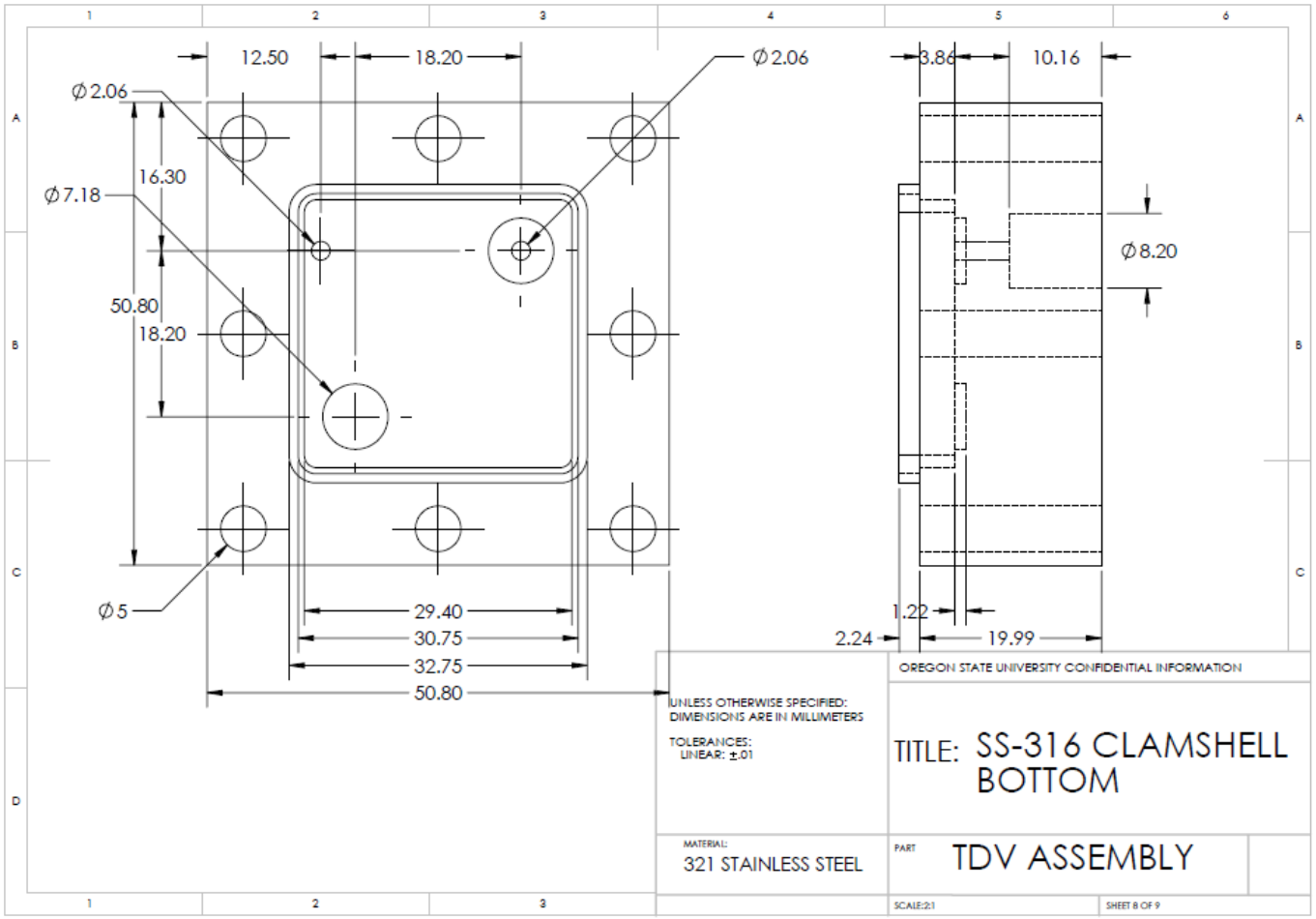
12.50
18.20
Ø2.06
Ø2.06
16.30
Ø7.18
50.80
18.20
Ø5
29.40
30.75
32.75
50.80
3.86
10.16
Ø8.20
1.22
2.24
19.99
UNLESS OTHERWISE SPECIFIED:
DIMENSIONS ARE IN MILLIMETERS
TOLERANCES:
LINEAR: ±.01
OREGON STATE UNIVERSITY CONFIDENTIAL INFORMATION
TITLE: SS-316 CLAMSHELL BOTTOM
MATERIAL:
321 STAINLESS STEEL
PART
TDV ASSEMBLY
SCALE:2:1
SHEET 8 OF 9

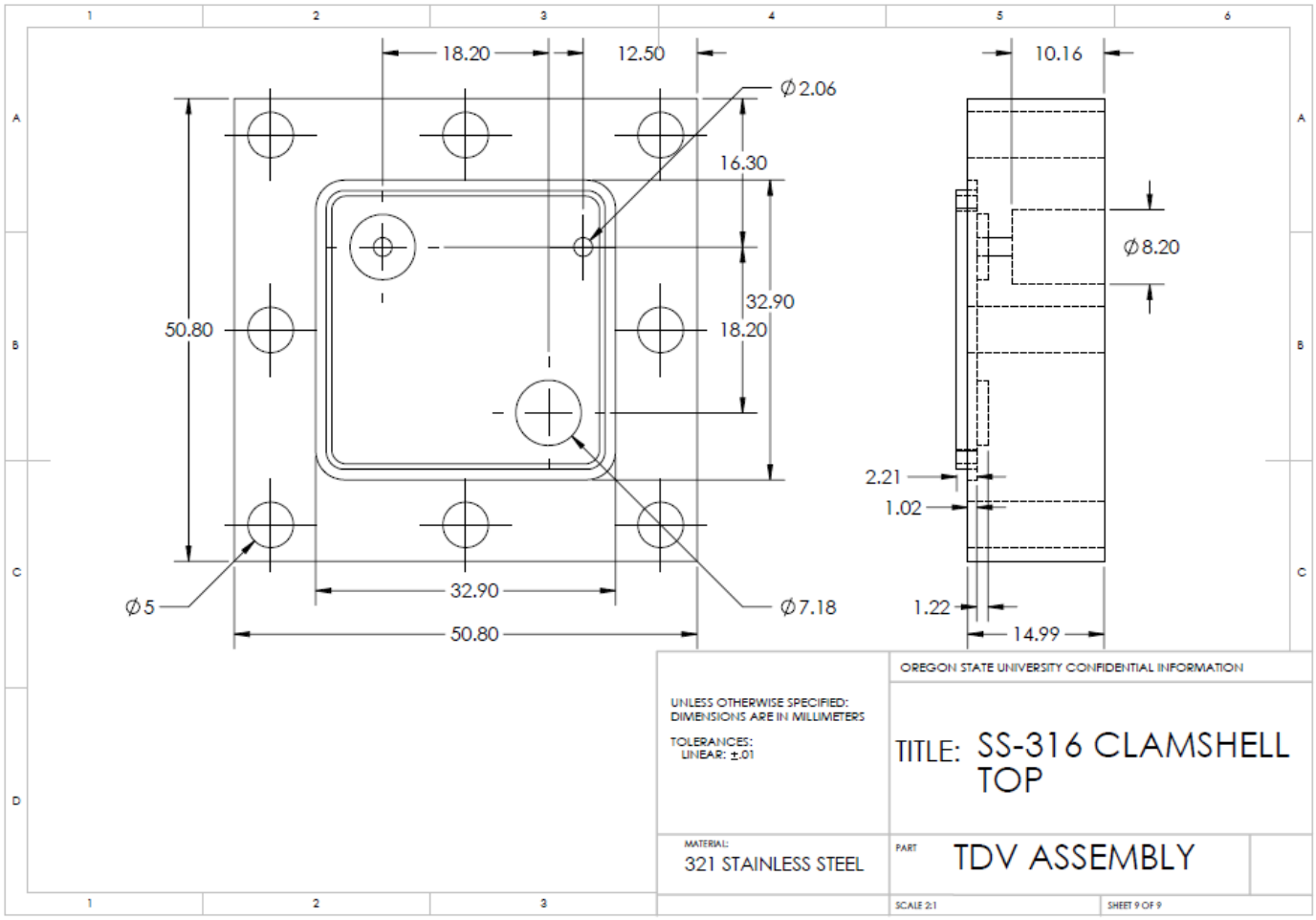
18.20
12.50
Ø2.06
16.30
32.90
18.20
50.80
Ø5
32.90
50.80
Ø7.18
10.16
Ø8.20
2.21
1.02
1.22
14.99
OREGON STATE UNIVERSITY CONFIDENTIAL INFORMATION
UNLESS OTHERWISE SPECIFIED:
DIMENSIONS ARE IN MILLIMETERS
TOLERANCES:
LINEAR: ±.01
TITLE: SS-316 CLAMSHELL TOP
MATERIAL:
321 STAINLESS STEEL
PART
TDV ASSEMBLY
SCALE 2:1
SHEET 9 OF 9